Development of Electro-active Graphene Nanoplatelets and Composites for Application as Electrodes within Supercapacitors

by

Aaron Davies

A thesis

presented to the University of Waterloo

in fulfillment of the

thesis requirement for the degree of

Master of Applied Science

in

Chemical Engineering

Waterloo, Ontario, Canada, 2012

Author's Declaration:

I hereby declare I am the sole author of this thesis. This is a true copy of my thesis, including any required final revisions, as accepted by my examiners.

I understand that my thesis may be made electronically available to the public.

Abstract:

The mounting concern for renewable energies from ecologically conscious alternatives is growing in parallel with the demand for portable energy storage devices, fuelling research in the fields of electrochemical energy storage technologies. The supercapacitor, also known as electrochemical capacitor, is an energy storage device possessing a near infinite life-cycle and high power density recognized to store energy in an electrostatic double-layer, or through a pseudocapacitance mechanism as a result of an applied potential. The power density of supercapacitors far exceeds that of batteries with an ability to charge and discharge stored energy within seconds. Supercapacitors compliment this characteristic very well with a cycle life in excess of 10^6 cycles of deep discharge within a wide operational temperature range, and generally require no further maintenance upon integration. Conscientious of environmental standards, these devices are also recyclable.

Electrochemical capacitors are currently a promising candidate to assist in addressing energy storage concerns, particularly in hybridized energy storage systems where batteries and supercapacitors compliment each other's strengths; however specific challenges must be addressed to realize their potential. In order to further build upon the range of supercapacitors for future market applications, advancements made in nanomaterial research and design are expected to continue the materials development trend with a goal to improve the energy density through the development of a cost-efficient and correspondingly plentiful material. However, it is important to note that the characteristic power performance and exceptional life-cycle should be preserved alongside these efforts to maintain their niche as a power device, and not simply develop an alternative to the average battery. It is with this clear objective that this thesis presents research on an emerging carbon material derived from an abundant precursor, where the investigations focus on its potential to achieve high energy and power density, stability and integration with other electroactive materials.

Activated carbons have been the dominant carbon material used in electric double-layer capacitors since their inception in the early 1970s. Despite a wide range of carbon precursors and activation methods

available for the generation of high surface area carbons, difficulties remain in controlling the pore size distribution, pore shape and an interconnected pore structure to achieve a high energy density. These factors have restricted the market growth for supercapacitors in terms of the price per unit of energy storage. Activation procedures and subsequent processes for these materials can also be energy intensive (i.e. high temperatures) or environmentally unfriendly, thus the challenge remains in fabricating an inexpensive high surface-area electroactive material with favourable physical properties from a source available in abundance.

Double-layer capacitive materials researched to replace active carbons generally require properties that include: high, accessible surface-area; good electrical conductivity; a pore size distribution that includes mesopore and micropore; structural stability; and possibly functional groups that lend to energy storage through pseudocapacitive mechanisms. Templated, fibrous and aerogel carbons offer an alternative to activated carbons; however the drawbacks to these materials can include difficult preparation procedures or deficient physical properties with respect to those listed above. In recent years nanostructured carbon materials possessing favourable properties have also contributed to the field.

Graphene nanoplatelet (GNP) and carbon nanotube (CNT) are nanostructured materials that are being progressively explored for suitable development as supercapacitor electrodes. As carbon lattice structured materials either in the form of a 2-dimensional sheet or rolled into a cylinder both of these materials possess unique properties desirable in for electrode development. In the proceeding report, GNPs are investigated as a primary material for the synthesis of electrodes in both a pure and composite form. Three projects are presented herein that emphasize the suitability of GNP as a singular carbon electrode material as well as a structural substrate for additional electroactive materials. Investigation in these projects focuses on the electrochemical activity of the materials for supercapacitor devices, and elucidation of the physical factors which contribute towards the observed capacitance.

An initial study of the GNPs investigates their distinct capacitive ability as an electric double-layer material for thin-film applications. The high electrically conductivity and sheet-like structure of GNPs supported the fabrication of flexible and transparent films with a thickness ranging from 25 to 100

nm. The thinnest film fabricated (25 nm) yielded a high specific capacitance from preliminary evaluation with a notable high energy and power density. Furthermore, fast charging capabilities were observed from the GNP thin film electrodes.

The second study examines the use of CNT entanglements dispersed between GNP to increase the active surface area and reduce contact resistances with thin-film electrodes. Through the use MWNT/GNP and SWNT/GNP composites it was determined that tube aspect ratio influences the resulting capacitive performance, with the formation of micropores in SWNT/GNP yielding favourable results as a composite EDLC.

The third study utilizes electrically conducting polypyrrole (PPy) deposited onto a GNP film through pulse electrodeposition for use as a supercapacitor electrode. Total pulse deposition times were evaluated in terms of their corresponding improvements to the specific capacitance, where an optimal deposition time was discovered. A significant increase to the total specific capacitance was observed through the integration PPy, with the majority charge storage being developed via psuedocapacitive redox mechanisms.

A summary of the studies presented here centers on the development of GNP electrodes for application in high power supercapacitor devices. The potential use for GNP in both pure and composite electrode films is explored for electrochemical activity and capacitive capabilities, with corresponding physical characterization techniques performed to examine influential factors which contribute to the final results. The work emphasizes the suitability of GNP material for future investigations into their application as carbon or carbon composite electrodes in supercapacitor devices.

Acknowledgements:

I would first and foremost give my thanks to God for His blessings and for providing me the ability, character and discipline to accomplish the following works. A special thanks to my supervisor Dr. Aiping Yu for her strong dedication towards my education and development as a professional engineer.

I give everlasting gratitude to my wife, Sarah Graham, for her love, support and patience throughout my education; I would not be here to thank her without all that she has done for me and our family. Furthermore, I dedicate my gratitude to my three daughters: Mikayla, Gabrielle and Charlotte. They are genuinely a gift from God, expressing unconditional love and understanding throughout my studies; girls, you are true princesses. A special thank you goes to Dr. Zhongwei for his support and advice in my research. I would also like to thank my colleagues including: Isaac Roes, Phillip Audette, Davis Lye, Victor Chabot, Ryan Hsu, Drew Higgins, Clark (Zhu) Chen, Heywoong Park, Ja-Yeon Choi, Wenmu Li, Jason Wu and Fathy Hassan for all their time and assistance.

I would like to acknowledge the time and support given by my reviewers, including Dr. Aiping Yu, Dr. Zhongwei Chen and Dr. Boxin Zhao.

Contents

List of Figures x

List of Tables xiv

List of Abbreviations, Symbols and Nomenclature xv

1.0 Introduction to supercapacitors 1

1.1 Main types and structures of supercapacitors 4

1.1.1 Electric Double-Layer Capacitors (EDLCs) 4

1.1.2 Pseudocapacitors 6

1.1.3 Asymmetric hybrid Capacitors 7

1.2 Physical/electrochemical processes in supercapacitors 8

2.0 Materials for supercapacitor electrode 13

2.1 General requirements of the materials 13

2.1.1 Effects of pore size and pore-size distribution 13

2.1.2 Surface Area 14

2.2 Carbon as an EDLC material 15

2.2.1 Carbon Nanotubes 15

2.2.2 Graphene 16

2.3 Pseudocapacitive Electrode Materials 20

2.3.1 Transition Metals 21

2.3.2 Electrically Conducting Polymers 21

2.4 Electrolytes for use in Electrochemical Supercapacitors 23

2.4.1 Aqueous Electrolytes 24

2.4.2 Organic and Ionic Liquid Electrolytes 24

2.5 Project Objective 25

3.0 Techniques for Physical and Electrochemical Characterization 26

3.1 Scanning electron microscopy 26

3.2 Transmission electron microscopy 26

3.3 Thermogravimetric analysis 27

3.4 Ultraviolet-visible Spectroscopy 27

3.5 Half cell electrochemical testing 28

3.5.1 Cyclic Voltammetry 28

3.5.2 Charge or Discharge Chronopotentiometry 30

3.5.3 Impedance Spectroscopy 32

3.6 Energy and Power Density 34

3.6.1 Energy Density 35

3.6.2 Power Density 35

4.0 Ultra-thin and transparent graphene nanoplatelet film electrodes 37

4.1 Introduction and objective 37

4.3 Results and Discussion 38

4.4 Conclusions 48

5.0 In-situ Preparation of Graphene/Carbon Nanotube Hybrid Transparent and Flexible Thin-Films as Electrode for Supercapacitor Application 50

5.1 Introduction 50

5.2 Experimental 51

5.3 Results and Discussion 52

5.4 Conclusion 63

6.0 Graphene-based supercapacitors electrodes with Pulse-Electropolymerization of Polypyrrole 65

6.1 Introduction 65

6.2 Experimental 66

6.4 Conclusions 81

7.0 Summary and perspective towards future research 83

References 85

List of Figures

Figure 1: Ragone plot with guide lines of specific power with respect to specific energy of current energy storage and conversion devices,.....2

Figure 2: Depiction of a charged electric double-layer capacitor.....6

Figure 3: An increase in the potential window of a pseudocapacitive adsorption mechanism (Θ) with respect to voltage given single, pair and a triad of redox couples are involved.....7

Figure 4: Progressive evolution of models describing the electric double layer at a positive electrode: (a) the initial Helmholtz model, (b) the Guoy-Chapman model, and (c) the Stern model, where the division of the inner Helmholtz plane (IHP) and outer Helmholtz plane (OHP) show specifically and non-specifically absorbed ions. The distance, *d*, in the Helmholtz model describes the double-layer distance, ψ_0 and ψ are the surface and electrode/electrolyte interface potentials, respectively. 10

Figure 5: AHC: Schematic of hybrid carbon/nano-Li4Ti5O12 utilizing LiPF6.....12

Figure 6: Imaging by TEM of individual graphene sheets obtained from chemical modification are observed around the edges of the particle.....18

Figure 7: Diagram representing the p-doping (a) and n-doping (b) of polymers as they undergo charging and discharging. 22

Figure 8: Cyclic voltammograms comparing (a) an ideal capacitor and (b) a localized and reversible pseudo-capacitive reaction for an electrode thinly coated by a redox material at increasing scan rates. ...30

Figure 9: Nyquist impedance diagram comparing the ideal vertical impedance of a capacitor (thin line) and that of an EC supercapacitor (thick line). The equivalent series resistance (ESR) is derived from the intercept of the real impedance axis, followed by the equivalent distributed (EDR) of a porous electrode. 34

Figure 10: (a) Photographs of transparent thin-films of varying thickness on glass slides. (b) TEM image of graphene collected from dispersion before filtration. (c) SEM image of 100 nm graphene film on glass slide.....39

Figure 11: Transmittance spectra of thin-films of varying thickness. Top-left inset is the plot of absorbance at 550 nm versus thin-film thickness. Bottom-right inset photo shows the flexibility of GNPs film on PET substrate..... 41

Figure 12: A plot of GNP thin film absorbance at 550 nm with respect to film thickness 41

Figure 13: CV curves for (a) 25 nm, (b) 50 nm, (c) 75 nm, and (d) 100 nm thin films at scan rate of 10, 20, 50, 100, and 200 mV/s 43

Figure 14: Cyclic voltammograms of GNP (80 nm) thin film at (a) high scan rates (100 – 200 $V \cdot s^{-1}$); with corresponding (b) discharge currents and (c) specific gravimetric capacitance. 45

Figure 15: A Ragone plot of energy density versus power density for each GNP thin film..... 46

Figure 16: Charge-discharge curves for (a) 25 nm, (b) 50 nm, (c) 75 nm, and (d) 100 nm thin films at 1.0 A/g. 47

Figure 17: AC EIS curves for (a) 25 nm, (b) 50 nm, (c) 75 nm, and (d) 100 nm thin films. 48

Figure 18: Schematic illustration of the graphene and carbon nanotubes hybrid new structures in the transparent and free-standing film. 51

Figure 19: Transmittance spectra of 100 nm thick thin-films of SWNTs, G-S hybrid, GNPs, G-M hybrid and MWNTs. Bottom-right inset is a photograp of the 100 nm thick G-S hybrid film on glass slides, a logo underneath of it showing the transparency of the film..... 54

Figure 20: SEM images of (a)G-S and (b)G-M at low magnification; and (c) G-S and (d) G-M at high magnification. 55

Figure 21: CV curves of (a) SWNTs, (b) G-S, (c) GNPs, (d) MWNTs and (e) G-M in 2 M KCl at scan rates of 10, 20, 50, 100 and 200 $mV \cdot s^{-1}$. 57

Figure 22: CD curves of (a) SWNT, GNP and composite G-S, and (b) MWNT, GNP and composite G-M at a current density of 0.5 $A \cdot g^{-1}$ in 2 M KCl. 58

Figure 23 Nyquist plots of (a) MWNT, (b) MWG, (c) GNP, (d) SWNT and (e) SWG at 0.1 V. Top right inset shows high frequency region of ESR. 60

Figure 24: Ragone plot of GNP and a) MWNT and b) SWNT composite film performance. 61

Figure 25: Capacitance retention for 800 cycles at 2 · A g^{-1} current density for GNP with respect to a) MWNT and G-M, and b) SWNT and G-S. 63

Figure 26: (a) Diagram of the apparatus used to deposit PPY on GNPs and electrochemical testing, where the clamp and rubber O-ring are not shown; (b) Electrodeposition potential waveform used in deposition experiments, with deposition pulse length T_d and rest pulse length T_r. 66

Figure 27: Photographs showing the flexibility of the (a) pure GNPs and (b) G/PPy 120s films, the in-set is the SEM image at the observation area with the white bar is 100 nm 68

Figure 28: Schematic diagram illustrating how rest periods allow for Py molecules to diffuse into the pore space of the G between deposition pulses. This leads to a more uniform coating and less blocked pores than obtained with a continuous deposition method 70

Figure 29: SEM images of (a) pure G and G/PPy after a (b) 60 s, (c) 120 s, (d) 360 s electrodeposition. The white particles are the PPy and the white bar is 1 μm 71

Figure 30: (a) Average PPy particle diameter and (b) average PPy particle density by electrodeposition time as determined by SEM; (c) Particle size distribution of G/PPy 60, 120 and 360. Particles were grouped into intervals with widths of 10nm 73

Figure 31: TGA thermograms of (a) PC membrane and (b) G and G/PPy 60, 120 and 360 76

Figure 32: Cyclic Voltammograms curves for the (a) G, (b) G-PPy60, (c) G-PPy120 and (d) G-PPy360 electrodes in a KCl solution between -0.4 and 0.6 V vs. SCE at scan rates of 0.01, 0.02, 0.05, 0.1 and 0.2 V · s-1. (e) Specific Capacitance of all the G/PPy electrodes by electrodeposition time as determined by CV with different scan rates. (f) Galvanostatic Charge-Discharge curves for the G, G-PPy60, G-PPy120 and G-PPy360 electrodes for comparison at a current density of 1 A · g-1 between -0.4 and 0.6 V vs. SCE in 1 M KCl 77

Figure 33: Nyquist plots of the G/PPy electrodes for (a) G, (b) G-PPy60, (c) G-PPy120 and (d) G-PPy360 at frequencies between 1 MHz and 10 mHz with a sinusoidal signal amplitude of 0.01 V vs. SCE in 1 M KCl 80

Figure 34: Ragone plot of the energy density vs. power density of the pure G and G/PPy 60, 120 and 360 electrodes, where capacitance data from CV analysis was applied. 81

Figure 35: A schematic of a hypothetical two electrode device fabricated with G/PPy 120 composite material for future work. 82

List of Tables

Table 1: Measured specific gravimetric capacitance C_p of ultra-thin GNP film electrodes from CV and CD analysis in 2 M KCl...... 44

Table 2: The absorbance at 550 nm from UV-spectroscopy for SWNTs, G-S hybrid, GNPs, G-M hybrid and MWNTs...... 54

Table 3: The absorbance at 550 nm from UV-spectroscopy for SWNTs, G-S hybrid, GNPs, G-M hybrid and MWNTs...... 61

Table 4 The capacitance calculated from cyclic coltammetry (CV), chronopotentiometry (CD), and the electrical series resistance (ESR) from EIS, maximum energy density and maximum power density for SWNTs, G-S hybrid, GNPs, G-M hybrid and MWNTs...... 62

List of Abbreviations, Symbols and Nomenclature

AC	alternating current
AV	alternating voltage
CD	charge/discharge chronopotentiometry
CNT	carbon nanotube
C_p	gravimetric specific capacitance ($F \cdot g^{-1}$)
CPE	constant phase element
CV	cyclic voltammetry
EDLC	electric double-layer capacitance
EIS	electrochemical impedance spectroscopy
ESR	equivalent series resistance
GNP	graphene nanoplatelet
GO	graphene oxide
KCl	potassium chloride
MWNT	multi-walled carbon nanotube
PC	polycarbonate
PPy	polypyrrole
Py	pyrrole monomer
SCE	standard calomel electrode

SEM	scanning electron microscopy
SWNT	single walled carbon nanotube
TEM	transmission electron microscopy
XRD	x-ray defraction

1.0 Introduction to supercapacitors

The supercapacitor, often called electrochemical capacitor (EC) or ultracapacitor as a result of their exceptionally high capacitance has been used since the mid seventies as an energy storage device, where labels such as these were initially coined by manufacturers using characteristic materials for fabrication. Investigations into supercapacitor design and development began with a patent assigned to General Electric in 1957, which described the manufacturing of a device using porous carbon electrodes flooded with sulfuric acid [1]. The patented device employed an electrostatic charge mechanism described by electric double-layer capacitance (EDLC) modeling, to develop a capacitive charge at the electrode/electrolyte interface. A key aspect of this design was to utilize the high surface area in carbon materials, which upon further improvements enabled a previously unattainable high specific capacitance to be achieved. Numerous commercial companies (Maxwell Technologies, Panasonic, NessCap etc.) have since designed ECs using a variety of porous carbon materials as electrodes. Alternative to the charge mechanism of EDLC, pseudocapacitance was investigated by Conway and group in collaboration with Continental Group Inc. beginning in 1975 with their studies of ruthenium oxide films. Pseudocapacitance differs from EDLC capacitance in that a fast Faradaic reaction mechanism is responsible for a capacitive charge developing at the interface, or within the material itself, at potentials specific to the redox couple of the electrode material and electrolyte [2][3].

In addition to supercapacitors, batteries are a well known electrochemical energy storage device. In order to better understand the inherent differences between these two electrochemical storage systems as well as electrochemical energy conversion systems, a Ragone plot can be drawn to illustrate their respective performances. Ragone plots are often used to graph the characteristic power density in relation to the energy density of such systems as observed in Figure 1 [4]. The unique role that each energy storage or conversion system plays is evident by their region of dominance.

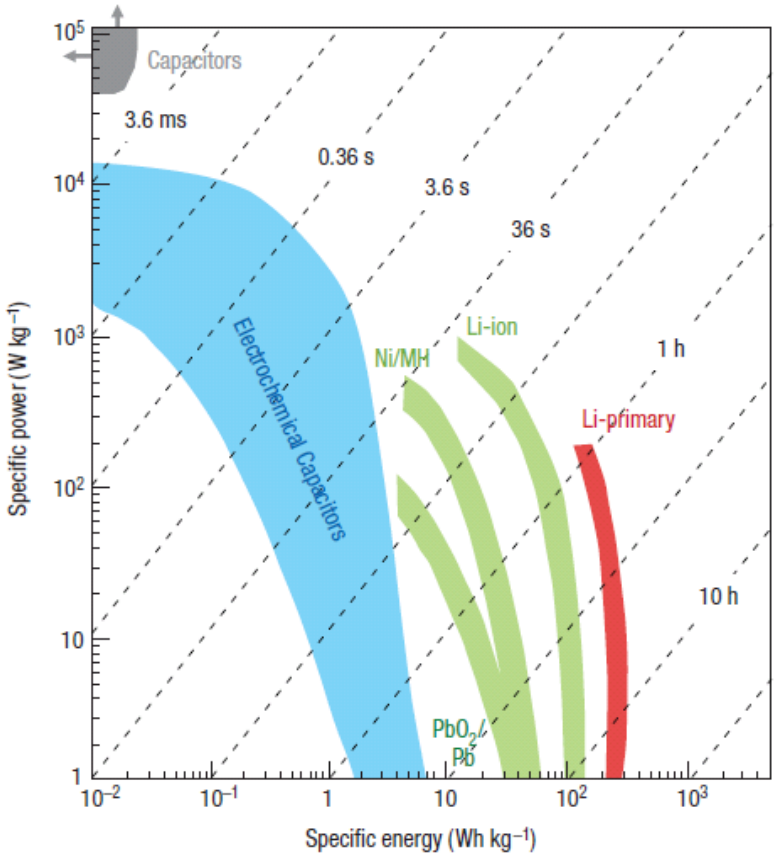

Figure 1: Ragone plot with guide lines of specific power with respect to specific energy of current energy storage and conversion devices, Reprinted from [4] Copyright 2008 with permission from Macmillan Publishers Ltd: Nature Materials

While batteries are the popular choice for high portable energy storage, with Li-ion batteries achieving energy densities of 180 Wh kg^{-1} [5], the electrode materials suffer strenuous volume and irreversible phase changes during charge discharge cycling that limits their cycle-life. This disadvantage further impedes their application for high power performance applications which often require rapid charging and discharging in short intervals. These shortcomings draw attention to the characteristic strengths of ECs.

Evident by the Ragone plot (Figure. 1), commercial ECs do not currently possess the large energy densities of batteries, with commercial devices ranging between 5 – 10 Wh· kg^{-1}. However, the power density of ECs far exceeds that of batteries with the ability to charge and discharge stored energy within seconds. ECs compliment this characteristic very well with a cycle life in excess of 10^6 cycles of deep

discharge within a wide operational temperature range and require no further maintenance upon integration. Conscientious of environmental standards, these devices are also recyclable. The US Department of Energy (DoE) recognized promising aspects of ECs in the early nineties following their assessment for use in hybrid electric vehicles (HEV), and has since rated the importance of EC research and development to be on par with batteries as energy storage devices for use in future technologies [6].

Earlier marketed ECs were used for applications in clock chips and computer memory for protection against memory loss resulting from a loss of primary power. Their expansion over the following 30 years into wireless communications, power quality and improving the energy efficiency of systems containing a separate primary power source has demonstrated their distinction as a energy device that can compliment and at times overcome the limitations of batteries. This has been demonstrated to be particularly useful by their successful incorporation in battery and diesel systems in allowing the recovery of brake energy to improve energy efficiency [7]. In order to further build upon the range of ECs for future market applications, advancements made in nanomaterial research and design are expected to continue the materials development trend with improved energy density. However, it is important to note that the characteristic power performance and exceptional life-cycle should be preserved in future generations of ECs to maintain their niche as a power device and not simply develop an alternative to the average battery.

The focus of the present thesis is directed towards the development of high energy density electroactive materials for high power supercapacitor electrodes. Prior to the discussion of these works, a background on supercapacitor types, operating principles and present challenges faced by their development are reviewed. In addition, techniques utilized for the physical and electrochemical characterization of the materials is discussed. The following works presented incorporate graphene nanoplatelets as a central material for supercapacitor electrodes. The chapters are summarized to include a full account of each work through an introduction, a summary of the results and discussion, and conclusions which may be derived from the following studies:

I. Ultra-thin and transparent films of GNP. This chapter centers on the work of reference [8].

II. Thin, transparent films of GNP intercalated with CNTs.

III. Integration of GNP with electrodeposited polypyrrole as a composite electrode film. This chapter centers on work from reference [9].

1.1 Main types and structures of supercapacitors

Supercapacitors are divided into two types that rely on respectively different methods of charge. With the discovery and subsequent commercialization of these devices in the seventies, porous carbon was utilized as an electrode material to develop electric double-layer capacitance during charging. A separate charge mechanism, called pseudocapacitance, differentiates from EDLC on a fundamental level. This type of supercapacitor is often best employed in an asymmetric hybrid configuration similar to that of a battery; however it frequently suffers a similar lack in stability and the life cycle can be significantly lower than that of carbon electrodes, depending upon the pseudocapacitive material.

1.1.1 Electric Double-Layer Capacitors (EDLCs)

The accumulation and release of electrostatic charge in EDLCs occurs via a withdrawal or deposition of electrons in either the cathode or anode, which in turn is induced by an applied potential across the device. The positive or negatively charged surface is balanced by an accumulation of counter-ions from the solution forming a double-layer of positive-negative charges (or vice-versa) that ideally remains electrostatic, having no electron transfers between layers throughout the process. The potential applied for capacitive charging is essentially limited by the thermodynamic stability of the electrolyte employed, reemphasizing the importance of electrolytes for energy storage. Principal aspects to consider regarding the physical attributes that contribute to EDLC include:

I. A large active area in contact with the electrolyte for capacitive charging
II. Good electrical conductivity to reduce the loss in power from internal resistance
III. Manipulation of the pore size pore distribution to complement the anticipated ion size of the electrolyte
IV. Interconnecting pores for ion mobility, accessibility and reduction in diffusion path length
V. Surface wettability to enhance pore flooding, improving the specific surface area utilized [10]

Commercial ECs all presently employ carbon for electric double-layer charging and discharging similar to that of dielectric capacitors. The capacitance of these devices develops from an electrostatic charging of the electrode/electrolyte interface described in Figure 2. Activated carbon currently remains the most widely used carbon material owing to the low costs, availability and variety of precursor material [10] to achieve near 200 F g^{-1} in aqueous electrolyte and half of this in organic electrolytes [11]. Despite these benefits, research and development emphasizes the importance of new material design to improve the power delivery and energy storage of EDLCs critical; broadening their future application by utilizing a large basis of nanostructured materials, including templated or hierarchical carbons [12], colloidal carbon aerogels [13], carbon nanotubes [14] and graphene [15].

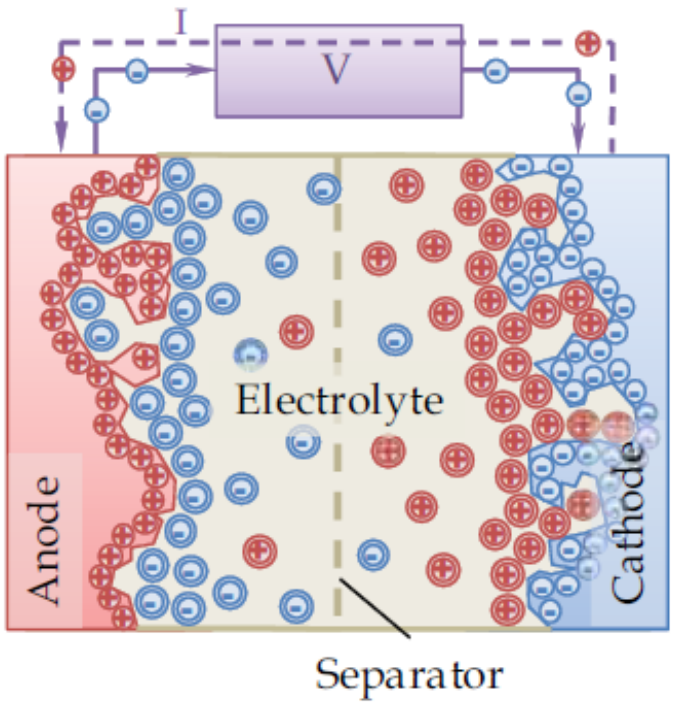

Figure 2: Depiction of a charged electric double-layer capacitor, Reprinted from [16] Copyright 2009 with permission from Electrochemical Society Interface

1.1.2 Pseudocapacitors

Materials for pseudocapacitive devices utilize a separate mechanism from EDLC, where the Faradaic redox reactions occurring due to thermodynamics reasons at defined potentials are responsible for an accumulation and release of charge during cycling. This reason divides pseudocapacitive materials from battery materials, where batteries make use of Nernst processes and the potential between the two electroactive materials ideally remains constant. Variations in electrode/electrolyte interactions encompassed by the pseudocapacitance mechanism depend on the choice of electrode material, where adsorption or intercalation processes are both considered, and described analogously [2]. A key aspect for the practical use of this mechanism relies on the repulsive forces between interacting adsorbed or intercalated electrolyte ions, which perform a significant role in broadening the operating potential for charge development. Conversely, a weak repulsive or attractive force between ions severely limits the

useful operating window [17]. Pseudocapacitive materials generate significant appeal due to the number of electrons transferred during the redox process (1 to 2) compared with EDL capacitive charging which amounts to ~0.18 electrons stored in the conduction band. Materials that exhibit multiple redox reactions within a specified operating potential further compliment this aspect of increased energy storage and can generate a more constant current during charge-discharge cycling. Figure 3 illustrates this case through depiction of pseudocapacitive capacitance developed from redox factor Θ, where a single redox reaction generates a peak response and consecutive peaks may promote continuous pseudocapacitive charging. Thus, pseudocapacitance can be 10 to 100 times greater than EDLC [18].

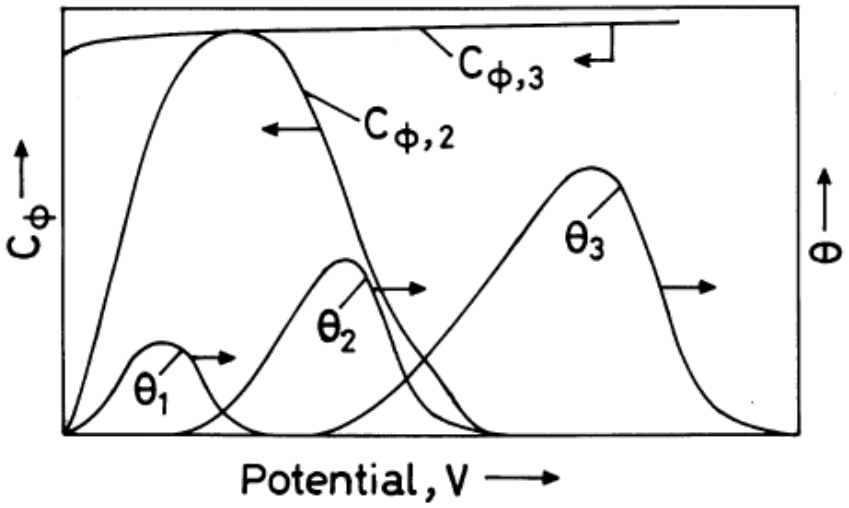

Figure 3: An increase in the potential window of a pseudocapacitive adsorption mechanism (Θ) with respect to voltage given single, pair and a triad of redox couples are involved, Reprinted from [17] Copyright 2000 with permission from Indian Academy of Science

1.1.3 Asymmetric hybrid Capacitors

Capacitors of asymmetric hybrid design incorporate different anode and cathode materials for purposes of expanding the operating voltage using the optimal range of electrochemical activity that pertains to each material. High oxygen or hydrogen evolution over-potentials of cathodic and anodic

materials are also advantageous when using aqueous electrolyte to further enhance the energy density as a result of an increased operating potential [19].

Early investigations in asymmetric designs with a Pb/PbO_2 and activated carbon (AC) asymmetric hybrid capacitor (AHC) have yielded devices with an energy density of ~20 Wh $\cdot kg^{-1}$ and an improved cycle life compared to lead-acid batteries. Promising electrode configurations of lithium titanate and AC, beginning with Amatucci et al. in 2001 [20], have since followed the success of asymmetric design. Naoi et al. have recently prepared a lithium titanate/carbon nanofiber composite for configuration with an AC electrode to achieve a power density twice that of the average commercial EC at 10 kW. kg^{-1} with an high energy density of ~29 Wh$\cdot$ kg^{-1} [21]. Another successful approach to AHCs by Wang et al. have used aligned titania nanotubes together with ordered mesoporous carbons as opposed to AC to obtain a configuration with a power density of 3 KW$\cdot$ kg^{-1}, energy density of 25 Wh$\cdot$ kg^{-1} and high stability following a 1000 cycle evaluation [22]. Complimenting the academic research initiative toward AHCs, Fuji Heavy Industries has commenced commercial pursuit of AHCs using a pre-lithiated AC together with an untreated AC, demonstrating recognition of the potential of hybrid configuration.

1.2 Physical/electrochemical processes in supercapacitors

Supercapacitor charging and discharging is described by the physical and electrochemical processes necessary for the development and release of an electrostatic or faradaic charge. Here, a brief insight is given to the development charge storage modeling, and the influential parameters pertaining to these processes.

The electric double-layer responsible for capacitive charge was initially introduced by Von Helmholtz in the nineteenth century with a model that over-simplified the behavior representing capacitive charge. It proposed that by charging a conducting solid with an applied potential ΔV, the ions from solution would develop an oppositely charged layer along the surface of the solid. This counter-layer would have a charge $\pm\Delta q$ to balance the parallel charge induced by the accumulation or removal or

electrons from within the solid, yielding a capacitance $C = dq/dV$ [23][24]. The two condensed "layers" of oppositely charged ions along the interface, thereafter named the double-layer, ideally remain electrostatic until the circuit between the polarized electrodes are closed, releasing the charge. Helmholtz model remained until Guoy and Chapman independently evaluated the thermal fluctuations that influence ions in solution to produce a joined Guoy-Chapman model that introduced the diffuse layer [25][26]. Assumptions made in the Guoy-Chapman model however, resulted in the inaccurate calculation of the double-layer capacitance that only approached true values near the point of zero charge (~0.1 V). Models later developed by Stern [27][28] and Grahame [29] overcame this setback by incorporating compact layers termed the inner and outer Helmholtz layers, in addition to the diffuse layer. The division of the compact layer was necessary to distinguish separate points of closest approach for cations and anions that are dependent on a number of factors, including the polarity of the surface, and choice of electrolyte/solvent pair. Modeling capacitive behavior with this approach provides the overall capacitance, C, to be divided into a series of capacitances: C_{H}, the Helmholtz layer capacitance, and C_{diff}, the diffusion layer capacitance [18] in Equation 1

$$\frac{1}{C_{dl}} = \frac{1}{C_H} + \frac{1}{C_{diff}} \qquad \text{Eq. 1}$$

The development of the double-layer, illustrated in Figure 4, summarizes the modifications and contributions of these models.

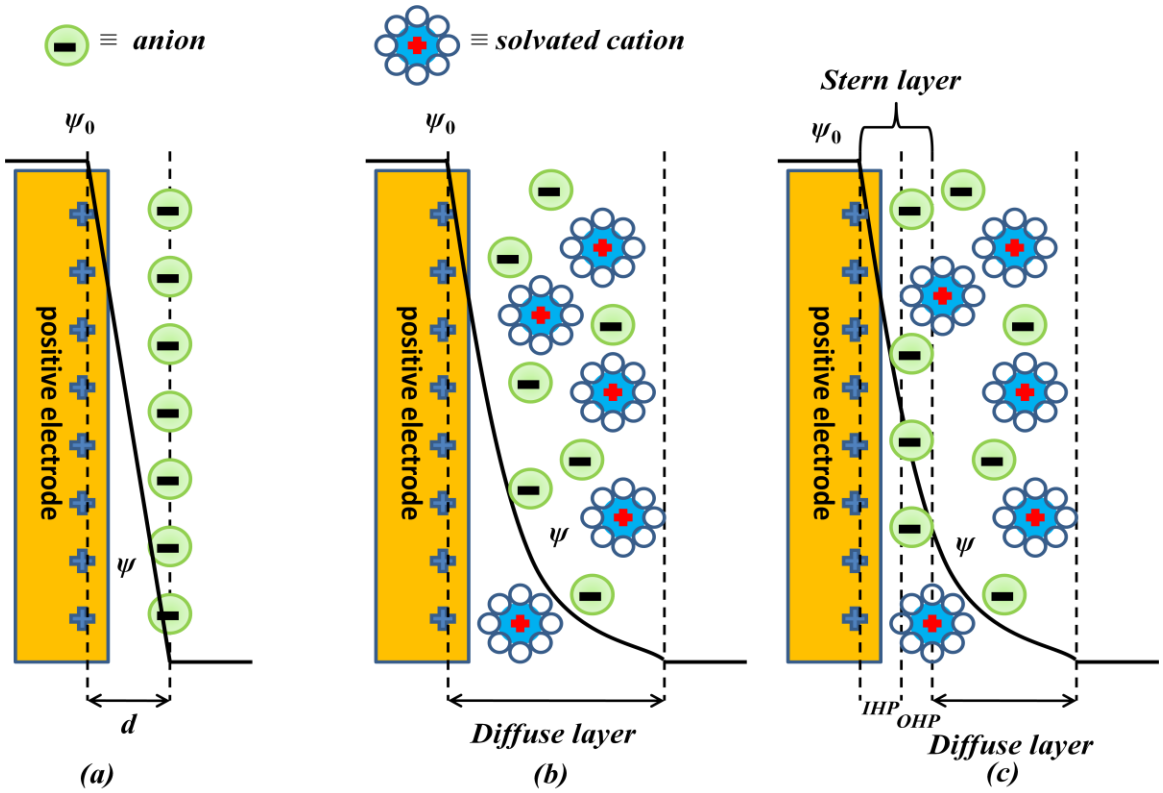

Figure 4: Progressive evolution of models describing the electric double layer at a positive electrode: (a) the initial Helmholtz model, (b) the Guoy-Chapman model, and (c) the Stern model, where the division of the inner Helmholtz plane (IHP) and outer Helmholtz plane (OHP) show specifically and non-specifically absorbed ions. The distance, *d*, in the Helmholtz model describes the double-layer distance, ψ_0 and ψ are the surface and electrode/electrolyte interface potentials, respectively.

Pseudocapacitance, as a separate mechanism for energy storage in ECs, occurs with the use of metal oxide and ECP materials to undergo redox reactions together with the electrolyte at the surface interface or within the material itself. An initial thermodynamic approach to describe the pseudocapacitance due to adsorption uses a Langmuir isotherm

$$\frac{y}{(1-y)} = K \exp\left(\frac{VF}{RT}\right) \qquad \text{Eq. 2}$$

where the parameters *K*, *F*, *R* and *T* are the reaction equilibrium constant, Faraday's constant, ideal gas constant and temperature, respectively and *y* being the variable quantifying the extent of the fractional specie either adsorbed on the electrode surface, θ, intercalated into the material by absorption, *X*, or converted through an oxidation/reduction coupling system, *[Ox]/[Re]* [2]. (Conway et al., 1997) Each mechanism involves the charge transfer of an electron(s) between the ionic species, measured by an extent, *Q*. As a function dependent upon the applied potential, *V*, the extent to which these reactions occur can be related as d*Q*/d*V*, which can be seen as analogous to the description of the electric double-layer capacitance [30]. Thus, the differential of *y* with respect to potential, *V*, and considering the pseudocapacitance to be $C_{pc} = q(dy/dV)$ provides a corresponding capacitance

$$C_{pc} = q\left(\frac{dy}{dV}\right) = \frac{qF}{RT} \cdot \frac{K \exp\left(\frac{VF}{RT}\right)}{\left[1 + K \exp\left(\frac{VF}{RT}\right)\right]^2} \qquad \text{Eq. 3}$$

Further investigation by Conway and Gileadi considered the lack of interaction terms between adsorbates using a Langmuir isotherm, and suggested a more realistic approach using a Frumkin type isotherm [31] and incorporating an oversimplified term for the lateral interaction energy (*exp±gy)* with the equilibrium constant. This has been helpful to explain a wider potential window that results from the additional energy necessary to overcome repulsion forces between the adsorbed species ($g > 0$) for further adsorption.

With the use of an asymmetric capacitor or hybrid-capacitor design, both pseudocapacitive and EDLC mechanisms can be employed through the integration of a carbon, carbon composite and/or battery electrodes. The intention of improving the energy density through the use of both mechanisms places an emphasis on their design, while the corresponding preservation of a high power density rests with

materials that possess a short electrolyte diffusion path length. This applies to both the EDLC and intercalation/adsorption processes in carbons and metal oxides/polymer matrices, respectively [32][33]. Current efforts by Wang et al. [22] employing lithium ion intercalation to increase the energy storage of asymmetric or hybrid capacitors and have shown success, particularly through their design of the electrodes composed of short aligned titania nanotubes and OMC, while others have used activated carbon with nanoparticle $Li_4Ti_5O_{12}$ [34], as shown by the schematic of such an AHC system in Figure 5.

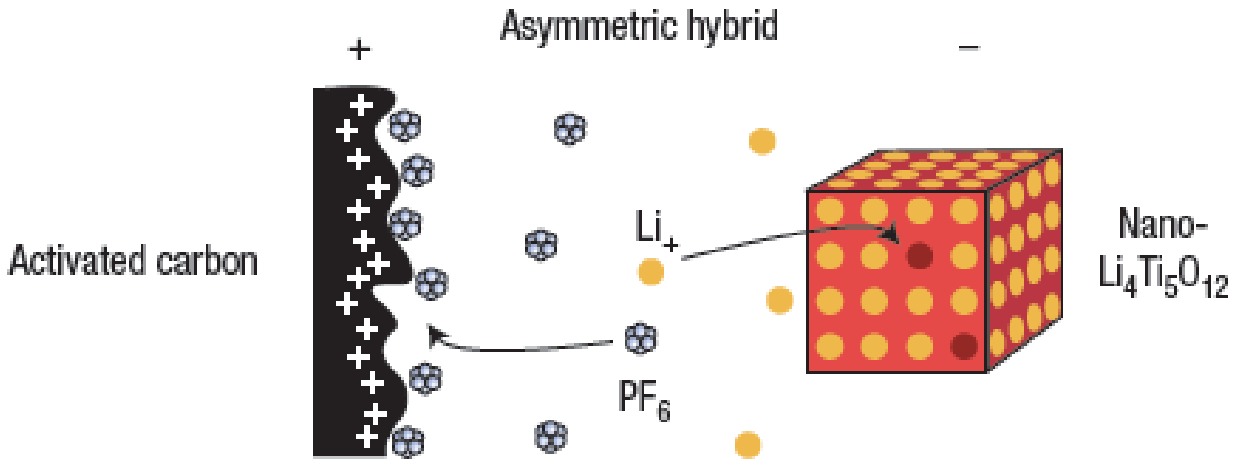

Figure 5: AHC: Schematic of hybrid carbon/nano-Li4Ti5O12 utilizing LiPF6, Reprinted from [34], Copyright 2005 with permission from Macmillan Publishers Ltd: Nature Materials.

2.0 Materials for supercapacitor electrode

2.1 General requirements of the materials

Electrochemical capacitor electrodes deviate from battery electrodes in a number of ways. In addition to a lack of notation for anode and cathode, both of which are generally a symmetric material, a list of properties are required by a material for it to be of proper use as an EC electrode:

- Long, stable life cycle ($> 10^5$)
- Lack of functional groups to undergo an irreversible redox process along the material surface
- High specific surface area ($1000 – 2000\ m^2 \cdot g^{-1}$)
- Thermodynamic stability beyond the potential window for operation
- A means to control the pore size and distribution of the material
- Surface wettability
- Mechanical resilience

The materials used in electrodes exhibiting either EDLC or pseudocapacitive behavior each have their respective advantages and disadvantages related to this list of requirements.

2.1.1 Effects of pore size and pore-size distribution

Electric double-layer capacitance is largely dependent upon the pore distribution and pore size of the carbon material. Carbons are generally designed to incorporate both mesopores (2 to 50 nm) and micropores (< 2nm) which are considered to be critical in the development of energy storage, and resulting power performance of the electrode [35]. While capacitance is theoretically proportional to the

surface area of the electrode, studies have shown a significant portion of obtained high-capacitance results in porous carbon electrodes are due to the presence of micropores. Mesopores remain necessary in maintaining high electrolyte mobility throughout the material for micropore accessibility, and by reducing resistances that impede addressing high power demands in a short time interval. A maximum capacitance and preserved power performance for EDLCs therefore requires the porosity of a material to be optimized [36].

2.1.2 Surface Area

Initial consideration towards surface area surrounded the concept that a large specific surface area directly resulted in a higher capacitance. As stated before, the investigations with highly mesoporous materials with high surface area, as well as contributions toward capacitance relative to pore size has since supported redirecting this significance toward micropores (< 2 nm) [37]. Multiple studies have promoted that a maximum EDLC is achievable in sub-micropores (0.7 – 0.8 nm), and with an increase in the micropore surface area, tailored materials are able to achieve an anomalous increase in specific capacitance.

2.1.3 Conductivity

The conductivity of carbon materials is largely influenced by two major factors: intrinsic material structure and functionality. By increasing the order or graphitization of carbon materials via increasing pyrolysis temperatures, a parallel increase in intrinsic electrical conductivity can often be observed [10]. However, a material requires investigation into the benefits of improving the conductivity, particularly in circumstances where a loss in active area may also result. Electrical conductivity can also be negatively affected by the incorporation of functional groups (oxygen, nitrogen, boron) which statistically have a higher rate of bonding at the edge plane. Here, they can consequently inhibit electron transport between

the intrinsic crystal structures of the material. Contrary to the loss in electrical conductivity, functional groups can serve to improve the ionic conductivity, or mobility, of electrolyte ions through the porous materials, improving their accessibility to active surface areas and reduce the ohmic drop of the electrolyte during charge/discharge [14].

2.2 Carbon as an EDLC material

Since initial commercialization, supercapacitors have primarily used carbon as an electrode material for EDLC due to the distinctive chemical and physical characteristics, appealing low cost, high surface area (1 - >2000 $m^2 \cdot g^{-1}$) and conductivity, and stability at high temperatures. A wide range of structures are attainable as a result of the four crystalline allotropes of carbon, including diamond (sp^3), graphite (sp^2), carbine (sp) and fullerenes (sp^2, distorted) [38].

2.2.1 Carbon Nanotubes

With a unique set of properties benefiting application as EDLC electrode material, carbon nanotubes (CNTs) have initiated considerable research in efforts to enhance EC performance. These nanostructured materials, which can be divided into two subgroups as either single-walled (SWNTs) or multi-walled (MWNTs), possess a high electrical conductivity, respectable surface area (~1315 $m^2 \cdot g^{-1}$) and considerable mechanical and thermal stability [39]. All of these beneficial properties offer a characteristically high power, exceedingly stable electrochemical capacitor [40][41]. Further support of their use rests in their ability to act as a substrate for unstable pseudocapacitive materials suffering mechanical degradation. Their use as a pure electrode material can result in a specific capacitance that ranges between 15 to 200 $F \cdot g^{-1}$, which is mainly affected by their production procedure, determining their morphology and purity, and any subsequent treatment techniques used [42]. Their capacity as a high

power device is owed to an accessible tubular network and high intrinsic conductivity, yet their low active surface area (< 500 $m^2 \cdot g^{-1}$) is responsible for a small energy density, and further production techniques are necessary to overcome agglomeration [43]. Tube entanglements can result in an irregular pore distribution that can decrease both the mobility and accessibility of ions throughout the material. The effect of this has been shown by Futaba et al. [44] using arranged carbon nanotubes with larger organic electrolyte ions to achieve a high energy density of 35 $Wh \cdot kg^{-1}$ and a lower operating resistance compared with an entangled network. Through chemical activation techniques the active surface area can be increased, however this comes at the cost of introducing functional groups that can affect the stability and electrical conductivity and require further optimization to evaluate whether an overall performance improvement is achieved. Carbon aerogels together with CNTs have been used to develop a composite through the uniform dispersion of the aerogel into the CNT matrix. This was achieved without affecting the original properties of the matrix to produce a composite with a high specific surface area of 1059 $m^2 \cdot g^{-1}$ and considerable capacitive ability (524 $F \cdot g^{-1}$), yet the difficulty in preparing this material is a significant hindrance regarding commercial production [45].

2.2.2 Graphene

In possession of a unique morphology described by a single-layered 2-D lattice structure of carbon atoms, the accessible flat surface area of graphene portrayed in Figure 6 isolates itself from any other carbon material for application in EDLCs [46]. In addition to having a high electrical conductivity, chemical stability and mechanical endurance similar to CNTs, graphene has surpassed CNTs for use in energy storage devices with a high specific capacitance ranging between 100 to 200 $F \cdot g^{-1}$, and recently achieved notably high energy density of 85.6 $Wh\ kg^{-1}$ using an ionic liquid [47][48]. While other supercapacitor materials rely on a fixed porous structure to transport and adsorb mobile ions, graphene layers are dispersed within solution having a high surface area, which ideally would remain accessible to

electrolyte ions for the development of EDLC [49]. Advantageous physical characteristics attributed to graphene for its use as a supercapacitor electrode material are listed in kind. First, the high theoretical surface area of 2630 $m^2 \cdot g^{-1}$ [50] is desirable in providing active sites for electrostatic adsorption of electrolyte ions for capacitive development. Secondly, as a zero-gap semiconductor with theoretical a resistance of 10-6 $\Omega \cdot$ cm [51] its inherent electrical conductivity supports rapid charging and discharging, characteristic of supercapacitors. Thirdly, the optical properties of graphene (monolayer) yield a ~2.3% absorbance of white light [52], allowing for the production of thin film electrodes with transparent qualities. Lastly, a high tensile strength of 130 GPa [53] imparts structural stability required for its use as either a singular electrode material, or a scaffold for the integration of pseudocapacitive materials in efforts to further enhance the overall energy density. Adding to this last advantage, graphene also possesses a chemical resistance suitable for use as a substrate material.

Several synthesis methods are presently available that yield graphene nanoplatelets. The earliest method capable of yielding single layer graphene sheets utilizes a mechanical "cellophane method" where tape is applied to graphite and then removed. This method is effective in investigating the physical properties of graphene; however it is not practical for the production of large quantities. Bulk quantities can be produced via the unzipping of CNTs through either a physical, electrochemical or chemical process to yield narrow width graphene nanoribbons. Nanoplatelets and nanoribbons can also be derived from chemical vapour deposition (CVD) processes. Alternatively, chemical exfoliation methods have been developed using small molecule nitric or sulphuric acid to intercalate between the graphene sheets. Thermal evaporation or sonication techniques can then be applied to separate these layers into individual sheets to produce what is known as graphene oxide (GO). Subsequent thermal, electrochemical or chemical reduction processes can then be carried out to yield graphene nanoplatelets with the latter often with the use of hydrazine or sodium borohydride [54]. Efforts to produce single-sheet graphene are hindered by its inherent instability and tendency to stack to form graphene nanoplatelet structures (<100 layers). This problem can be overcome through added functionalization or nanoparticle deposition onto the basal plane of the sheets, providing steric hindrance. Graphene performance, relative to preparation

procedures have been investigated, with the largest specific capacitance derived from a chemical reduction procedure.

Doping of GNP into the carbon lattice in order to add a pseudocapacitive species, and increase the solubility and dispersion of GNP nanostructures can be done by incorporating nitrogen precursors into the synthesis procedure [55]. Yet, doping the structure can have an adverse affect on the mobility of electrons within the basal plane as well as along the edge plane, where functional groups may serve to effectively impede electron transfer.

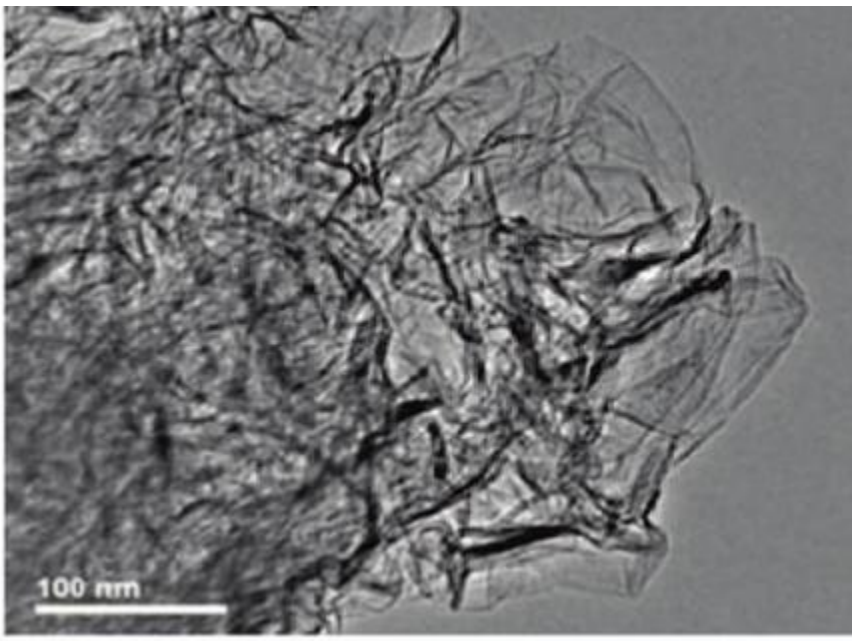

Figure 6: Imaging by TEM of individual graphene sheets obtained from chemical modification are observed around the edges of the particle. Reprinted with permission from [49] **Copyright 2008 American Chemical Society.**

GNP Material Preparation

The GNP materials used in the following works were developed through a chemical exfoliation technique to generate GO. The precursor powdered graphite and all chemicals used in the synthesis procedure were supplied by Aldrich to ensure high purity materials are maintained. Preparation of the GO material was achieved by an initial acid treatment (conc. 18 M H_2SO_4) of graphite and NaNO3 in a

stirred ice bath. Additional oxidizing agent KMnO4 was gradually added to the stirred mixture over time, and the progressive addition of de-ionized (DI) water followed. Termination of the reaction was done by the addition of H_2O_2. The reaction was then proceeded by wash filtration of the slurry using copious amounts of HCl (5% aqueous) and several centriguation and additional wash (DI water) cycles. These purification steps are necessary to remove any impurities including residual salts, acids and metals from the GO product. Drying of the GO was done in fume hood for 24h followed by dehydration within a dessicator for a subsequent 48h.

Prepared GO was dispersed in DI water through sonication, and the pH adjusted to 9-10 using 5 wt % Na_2CO_3 as the initial step to convert GO to GNP. Following sonication, $NaBH_4$ dissolved in 50 mL DI water was added to the mixture and subsequently stirred at a moderate temperature for 36 hours. The reduction process was repeated once to remove any residual oxygen groups present on the GNPs.

2.2.2.1 Performance of Graphene in Literature

Research conducted by Stroller et al. pioneered the study of graphene, therein noted as chemically modified graphene (CMG), for its use in electrochemical supercapacitors [56]. Their CMG, prepared through a similar reduction procedure used in the following work, demonstrated a good propagation of charge through cyclic voltammetry (CV) evaluation and obtained a high electrical conductivity (~2 x 10^2 $S \cdot m^{-1}$). The length of the ion diffusion path for CMG was exemplified through A.C. impedance analysis, where a short Warburg impedance region was noted to illustrate a significant decrease of the ion resistance relative to characteristic porous materials used in supercapacitors. By following with a chemical reduction procedure, Wang et al. produced graphene materials that further supported the ability of GNP to rapidly develop an electric double-layer capacitance, and subsequently achieved the highest reported specific capacitance for graphene (205 $F \cdot g^{-1}$) [57].

2.2.2.2 Graphene Composite Materials

As a substrate material, graphene has been investigated together with electronically conducting polymers and transition metal oxides to develop synergistic materials that exhibit significant pseudocapacitive energy storage. The primary characteristics sought after in such hybridized structures are an accessible high surface-area, that correspondingly facilitates high ion and electron conductivity. Efforts to accomplish this are illustrated in studies such as a graphene/polyaniline paper composite prepared by Wang et al. [58], where they concluded an increased specific capacitance from 147 $F \cdot g^{-1}$ (pure graphene) to 233 $F \cdot g^{-1}$ with a maintained stability.

2.2.2.3 Transparent Graphene

The electrical and mechanical properties reported for graphene has attracted attention in evaluating the flexibility and transparency of this material for potential use in optical and portable electronics. A recent review by Liang et al. supports graphene as a strong future alternative to indium tin oxide (ITO) and fluorine tin oxide (FTO) for use in photovoltaic cells [59] for clean energy. GNPs are equally applicable for thin-film supercapacitor electrode fabrication, where a high mechanical stability allows flexibility to be maintained. Investigation towards this field of application has recently yielded several methods to produce thin-film electrodes, including spin-coating [60], dip-coating [61][62], direct CVD[63] and vacuum filtration[64] that have demonstrated favourable electrical properties and maintained structural integrity while bending.

2.3 Pseudocapacitive Electrode Materials

Pseudocapacitors contrast conventional EDLC by employing a Faradic charge transfer to establish a capacitive charge. Although appearing similar to batteries, the charge transfer is a result of a thermodynamic relationship that manifests through adsorption, reduction/oxidation and/or intercalation of an ionic species [18]. Transition metal oxides and ECPs as pseudocapacitive materials owe their appeal to a higher capacitive charge development acquired with their use, yet often possess a lack of stability from mechanical stress or by undergoing soluble transition states during charge/discharge. Addressing

the former through the integration of EDLC and pseudocapacitive materials together has been successfully done to develop superior composites, while the latter largely depends upon the electrolyte used, polarity and operating potential of the electrode.

2.3.1 Transition Metals

A number of metal oxides, including ruthenium (RuO_2) [65], iron (Fe_3O_4) [66], vanadium (V_2O_5) [67] tin (SnO_2) [68] and manganese (MnO_2) [69] have been examined for suitability as a pseudocapative material. The transition oxidation states of these metals, at particular voltages, give rise to either a local or constant charge depending on the number of redox couples within the defined operating potential. In addition to relying on multiple transition states, the performance of these materials depends on the electrical conductivity which can vary not only between metals but among the variety of polymorphs of each that can be produced from a variety of procedures, with some being more conductive than others [70]. Hydrous RuO_2 has shown a large capacitance (1580 F g^{-1}) [71], however investigation towards inexpensive, health conscious alternatives suggest manganese oxide [72] (698 F g^{-1} per mass active material [73]) as a strong candidate.

2.3.2 Electrically Conducting Polymers

Electrically conducting polymer (ECP) groups have aroused great interest as a family of synthetic metals due to their rapid, reversible redox reactions and high doping ability [74]. As such, polymers that have drawn attention in the development as supercapacitors include polypyrrole (PPy), polyaniline (PANI), poly(3, 4 ethylenedioxythiophene) (PEDOT) and their derivatives, owing to their intrinsic properties and commercial appeal. Benefits to their use include relatively high conductivity, low cost, and ease of synthesis [75]. Through electrochemical deposition or chemical oxidation methods with the option of surfactant use (subsequent removal processes may then be required), nanostructures such as

nanotubes, nanowires and nanospheres can be produced [76]. Similar to metal oxides, a pseudocapacitance mechanism is developed through a redox reaction as the polymer transitions between oxidation states. Through the involvement of the entire volume in accumulating charge, it surpasses other EC materials that are reliant solely on electrostatic surface charging (carbons) and has been able to obtain high specific capacitance values in excess of 400 F g^{-1} [77]. The main advantage of ECPs; however, is responsible for their major drawback as a short-lived material, with poor stability being a result of volumetric changes that occur during doping/dedoping (insertion/extraction) of the counterions, a process illustrated by Figure 7.

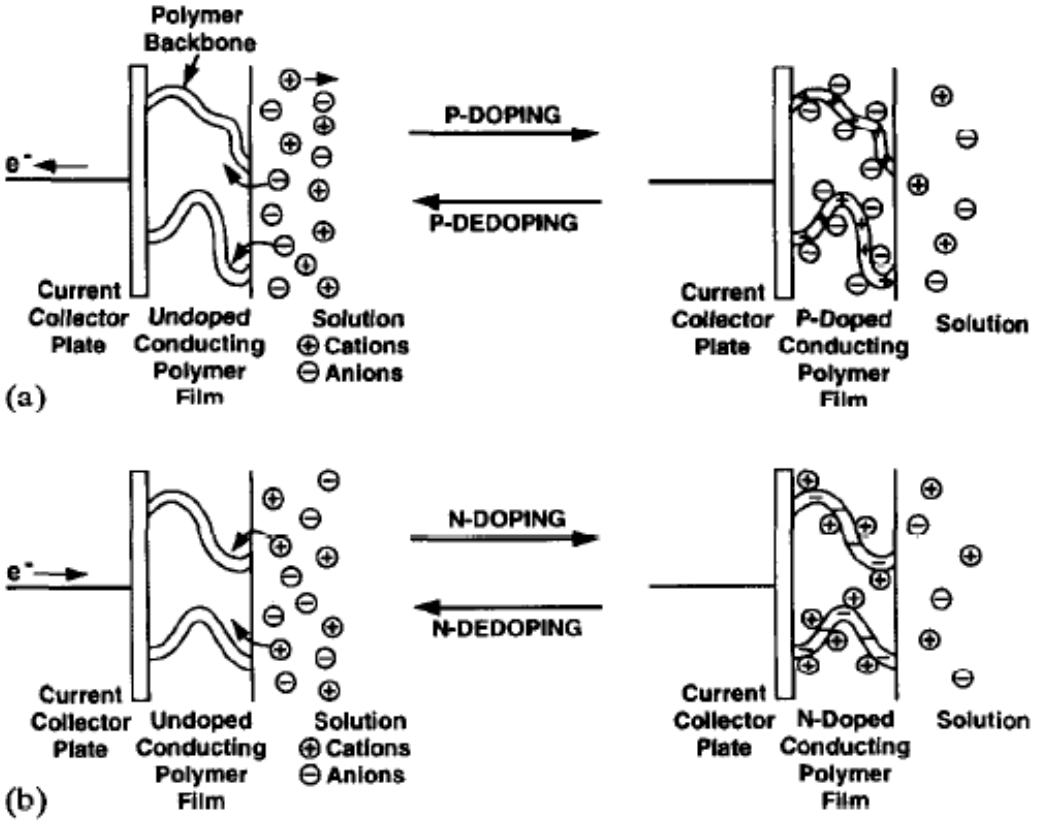

Figure 7: Diagram representing the p-doping (a) and n-doping (b) of polymers as they undergo charging and discharging, Reprinted from [78] Copyright 1994 with permission from Elsevier.

This process involves the swelling, shrinking, cracking and/or breaking of the polymer. In addition to this problem, a small working potential can be expected in order to avoid isolating states and/or polymer degradation due to over oxidation of the material [74][79]. These problems make it necessary to develop composite designs that utilize a carbon support structure with the polymer matrix, or through deposition of the polymer on a carbon surface to reduce these mechanical stresses and improve cyclability. Polymer/carbon composites obtained with high specific capacitance, respective cycle life and facile synthesis methods illustrates the effectiveness of incorporating carbon to help alleviate this problem and has subsequently been shown to increase porosity of the ECP. Work performed by Yan *et al.* has shown a high capacitance of 1046 F g^{-1} in 6 M KOH by the incorporation of graphene with PANI. Furthermore, by the addition of ~1% CNTs, a retention of 6% of the original capacitance after cycling remained, thus improvements in performance through enhanced electrolyte accessibility and diffusion rates are achievable [80].

Adding to ECPs high capacitive ability, they have shown good application in asymmetric capacitor configurations by operating within their own optimal potential range to provide their use as either an anodic or cathodic electrode similarly observed in batteries. The outcome of ECPs for their application in ECs rests on their development as hybrid capacitors using carbon supporting materials for future applications [81].

2.4 Electrolytes for use in Electrochemical Supercapacitors

Electrolytes play a critical role in development of the electric double-layer in supercapacitors and for the reversible adsorption, intercalation redox processes occurring in pseudocapacitive materials. Hence, their molar conductance and subsequent dependency on the cell operating temperature is a contributing factor when determining the equivalent series resistance (ESR). In addition, due to the square relation of the operating potential with respect to equivalent energy density, the electrochemical stability range is significant. Aqueous electrolytes have a smaller 1 V window in comparison to

nonaqueous electrolytes 3.5 to 4 V range. Each electrolyte inherently has their benefits and disadvantages that ultimately have to be weighted.

2.4.1 Aqueous Electrolytes

The advantages of using aqueous electrolytes include its availability and subsequent low cost, in addition to its high conductivity and low health concerns; however, their primary disadvantage is their thermodynamic limitations for electrochemical decomposition in a relatively narrow potential range (1.2V). An operating range of 0.8 – 1.0 V is often employed to avoid the loss of electrolyte, introduction of oxygen or hydrogen gasses that can lead to additional losses in current from competing faradaic reactions, gas formation and ultimately limited accessibility of the electrolyte ion to the active surface. Aqueous potassium chloride (KCl) electrolyte is used in the following projects to emphasize a high-power, low cost design with consideration towards green energy.

2.4.2 Organic and Ionic Liquid Electrolytes

Organic electrolytes are currently used in commercial ECs because of their voltage window, and often operate at potentials above 2 V (2.2 – 2.7 V) which can be floated as high as 3.5 V for short periods [82]. Polar aprotic electrolytes used in high-tech capacitors include acetonitrile and propylene carbonate; however the benefits of using propylene carbonate to reduce the safety concerns of acetonitrile are weighed down by an almost three-fold increase in electrolyte resistivity [83]. Organic electrolytes in general suffer from a noted increase in resistivity detrimental to its power performance and a number of safety issues arise with the incorporation of a toxic, flammable material. These solvents also require purification processes to remove any residual water content which can lend to the corrosion of the current collectors at high operating potentials.

Ionic liquids (ILs) are relatively new electrolytes xist as solvent-free molten salts at room temperature that possess high thermal and electrochemical stability in excess of 3 V made possible by the chemical and physical properties of the chosen cation and anion [84]. Being composed entirely of liquid ions at ambient temperatures necessitates large sized ions, and as a result their ionic mobility is significantly reduced to a few milliSiemens per centimeter at ambient temperature.

2.5 Project Objective

The primary objective of these works is focused towards exploiting the uniquely favourable physical and electrochemical properties of GNP described above for its application as a supercapacitor electrode material. The investigation of GNP thin-film, transparent electrodes is conducted to evaluate their capacitive performance at various thicknesses and its effective ability to capacitively charge at ultra-high charge rates. The integration of dispersed graphene with CNTs in thin films seeks to further increase the surface area and facilitate structural designs to favour electrolyte access and electron mobility. The use of GNP as a scaffold material for ECP polypyrrole is evaluated to contrast its integration with a psuedocapacitive material. These projects are investigated with the purpose of advancing the energy density of supercapacitors via the use of inexpensive and environmentally conscientious precursor materials. This is in the effort to confront the problems of low energy density and higher cost which present EDLC supercapacitors face.

3.0 Techniques for Physical and Electrochemical Characterization

Proper characterization of each material is necessary to gain understanding of the specific compositional, structural and electrochemical aspects which are responsible for the results obtained. Thus, several techniques are employed to address this challenge. The electrochemical techniques are utilized in order to ascertain the capacitance, energy, power density and resistances present in each work. Physical characterization techniques further assist in evaluating the chemical, morphological and optical properties of the constructed film electrodes. The following section is provided to detail the characterization techniques and their respective principles that facilitate these efforts.

3.1 Scanning electron microscopy

A common and versatile technique used by international research scientists for the evaluation of surface morphology, atomic composition and electrical conductivity of a broad array of materials is scanning electron microscopy (SEM). These analytical techniques are permitted through the irradiation and raster scanning of a designated rectangular surface area with a highly focused electron beam. Signals emitted through this process include x-rays, secondary electrons and backscatter electrons, while secondary electron detectors are most common to yield a high resolution nanoscale image for the useful understanding of the morphology and surface structure of a material. The secondary electrons responsible for yielding images are ejected from an orbital a few nanometers from the surface of the sample [85]. This report utilizes SEM primarily to investigate the structural design and surface morphology of the synthesized electrode materials.

3.2 Transmission electron microscopy

High resolution imaging of a material through transmission electron microscopy (TEM) technique is utilized to magnify a noted area of interest via an electron beam and project it for view.

Rather than detecting backscatter or secondary electrons, this form of microscopy uses an applied high voltage for electrons to transmit through the specimen, where they interact as they pass through and are subsequently collected and processed. Nanometer scale imaging of the crystalline structure of thin materials is achievable through this technique and applied for investigation to compliment SEM imaging of materials.

3.3 Thermogravimetric analysis

A test which characterizes the change in weight of a sample with respect to a constant rate temperature increase in an ambient atmosphere (N_2) is used to evaluate the thermal properties of a specimen including its stability, decomposition temperature and moisture content. It can also assist in quantifying the presence of multiple materials present in a composite specimen. These properties are utilized in this work to determine the weight percentage of a composite film.

3.4 Ultraviolet-visible Spectroscopy

Ultraviolet-visible (UV-Vis) spectroscopy is an absorption spectroscopy technique that uses light in the visible and adjacent range to either be either absorbed or reflected by the specimen. This characterization technique can be used with the Beer-Lambert law to measure the absorbance of a specimen over a wide range of wavelengths, with the Beer Lambert law expressed as:

$$A = log_{10}\left(\frac{I_0}{I}\right) \quad \text{Eq. 4}$$

where A is the measured absorbance, I_0 the incident light intensity for a given wavelength and I the intensity of the transmitted light.[86] Corresponding transmittance T can be derived from Eq. 4 by using the following

$$\%T = e^{-A \cdot 100\%} \quad \text{Eq. 5}$$

In this work, transmittance at the 550 nm wavelength is ascertained with respect to a material's optical transparency.

3.5 Half cell electrochemical testing

Measurement of capacitance in the development of electrochemical supercapacitors is necessary to evaluate performance, application and trouble-shooting when designing and re-designing active electrode materials. This analysis is done through quantitative measurement of experimental variables with a respective relation to a developed capacitance. Two-electrode full cell experimentation is possible for supercapacitor characterization; however this form of testing does not provide specific characterization of the material over a give operating potential, rather it describes the overall behavior of both electrodes. To this effect, half- cell electrochemical testing is useful to assess the electro-active behavior of a single electrode specimen over the complete voltage window of the electrolyte to properly ascertain its applicable usage.

Half-cell electrochemical analysis is performed with the use of the following electrodes: i) a working electrode, generally comprised of a conducting substrate and deposited active material; ii) a reference electrode; and iii) a counter electrode. In the works presented, half-cell measurements were conducted with either a glassy black carbon electrode or metal ring serving as a substrate or current collector for the active material; a platinum mesh counter electrode; and a mercury/mercury(I) chloride standard calomel electrode (SCE) (0.244 V vs. standard hydrogen electrode). A potentiostat was used to perform the electrochemical techniques described in the following on the working electrode within a defined potential window.

3.5.1 Cyclic Voltammetry

Cyclic voltammetry (CV) provides a useful technique in screening for potential capacitor materials in a relatively swift procedure. This technique is performed by cycling a linear potential-sweep between two defined voltages determined by the electrolyte decomposition limits, and is generally aided by a reference electrode within the described three electrode half-cell. The potential applied to the electrode varies linearly with time yielding a time-dependent dynamic responsive current which is recorded by computer software.

Several predetermined constant potential-sweep rates v_s = d*V*/d*t* are used in the following experiments to evaluate the capacitive charging current *i* passing through the material described by the following

$$i = C\frac{dV}{dt} = Cv_s \qquad \textbf{Eq. 6}$$

Ideal double-layer capacitance through CV analysis is depicted by a constant and equivalent charging and discharging current $\pm i$ resulting from a constant sweep rate $\pm v_s$; represented by a rectangle within a voltammetry plot of the current with respect to applied potential illustrated in Figure 8. Supercapacitors exhibiting double-layer capacitance approach ideality with a constant current measured through a majority of the charging process, deviating slightly from this relation due to diffusion resistances in the initial charging or discharging process of the double-layer for the respective voltage limits. Other materials may not exhibit constant capacitance as a result of material resistances or may display potential specific Faradaic reactions depicted by peaks in the response current due to reversible pseudocapacitive processes typically shown in metal oxides and conducting polymers. Characteristic profiles of these capacitive mechanisms from CV technique are also shown in Figure 8. Determining the capacitance *C* or specific gravimetric capacitance C_p from CV experimental results often requires the integration of the current response in a cyclic voltammogram and can then be calculated by the following [87]

$$C = \frac{\int i \cdot dV}{\Delta V \cdot v_s} \qquad \textbf{Eq. 7}$$

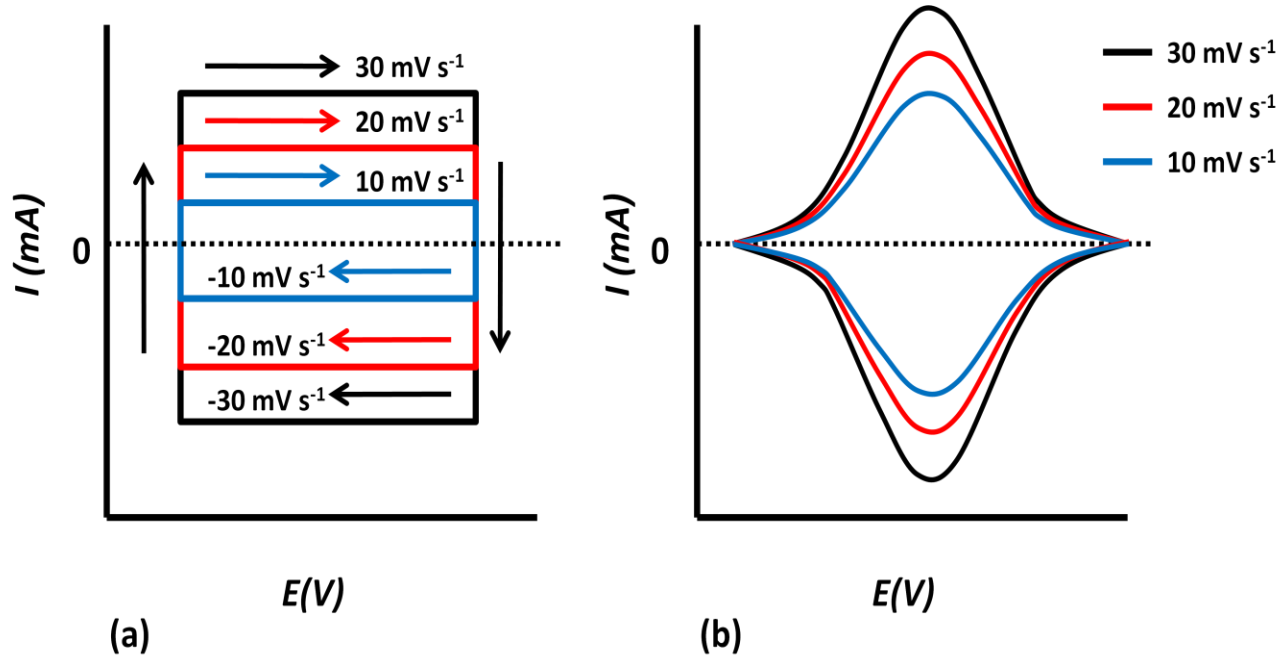

Figure 8: Cyclic voltammograms comparing (a) an ideal capacitor and (b) a localized and reversible pseudo-capacitive reaction for an electrode thinly coated by a redox material at increasing scan rates.

3.5.2 Charge or Discharge Chronopotentiometry

Interfacial charging of an electroactive material in contact with a solution electrolyte will behave capacitatively when a constant current density *i* is applied, developing a potential difference linearly with time across the cell. The capacitance is describe by

$$C = \frac{\Delta q}{\Delta V} \qquad \textbf{Eq. 8a}$$

where

$$\Delta q = \int i \cdot dt \qquad \textbf{Eq. 8b}$$

and can be used with charge or discharge constant current testing to determine the capacitance according to the following [88]

$$C = \frac{\int i \cdot dt}{\Delta V} = i \cdot \frac{\Delta t}{\Delta V} \qquad \textbf{Eq. 9}$$

where $\Delta t/\Delta V$ is the inverse slope of the response curve obtained from charge or discharge measurements, ΔV is between the limiting potential difference for electrolyte decomposition and current i is removed from the integral due to it being constant.

This is a conventional procedure used in testing electrode materials for use in batteries and supercapacitors alike, involving the charging of the electro-active material at constant current and subsequently discharged at constant current. Variation to this testing undergone in the following report involves changing the rate of the charge or discharge current.

An ideally polarized electrode exhibiting model reversible capacitance is described by a constant linear potential increase and decrease during charge and discharge. During experimentation however, this may not be the case. Consideration can be given towards Faradaic processes that occur at distinct potentials including those approaching the decomposition potential limits of the electrolyte, or initial diffusion limitations within microporous structures. When a Faradaic process occurs the applied current density i will be divided between a double-layer charging current, i_{dl}, and i_F pertaining to psuedocapacitive chemical processes taking place at the electrode surface. Reversible pseudocapacitive processes can exhibit capacitive charging similar to that of the double-layer if there are multiple redox reactions occurring continuously; otherwise a dynamic change to the slope of the potential will occur with a range dependent upon the interaction term, g, between the adsorbed species as discussed in Section 1.2. The potentials at which pseudocapacitive processes are observed to take place in chronopotentiometry techniques can be supported through CV analysis.

3.5.3 Impedance Spectroscopy

Measured response functions of the potential to changes in time-dependent current charging or vice-versa are shown to be useful in the characterization of capacitance. In addition to the CV and chronopotentiometry techniques, the response function of an alternating current (ac), generated by application of an alternating voltage (av) to an electrode interface is useful in characterizing the pseudocapacitive processes a material exhibits. The imaginary component, Z'', of the overall impedance Z response relates to the capacitance of the electrode through the equation $Z'' = 1/j\omega C$ [89]. This relation has placed the ac impedance technique as a principle method for capacitive behavior analysis. An ac impedance analysis provides a means of measuring capacitance as a function of the frequency, ω. In addition, evaluation of the phase relation between Z and Z'' impedances generated by this procedure can be achieved. Important circuit elements of the electrode structure, including the ESR, and potential-dependent Faradaic resistances (e.g. pseudocapacitive, leakage resistance) can be separated and determined using this technique.

The examination of fundamental and applied characteristics of supercapacitors can be performed using electrochemical impedance spectroscopy (EIS) over a wide range of frequencies, (10 kHz to 10 mHz). Supercapacitors yield characteristic observations by plotting the complex-plane of impedance (Nyquist) which may include semicircular forms occurring at high frequencies; a 45° region (Warburg region) of transition between high and low frequencies representative of ion diffusion resistance and a non-vertical slope at low frequencies. The ESR of the electrode, comprised of contact, separator and solution resistances summarized together as the real impedance, can be obtained from the intercept of real impedance at high frequencies.

The 45° phase angle observed in the complex plane of Z, often termed the Warburg impedance region, can arise for two separate reasons for an EC electrode undergoing ac impedance testing. Transitioning from the Faradaic resistance parallel to capacitance to diffusion control demonstrates a

dependence of both imaginary and real components of Z on the square-root of ω^{-1} or $(t)^{½}$ from the principles of particle diffusion in a concentration gradient [90].

In a separate case, unrelated to diffusion reason, a phase angle of the complex plane arises that is independent of ω. This is often observed in high-area, porous electric double-layer materials, where a network of distributed RC elements down the lengths of the pores describes the electrochemical behavior, as discussed in the model presented by de Levie [91].

A Nyquist plot in Figure 9 demonstrates characteristic electrochemical behaviour observed by supercapacitor electrodes. At low frequencies impedance can be reduced to a familiar term $Z_E = 1/j\omega C$. The Warburg impedance region at low frequencies is due to ionic solution resistances present within the pore structures of the electrode and are governed by the electrolyte conductivity and electrode porosity. This has been termed the equivalent distributed resistance (EDR). Evidence of this behavior has been shown by Kotz [92] using a constant electrode material and simply increasing the active electrode thickness, thereby increasing the pore number and a subsequent increase in observed EDR.

Due to non-ideal charging processes from macroscopic variations in current path lengths through the electrode (inconsistencies in electrode thickness) or microscopic variations in the electrode structure effecting adsorption processes, a non-vertical slope at low frequencies exists for real electrochemical capacitors.

At low frequencies where the imaginary component of impedance dominates the overall impedance, a close approximation can be made to the ideal capacitance of the material achievable under direct current (dc). The following equation can then be used to obtain the overall capacitance [93]

$$C = -\frac{1}{2\pi f Z''} \qquad \textbf{Eq. 10}$$

In addition, the phase angle of the overall impedance at low frequencies approaches 90° to exhibit and near vertical slope.

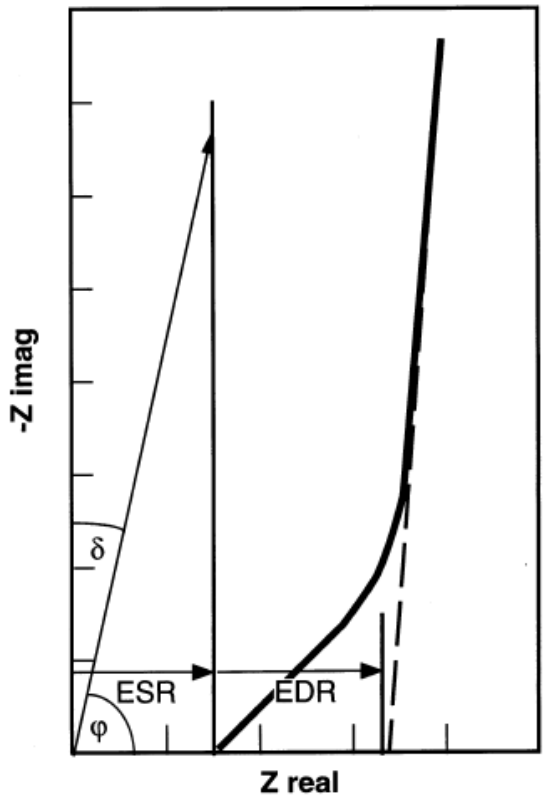

Figure 9: Nyquist impedance diagram comparing the ideal vertical impedance of a capacitor (thin line) and that of an EC supercapacitor (thick line). The equivalent series resistance (ESR) is derived from the intercept of the real impedance axis, followed by the equivalent distributed (EDR) of a porous electrode, Reprinted from [92] Copyright 2000, with permission from Elsevier.

3.6 Energy and Power Density

The assessment of energy and power density provided by a supercapacitor is desirable for any relevant application, particularly for their use in applications with high load demands within short time intervals. The specific power density (W kg^{-1}) is the rate at which the stored energy can be supplied per unit mass, and can be plotted versus the specific energy density (Wh kg^{-1}), or energy storage capacity of the device per unit mass, to yield a plot ubiquitously termed the Ragone plot which is often used to evaluate and compare the respective performance of electrochemical energy storage devices (including batteries and fuel cells). Through a Ragone plot of ECs and batteries, initially illustrated in Figure 1, a trend in diminishing energy density with increasing power density can be observed for all electrochemical

energy storage devices. This can be explained through the rationale that an increase in current density *i* will lead to a corresponding increase in polarization losses as well as a reduction in cell voltage.

3.6.1 Energy Density

The theoretical maximum energy storage of an electrode or device can be easily quantified by the Gibbs energy of charging, *E*, required to develop an electrostatic charge. Reiterating from Eq. 8 and 9, the charge of a capacitor, Δq, is directly related to the applied potential ΔV and capacitance *C* by the following $Q = C \cdot V$ as defined by capacitance. Accumulation of charge along the surface requires additional work to overcome subsequent repulsions between like charges. The resulting energy stored as charge is then

$$E = \frac{1}{2} q \cdot V = \frac{1}{2} C \cdot V^2 \qquad \textbf{Eq. 11}$$

hence, the importance of a large operating potential in the resulting energy stored by the device is apparent by the square voltage term.

It is observed through Ragone plots that an increasing energy density lowers the power performance of electrochemical storage devices and vice-versa. Thus, the relation between the energy density (*E* with respect mass or volume) and power density is important to evaluate in order to understand the relative performance between these two properties for practical application.

3.6.2 Power Density

The power density defines the rate of power delivered by a device of certain mass at a specified current density. Power densities are influenced by kinetic polarization at overpotentials, and ohmic resistances of the electrolyte and intrinsic material structure. The latter effect mainly determines the loss in power and is more prevalent in EDLC, where Faradaic reaction processes do not occur (ideally); however, when considering pseudocapacitive materials, kinetic polarization effects come into play, depending on the reversible potential of the cell.

The maximum power deliverable by a device, P_{max}, has been derived by Miller considering the capacitance of the material in series with an ESR, R_{ESR} [94]. Through this simplified circuit analogy the following equation can be obtained

$$P_{max} = \frac{{V_i}^2}{4R_{ESR}} \quad \textbf{Eq. 12}$$

This power is often used to normalize average or normal power deliverable by the device or system with respect to the number of time constants for discharge and energy delivered or dissipated. These factors are important to consider in application, in optimizing the energy and power delivery and minimizing the capacitor energy that dissipates internally.

The relation between the energy density, E_d, of a system and the respective power density P_d performance is evaluated by the simple ratio

$$\frac{E_d}{P_d} = \Delta t \quad \textbf{Eq. 13}$$

where Δt is the rate of discharge of the capacitor. This ratio is independent of any factors detrimental to both the power and energy densities.

4.0 Ultra-thin and transparent graphene nanoplatelet film electrodes

4.1 Introduction and objective

A primary challenge in the design process of miniaturizing portable, multifunctional electronics, optoelectronics and wireless sensor networks continues to be the integration of an energy source able to efficiently address power demands and perform beyond the lifetime of the device being powered [95][96][97][98]. Recent progress in supercapacitor research has focused on producing light weight, high performance capacitors which are flexible and optically transparent for use in a wide variety of applications including hybrid vehicles and personal electronics [4]. These properties are especially desirable in the field of personal electronics such as cell phones, laptops, and mp3 players where aesthetics and flexibility are becoming increasingly important [99][98]. While efforts to design improved high-power Li-ion batteries remain optimistic [5][100], the fundamental governing power density remain reliant on sluggish reaction kinetics during charging and discharging which may also result in material degradation, ultimately leading to a short lifetime of hundreds to at best thousands of cycles. This is in addition to achieving small energy densities within cycling times less than 20 s [7], and lack of transparency for optoelectronics application.

Carbon based materials have been the subject of extensive research for use in supercapacitor applications due to their good electrical conductivity, corrosion resistant in aqueous electrolytes, long cycle life and highly modifiable nanostructures[101]. Although there are reports on graphene for supercapactiors [102][49], this work presents an original fabrication of ultra-thin GNP films which are optically transparent and demonstrate excellent capacitive behaviour. The use of the ultra-thin GNP has the following advantages: (1) Substantial mechanical strength of the graphene materials allows for the formation of flexible and robust thin films, where thickness of these films can be reduced to 25 nm; (2) The transparency of the film allows for the realization of a supercapactior electrode for use in transparent electronics applications; (3) The high capability of graphene for electron mobility [46] can eliminate the

necessity for a metal current collector, thus avoid the resistances owing to a metal-carbon electrode interface and yield a lightweight architecture at a reduced cost; (4) Graphene can be solubilized in a number of solvents enabling it to be printed on a wide range of suitable substrates for integration with printable electronics.

The transparent, flexible graphene films obtained in the following are evaluated for their capacitance related to film thickness and charge propagation with increasing scan rates. Further investigation is done here to observe performance at ultra-high CV scan rates (range of 0.1 to 200 V s^{-1}) for the evaluation of its potential as a high-power density supercapacitor electrode material.

4.2 Experimental

Graphene oxide (GO) was synthesized though a modified Hummers [104][105] method as described earlier. Reduction of GO to GNP through the procedure described previously is applied twice to ensure sufficient restoration of the GNP sheets.

The ultra-thin films were prepared using a vacuum filtration method as follows, where a well dispersed, 0.2 mg · mL^{-1} solution of GNP in water was prepared via ultrasonication with a power of 495 W for two days. An appropriate amount of solution required to fabricate films of 25, 50, 75, and 100 nm thick, was diluted with 200 mL of water and filtered through an alumina Anodisc membrane with a pore size of 20 nm (Whatman). The filter membrane was subsequently dissolved in 1 M sodium hydroxide (NaOH), where the GNP film can be readily collected on a glass slide, PET substrate or glassy carbon electrode (0.2 cm^2 surface area) and washed with DI water to remove any residual ions.

4.3 Results and Discussion

Film electrode development was successful as shown in **Figure 10 (a)** where a photograph of 25, 50, 75, and 100 nm films are presented. Here, it can be seen that these films are highly homogenous over

a large surface area. This characteristic can be attributed to the small filter pore size and excellent dispersion of the GNP solution, in addition to the van der Waal attractions present among the GNP sheets. A TEM image of synthesized GNP collected from the GNP suspension prior to filtration is presented **Figure 10(b)**. The minor wrinkles apparent on the surface morphology of the sheet are a result of the buckling derived by residual epoxy groups present following the oxidization of the graphite precursor, and gives indication that the product GNP has not been completely reduced from GO to GNP. Further investigation of the surface morphology of the transparent films was done through SEM imaging, yielding an electrode film surface to be presented in Figure 1(c) for a 100 nm film. This portion of the film is representative of the film in its entirety to show the excellent contact existing between the GNP sheets provided by its characteristic two dimensional structure and high aspect ratio.

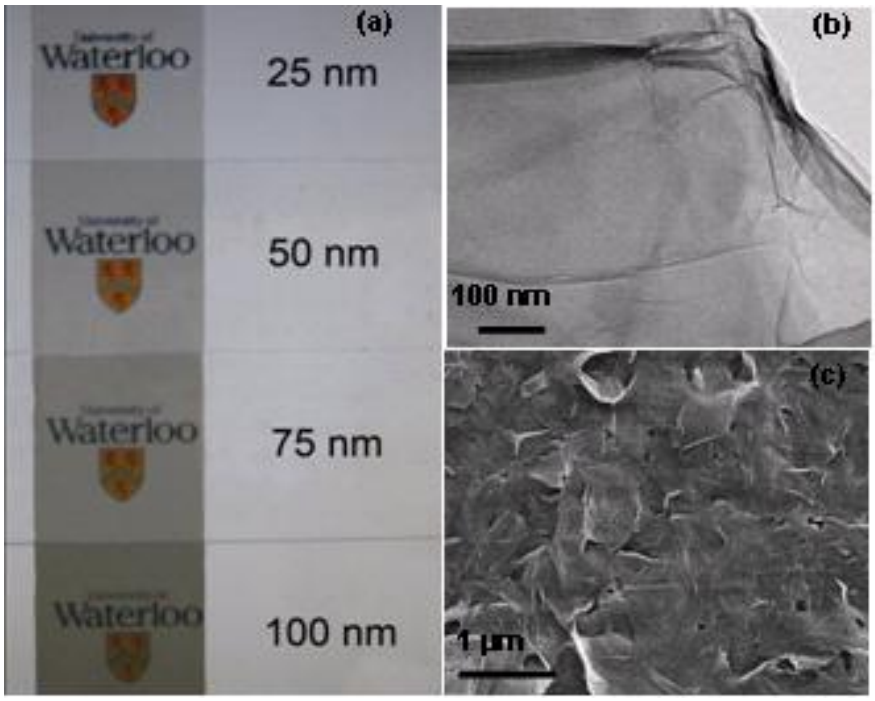

Figure 10: (a) Photographs of transparent thin-films of varying thickness on glass slides. (b) TEM image of graphene collected from dispersion before filtration. (c) SEM image of 100 nm graphene film on glass slide. Reprinted in adapted form with permission from [8], Copyright 2010 Academy of Applied Physics

The transmittance spectra were obtained through UV-vis spectroscopy technique for each of the films, with the results shown in **Figure 11**. A simple visual analysis confirms that as the film thickness increases the optical transparency of the film correspondingly decreases. Measurements at the 550 nm wavelength within the range of visible light yielded a high transmittance of approximately 70% for the 25 nm thick film. Furthermore, the absorbance of the developed films at this wavelength are verified to be in perfect accordance with the use of Beer-Lamberts law such that measured absorbance increases linearly with respective film thickness, as noted in **Figure 12**. The conductivities of the films were measured to range from between 800-1000 S/m, which is within range or higher than reported literature [106][49][48]. This factor is largely attributed to the secondary reduction cycle performed to restore the pristine structure of graphene and its corresponding electrical properties. The mechanical flexibility of these films is readily apparent through their collection onto a PET substrate demonstrated with the insert in **Figure 11**, and can be readily be bent to some degree without losing conductivity. The transparency and conductivity demonstrate by these GNP films are highly relevant to the subjects areas of electronics where flexible coatings are required, such as transparent electromagnetic shielding; anti-static or electrochromic devices; touch screen displays; organic solar cells; organic light emitting diodes to list a few.

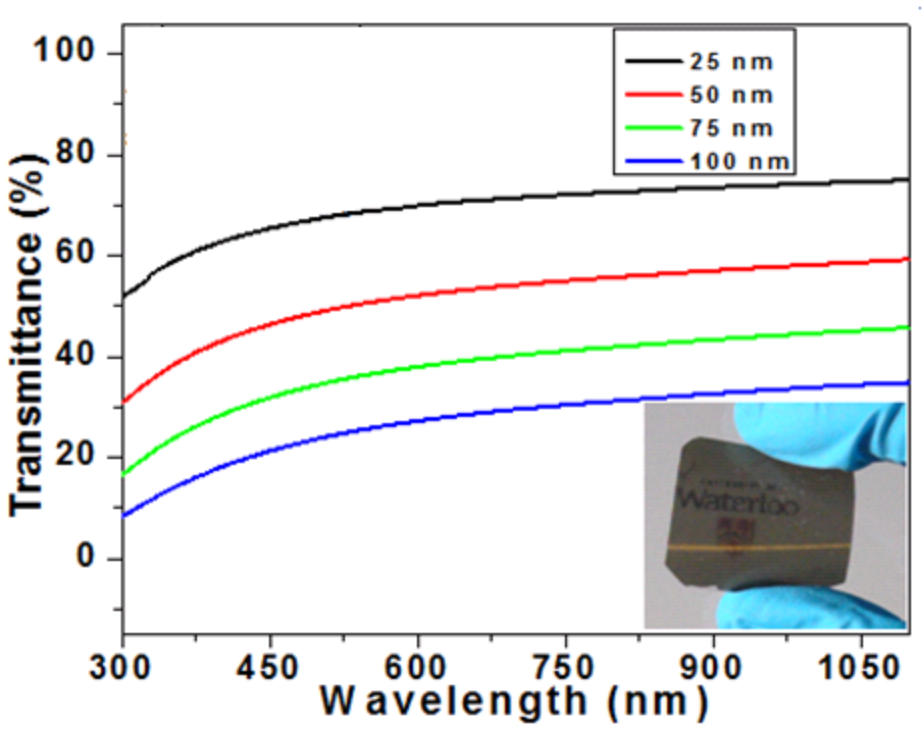

Figure 11: Transmittance spectra of thin-films of varying thickness. Top-left inset is the plot of absorbance at 550 nm versus thin-film thickness. Bottom-right inset photo shows the flexibility of GNPs film on PET substrate. Reprinted in adapted form with permission from [8], Copyright 2010 Academy of Applied Physics

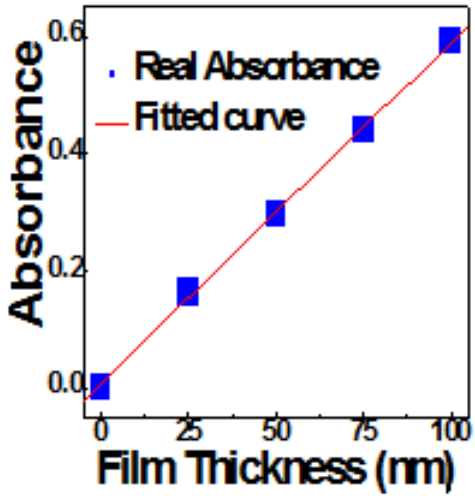

Figure 12: A plot of GNP thin film absorbance at 550 nm with respect to film thickness. Reprinted in adapted form with permission from [8], Copyright 2010 Academy of Applied Physics

The electrochemical properties of the GNP thin-films were evaluated using CV, CD and ac impedance spectroscopy (EIS) techniques. All measurements were performed using a three-electrode half-cell system in aqueous 2 M KCl solution with a Chi Instruments CHI7600D potentiostat. In terms of the operating potential, both the CV and CD techniques were conducted within a 0 - 1 V potential window vs SCE reference electrode.

The CV technique was conducted at scan rates of 10, 20, 50, 100, and 200 mV · s^{-1}, in addition to 80 nm film evaluated at higher scan rates of ranging between 0.5 to 200 mV · s^{-1}, to evaluate the electrostatic charge behavior and present resistances at low and ultra-high rates of charging. In **Figure 13(a) to (d)** the cyclic voltammograms obtained from the CV analysis of the films at low scan rates are presented. The curves of each GNP film demonstrate their close approach to ideality owing to their near perfect rectangular shapes, which is indicative of a strong electrostatic double-layer capacitance. Moreover, the high reversibility of each cycle characterizing reversible capacitive behavior is observed through the equivalent measured charge and discharge current. It is also important to note here that each film analysis observed near-identical voltammogram curves, which implies that the film thickness within this range as very little impact on the capacitive behaviour and capacitance of the material. The specific gravimetric capacitance C_p of each film based on an electrode mass m_e was calculated from the CV curves by the following equation

$$C_p = \frac{\int i \cdot dV}{\Delta V \cdot v_s \cdot m_e} \qquad \textbf{Eq. 14}$$

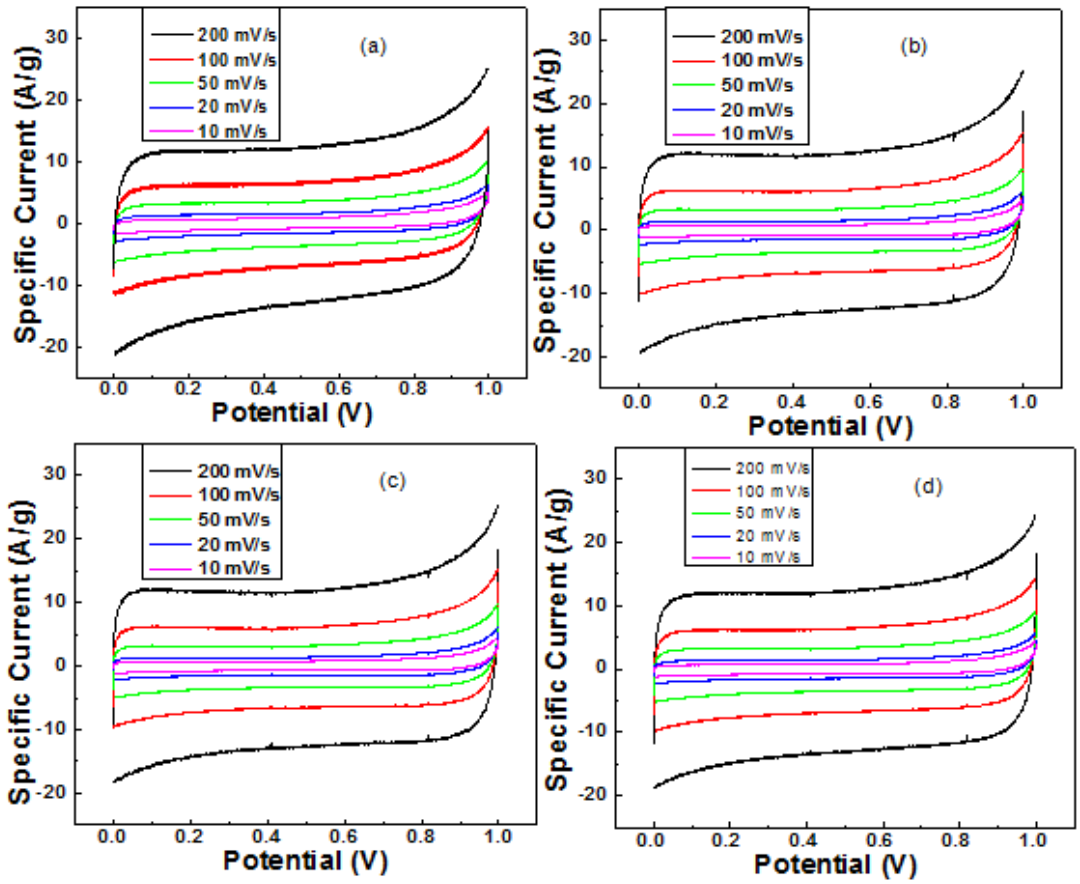

Figure 13: CV curves for (a) 25 nm, (b) 50 nm, (c) 75 nm, and (d) 100 nm thin films at scan rate of 10, 20, 50, 100, and 200 mV/s. Reprinted in adapted form with permission from [8], Copyright 2010 Academy of Applied Physics

where $\int i \cdot dV$ is the integrated area of the voltammogram and ν_s is the scan rate. At the lowest scan rate of 10 mV $\cdot$ s^{-1} a capacitance of 101 F $\cdot$ g^{-1} was obtained for a 25 nm films. The capacitance values measured at a 10 mV $\cdot$ s^{-1} for films of varying thickness are tabulated in Table 1. An increase in the C_p with decreasing film thickness is accredited to the specific surface area accessible to the electrolyte with respect to the mass of the film. Packing of the GNP to ensure the consistency of the mechanical and electrical properties through vacuum filtration and a subsequent air-drying process may have a negative effect on the electro-active surface permitted for the development of EDLC. Despite this effect, the wetted surface area of each film is readily accessible when noted that the graphene thin films retain 75-

80% of their capacitance when evaluated at a twentyfold increase to the scan rate. There appears to be negligible resistances present within a majority of the operating potential throughout each analysis to further emphasize the excellent electrical contact and low percolation threshold of the GNP films.

Table 1: Measured specific gravimetric capacitance C_p of ultra-thin GNP film electrodes from CV and CD analysis in 2 M KCl.

***10 mV · s^{-1}**

***1 A · g^{-1} in 2 M KCl**

Film Thickness (nm)	C_p (F · g^{-1})	
	CV*	CD**
100	91	100
75	93	105
50	97	117
25	101	135

Based on the excellent charge propagation demonstrated at low scan rates, an increase of the scan rate in 25 V · s^{-1} intervals evaluated for an 80 nm thick film provides a near-ideal rectangular shape that is well maintained at 100 V · s^{-1}. Further increases to the scan rate incur resistive contributions which progressively alter the charge-discharge current to yield a slimmer leaf shaped curve in Figure 14a. The high electrical conductivity of the film material is noted to be responsible for rapid charge propagation and EDLC development, emphasized by the reversible mirror current during charge and discharge at 200 V · s^{-1}. A measurement of the discharge currents of the voltammograms at increasing scan rates in Figure 14b demonstrate a noted linear dependence of the current upon the scan rate up to 100 V · s^{-1} where it then begins to deviate, as evident by the respective voltammogram shapes. These resistive elements are largely attributed to the ion mobility resistance as the rate of gain in potential becomes more rapid, allowing less active surface area to be successful at employing salt ions for capacitive charging. At high scan rates the capacitance is more reflective of charging the exposed surface layers of the GNP film, while interfaces located in deeper pores are no longer being utilized for EDLC. The gravimetric capacitance of the GNP film with increasing scan rate is shown in Figure 14c where an increase to 10 V ·

s^{-1} results in a swift decrease of 40% of the initial capacitance obtained at low scan rate. Following this initial drop, a small yet stable linear decrease in the charge current density of 0.1 A/g occurs within the range of 10 – 200 V · s^{-1}.

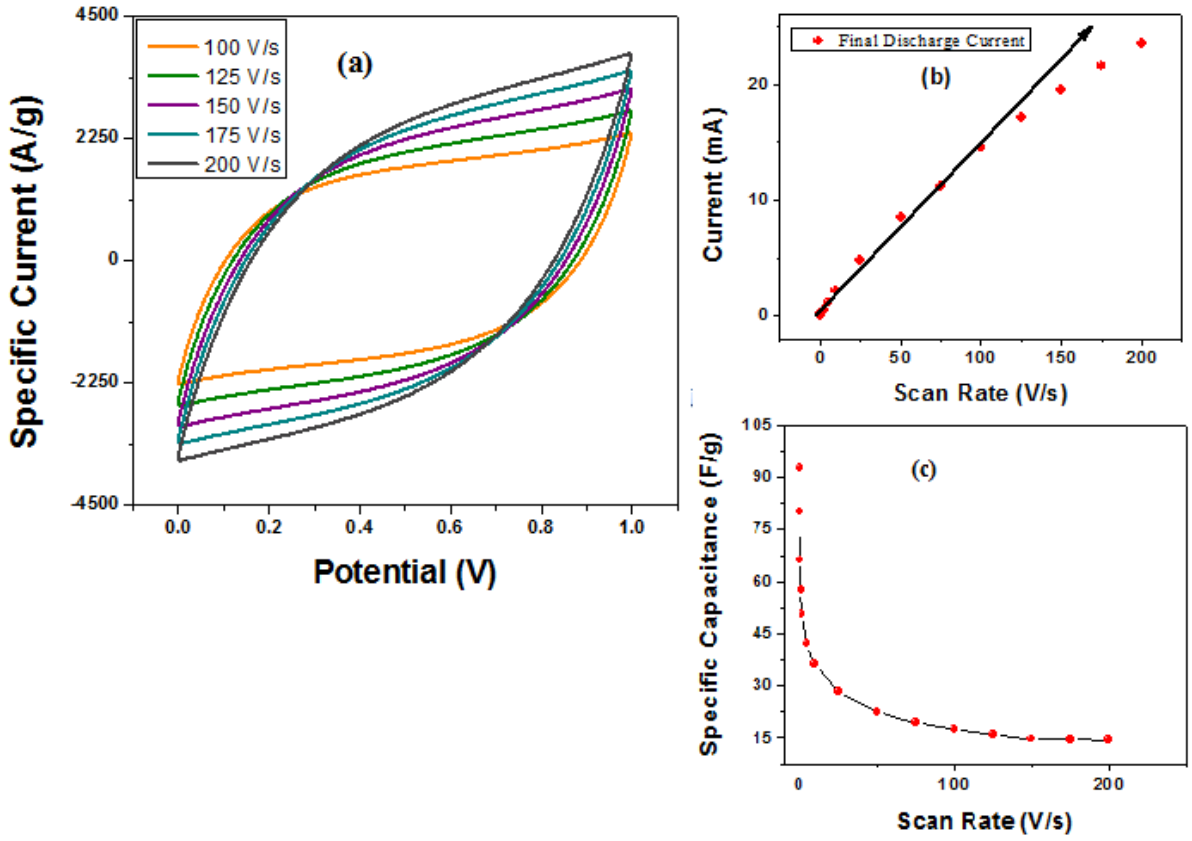

Figure 14: Cyclic voltammograms of GNP (80 nm) thin film at (a) high scan rates (100 – 200 V · s^{-1}); with corresponding (b) discharge currents and (c) specific gravimetric capacitance.

The energy density and power density are significant characterization parameters to describe the relative performance of the GNP thin-film electrodes in reference to the vast array of supercapacitor and battery materials. The energy and corresponding power densities are calculated from Eq. 11 and 13 through the use of a C_p derived from CD over a discharge time period *t*. In Figure 15 the energy densities with respect to power densities of each film are plotted in the form of a Ragone plot. The 25 nm film evidently has the best performance with a high energy density of 13 Wh · kg^{-1} at a corresponding power

density of 0.5 kW · kg^{-1} which reduces to 9 Wh · kg^{-1} at 6.5 kW · kg^{-1}. These results are in agreement with other developing carbon based supercapacitors [107] and are in the same order of magnitude as notably high results reported by Yan Wang and colleagues for graphene supercapacitors [48].

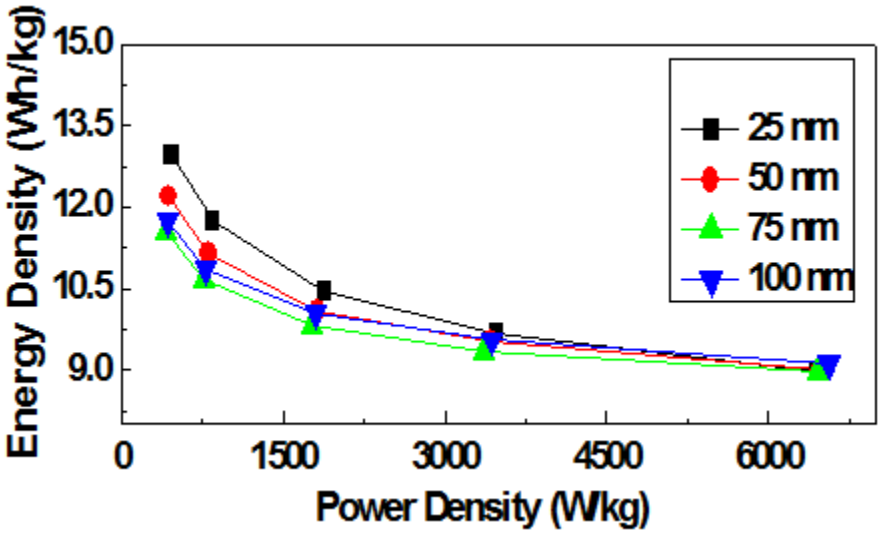

Figure 15: A Ragone plot of energy density versus power density for each GNP thin film.

The CD curves of each film were obtained at an implemented current density of 1.0 A/g and are subsequently presented in Figure 16(a-d). Analysis of the CD curves indicates a relatively ideal capacitive behavior analogous to the electrochemical behavior observed from the CV technique, where the rate of change in potential remains independent of the actual potential at which it is being measured. The specific gravimetric capacitance is calculated from the CD curves obtained through the application of Eq. 9. This technique yields a high capacitance of 135 for the 25 nm thin film, with the other film results tabulated in Table 1. Confirmation of the observed trend pertaining to film thickness and specific gravimetric capacitance is witnessed to suggest that the surface area of a thinner film remains readily accessible to electrolyte ions for improved charge transport kinetics thus giving rise to a higher capacitance per gram of active material.

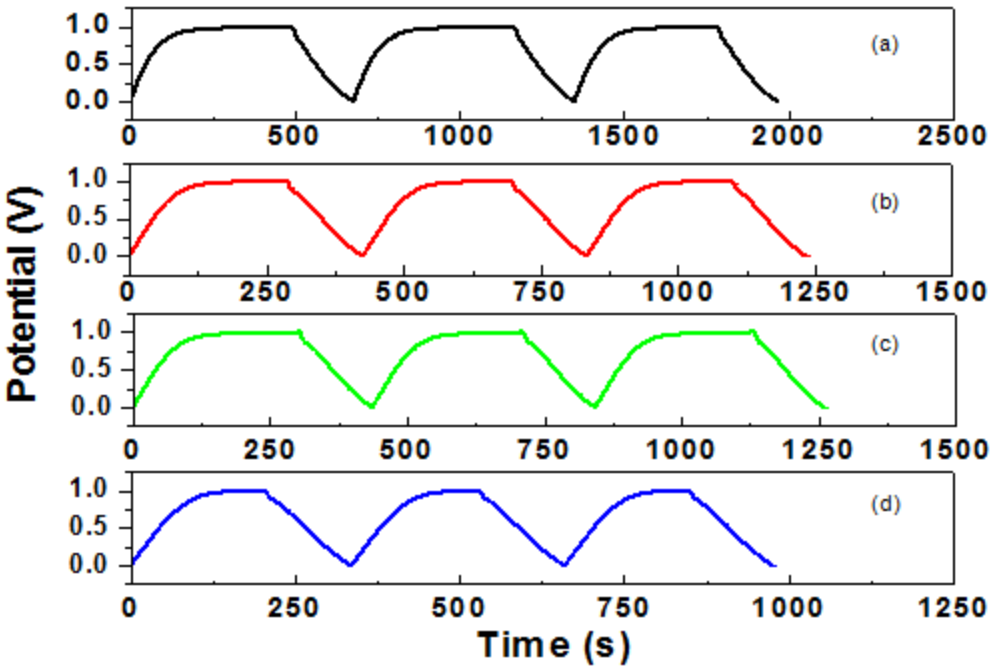

Figure 16: Charge-discharge curves for (a) 25 nm, (b) 50 nm, (c) 75 nm, and (d) 100 nm thin films at 1.0 A/g.

The EIS measurements were made within a frequency between 0.01 Hz and 10^6 Hz with an applied 10 mV bias dc voltage. A Nyquist plot of the imaginary and corresponding real impedances Z'' and Z', respectively are shown in Figure 17 for each of the thin films. In general, where the phase shift angle of the impedance approaches 90° the material performs as an ideal capacitor. Therefore, the very near-vertical impedance plots obtained for each film conclude that the graphene thin films demonstrate excellent potential for EDLC application.

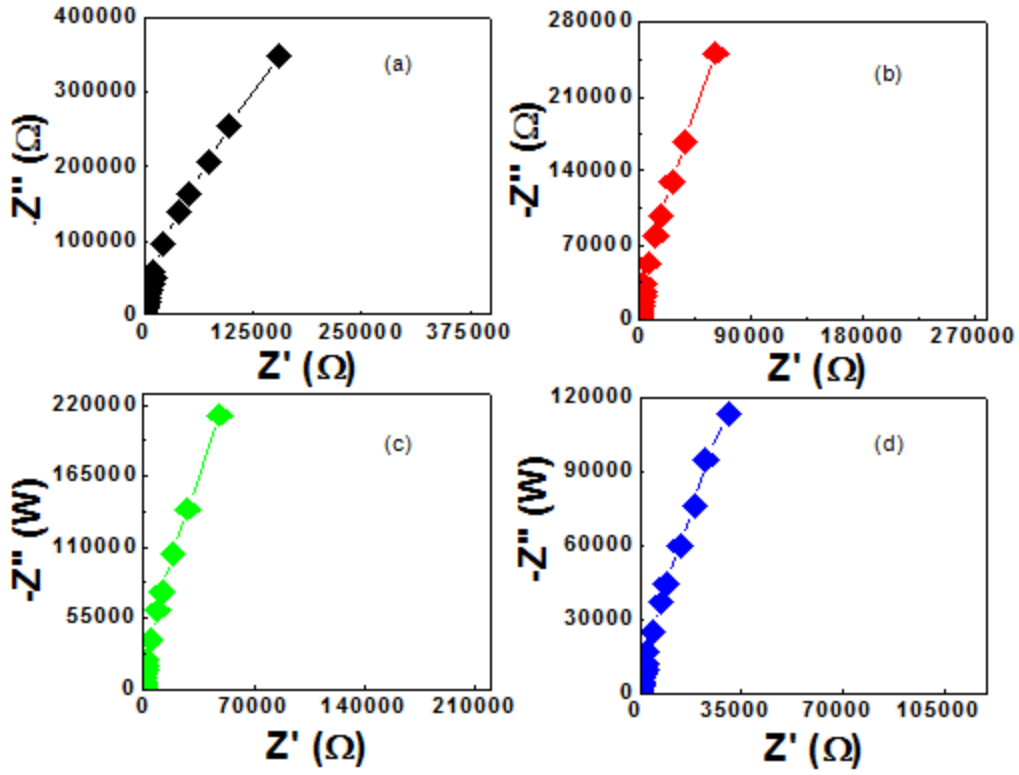

Figure 17: AC EIS curves for (a) 25 nm, (b) 50 nm, (c) 75 nm, and (d) 100 nm thin films.

4.4 Conclusions

In conclusion to this study, a simplified method for the fabrication of ultra-thin GNP films for application as an EDLC supercapacitor was presented. These films successfully demonstrate a high optical transparency with upwards of 70% transmittance of visible light measured at 550 nm for a 25 nm thick film, a homogenous surface morphology and near-ideal EDLC capacitive behavior. Through electrochemical analysis utilizing various analytical techniques a performance of 135 $F \cdot g^{-1}$ is obtained for the thinnest film ~25 nm thick. The lightweight architecture is shown to efficiently make use of the surface area of the GNP materials for electrolyte ion accessibility, with improved charge transport kinetics yielding a high energy and power density respective towards EDLC capacitor materials. It has been observed that film thickness was inversely related to the specific capacitance of the films.

Furthermore, it is anticipated that these transparent GNP films may be printed on suitable substrates for complete integration with printable and wearable electronics, which can be applied towards numerous applications.

The transparent thin films were found to undergo near-ideal EDLC charging at exceedingly fast charge rates two orders of magnitude beyond standard test rates. At scan rates above 100 $V \cdot s^{-1}$, resistive factors begin to appear which are likely related to the limitations of ions to travel through the porous structure of the film. Linearity of the discharge current deviates at this point and the developed EDLC appears to stabilize indicative that only the surface of the film is being charged. The latter conclusion is supported by a notable 83% decline of the initial C_p. Developing a means of maintaining a more accessible pore structure could be expected to improve this performance.

5.0 In-situ Preparation of Graphene/Carbon Nanotube Hybrid Transparent and Flexible Thin-Films as Electrode for Supercapacitor Application

5.1 Introduction

Carbon nanotubes (CNTs), both multi-walled (MWNTs) and single-walled (SWNTs) are electromechanically similar to GNP, possessing high electrical conductivity and superior mechanical tolerance to bending and abrasion [101]. Previous application of CNTs toward a number of transparent and flexible devices have been investigated, including organic light emitting diodes [108], organic solar cells and bolometers [109], with SWNT films having been shown to possess a sufficiently low critical thickness determined by its percolation threshold (2- 3 nm) [110], lending to its ability to yield thin-films that retain high electrical conductivity. Thus, the introduction of CNT networks to GNPs films may provide fast ionic transfer rates and minimize the resistive impact of any defects occurring on the edge or basal plane of graphene due to residual epoxy, hydroxyl and carboxyl groups remaining from preparation; ensuring the retention of high electrical conductivity [111][10]. As GNPs remain very stable as a few layers dispersed in solution, during a solvent evaporation process the surface tension facilitates the re-stacking of graphene to increasingly dense layers. With the integration of CNTs to a GNP solution a composite matrix is expected to be obtained, where the intercalation of GNPs by CNTs is anticipated to inhibit any further aggregation of platelets and form an interconnected network inside the composite. This is anticipated to improve the efficient use of effective surface area of each material utilized. The randomly interconnected network may bring a new architecture and different pore size distribution similar to that hypothesized in Figure 18, which is prominent in supercapacitor performance owing to the one dimensional structure of CNTs and the two dimensional feature of GNPs.

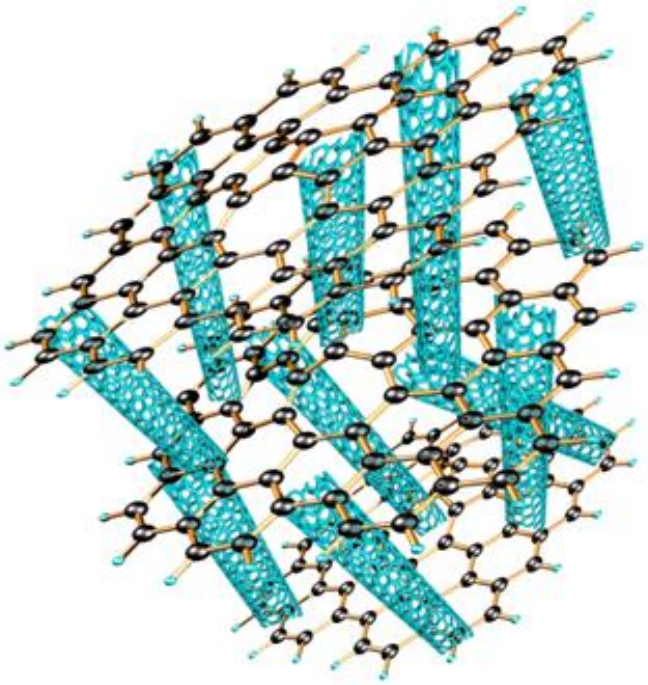

Figure 18: Schematic illustration of the graphene and carbon nanotubes hybrid new structures in the transparent and free-standing film.

The systematic study of both MWNTs and SWNTs with GNPs as hybrid structures is reported in the following as transparent thin films for application in supercapacitors. The hybrid structures were synthesized through an in-situ reduction process where a homogenous distribution of the two individual materials is obtained with few layered GNP preserved in both cases. The study presented here also investigates the transparency, electrochemical performance, and stability of both CNTs and combined GNP/CNT composites as transparent thin-film supercapacitor electrodes.

5.2 Experimental

Raw single- walled carbon nanotubes (SWNTs) were purchased from Carbon Solutions, Inc. and received HNO_3 treatment and centrifugation to remove the catalyst metal residue and amorphous carbon

[112][113]. Multi-walled carbon nanotubes (MWNTs) which have previously received HNO_3 treatment were purchased from MKNano, Canada.

Graphene oxide (GO) was synthesized by a modified Hummers method described previously. Preparation of the CNTs/GNPs hybrid was carried out during the GO reduction step. 40 mg CNTs were well dispersed with 0.2 mg mL^{-1} concentration and added to GO dispersion. The mixture was homogenized for 15 mins followed by 30 mins sonication. The molecularly mixed CNTs/GO dispersion subsequently received the same reduction process as described for GNP synthesis. Thus the CNTs function as the separator to block the self-aggregation of graphene platelets after reducing from GO, while CNTs/GNPs form homogenous network following drying and collection. The GNP/MWNT hybrid sample is denoted as G-M and GNP/SWNT hybrid is denoted G-S.

The 100 nm thick transparent thin films were prepared using a vacuum filtration method. There are 5 distinct film composites studied: GNPs, G-S, SWNTs, G-M and MWNTs. All electrochemical measurements for each of the films were performed in a three electrode cell and the measurements were carried out in a 2 M KCl aqueous electrolyte.

The SEM imaging was done using a LEO1530 FE-SEM equipped with EDAX Pegasus 1200 integrated EDX/OIM. The electrochemical properties of the transparent thin-films were evaluated using CV, CD and EIS techniques. The electrochemical measurements were performed using a Chi Instrument (CHI7600D) where the CV and CD techniques were conducted within a 0 - 1 V vs SCE potential window; the former at scan rates of 10, 20, 50, 100, and 200 mV/s and the latter with a constant charge density of 1 A/g. The EIS was measured over a frequency range of 10^6 Hz to 10^{-2} Hz, with a sinusoidal signal at bias DC voltages between 0.1 V – 0.01 V.

5.3 Results and Discussion

The transmittance spectra of each film is shown in Figure 19 which demonstrates that the SWNT and G-S hybrid films are significantly more transparent than that of GNPs, MWNTs and G-M. This is in

agreement with Park et al. pertaining to single and multi-walled CNT transparency [114]. The transmittance of GNPs falls directly between the two classes of CNTs within the region of visible light. One possible reason could be the varying size of the carbon nanomaterials considering they all possess π-plasmon of carbonaceous materials [110]. The SWNTs produced from arc-discharge technique have the uniform diameter of 1.4 nm and bundle size of 3-6 nm in width and 0.5-2 μm in length, while the MWNTs produced from CVD technique have a diameter of around 15-20 nm in width and 0.5-3 μm in length. Distinct GNP has an approximately 200-500 nm diameter and a 2-4 nm thickness. The SWNT and G-S spectrum maintain the second pair of singularities in the density of states (DOS) of semiconducting SWNTs (S_{22}) occurring at wavelengths around 1000 nm and M_{11} metal-conducting band-gap at around 720 nm [115]. Corresponding to the metallic and semi-metallic nature of MWNTs and GNPs respectively, neither displays any feature equivalent to that exhibited by SWNTs. Evaluation of each material's transmittance at 550 nm is tabulated in Table 2. Optical transparencies of the composite films were found to be 37%, 32%, 27%, 19% and 14% for SWNTs, G-S, GNPs, G-M and MWNTs, respectively, corresponding to 100 nm thick films. Adding GNPs to SWNTs slightly decreased the transmittance of the SWNT film, while adding GNPs to MWNTs worked in a converse manner. As indicated in the previous study, to achieve higher transparency the film thickness must be reduced. The right-bottom inset photo in Figure 19 demonstrates the optical transparency of the 100 nm thick G-S hybrid material film with the University of Waterloo logo underneath.

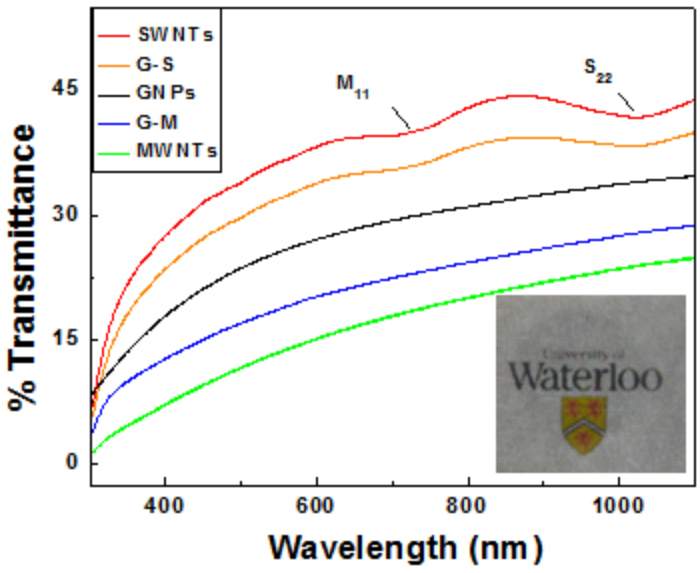

Figure 19: Transmittance spectra of 100 nm thick thin-films of SWNTs, G-S hybrid, GNPs, G-M hybrid and MWNTs. Bottom-right inset is a photograp of the 100 nm thick G-S hybrid film on glass slides, a logo underneath of it showing the transparency of the film.

Table 2: The absorbance at 550 nm from UV-spectroscopy for SWNTs, G-S hybrid, GNPs, G-M hybrid and MWNTs.

Capacitor Material	Transmittance (550 nm)
SWNTs	36.3
G-S	32
GNPs	25.5
G-M	18.62
MWNTs	13.53

The surface morphologies of the G-S and G-M composite thin-films were investigated by scanning electron microscopy (SEM) at both low and high magnification, and displayed in Figure 20. A loose network of MWNTs is observed to be well dispersed among the GNP matrix, both along the surface and between the individual sheets to form larger pores. Contrasting to this, smaller pores observed for G-S are primarily attributed to the smaller diameter and bundle size of the SWNTs. These images are in

agreement with the transmittance spectra analysis in Figure 19, which demonstrates that MWNTs have a larger volume than SWNTs and thus yield less transparency to the corresponding film. Both of these hybrid networks and newly formed pore structures may contain a distribution of micropore, mesopore and macropore which are expected to permit additional access of the electrolyte to the active surface of the hybrid material. Research groups investigating pore size relative to capacitance claim an optimal pore size of 0.7 nm yields a maxima EDLC when using an aqueous electrolyte, and a notable increase in capacitance with materials having a significant micropore population [116][89]. Thus, relative pore size and distribution are expected to have an impact on the capacitance attainable by CNT/GNP hybrid composite films.

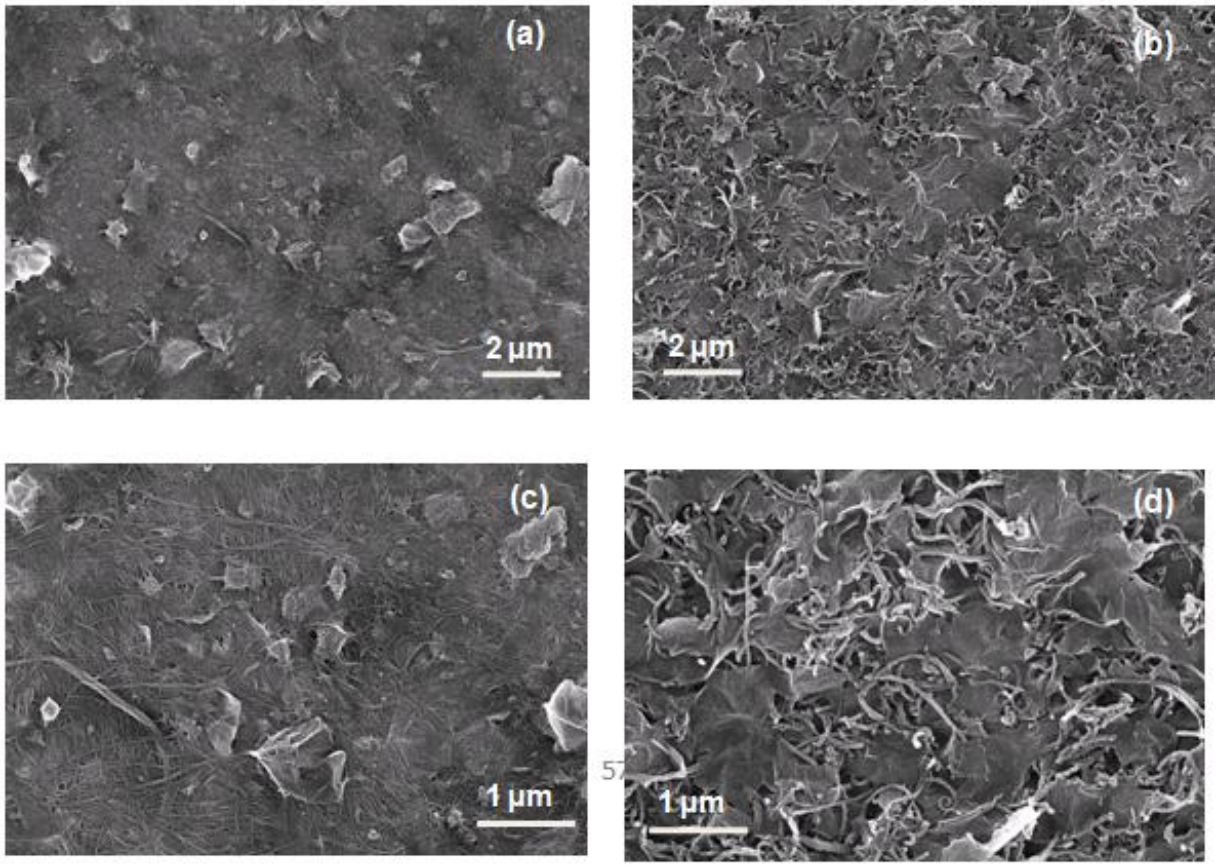

Figure 20: SEM images of (a)G-S and (b)G-M at low magnification; and (c) G-S and (d) G-M at high magnification.

The electrochemical CV technique was used to evaluate the EDLC of each thin-film, with increasing charge rates applied to characterize the charge/discharge kinetic behavior of the composites and power capability. In Figure 21 the CV curves of GNPs, G-M, and MWNT, show the approach to ideal EDLC of each material from their semi-rectangular shape maintained through all the scan rates. The rapid responses upon reversal of the potential, in addition to the relatively constant current, are representative of both a fast diffusion within the materials and small ESR. Figure 21(a, b) of SWNT and G-S materials display a slight distortion near 0 V (vs the SCE reference) which is attributed to a pseudocapacitive redox reaction, most likely exhibiting a redox coupling of the following:

$$SWNT - \mathrm{C\text{-}O}H \leftrightarrow SWNT - \mathrm{C{=}O} + H^+ + e^-$$

$$SWNT - \mathrm{COO}H \leftrightarrow SWNT - \mathrm{COO} + H^+ + e^-$$

These oxygen functional groups are likely present from initial purification procedures, and the results are in agreement with literature findings [117][118]. This substantiates that the SWNTs are more chemical active than MWNTs corresponding to a higher concentration of –OH and –COOH functional groups on the surface and ends, both of which contribute to the redox reaction. The distortions approaching the 1 V limit are possibly due to water decomposition, with all materials exhibiting this behavior as the scan rates increase [81]. The specific capacitance of each developed film was evaluated according to Eq. 7 to yield a C_p of 24.95, 44.11, and 86.14 $F \cdot g^{-1}$ for MWNTs, G-M, and GNPs, respectively at a scan rate of 10 $mV \cdot s^{-1}$. The SWNTs and G-S composite at the same scan rates obtain a capacitance of 43.95 and 83.28 $F \cdot g^{-1}$, respectively. The capacitance value of G-S was not shown to decrease relative to the mass of SWNT incorporated, possibly owing to the additional surface area provided through the formation of micropores, presenting an equal mass ratio CNT/GNP composite electrode successful in achieving a high specific capacitance than either pure specimen.

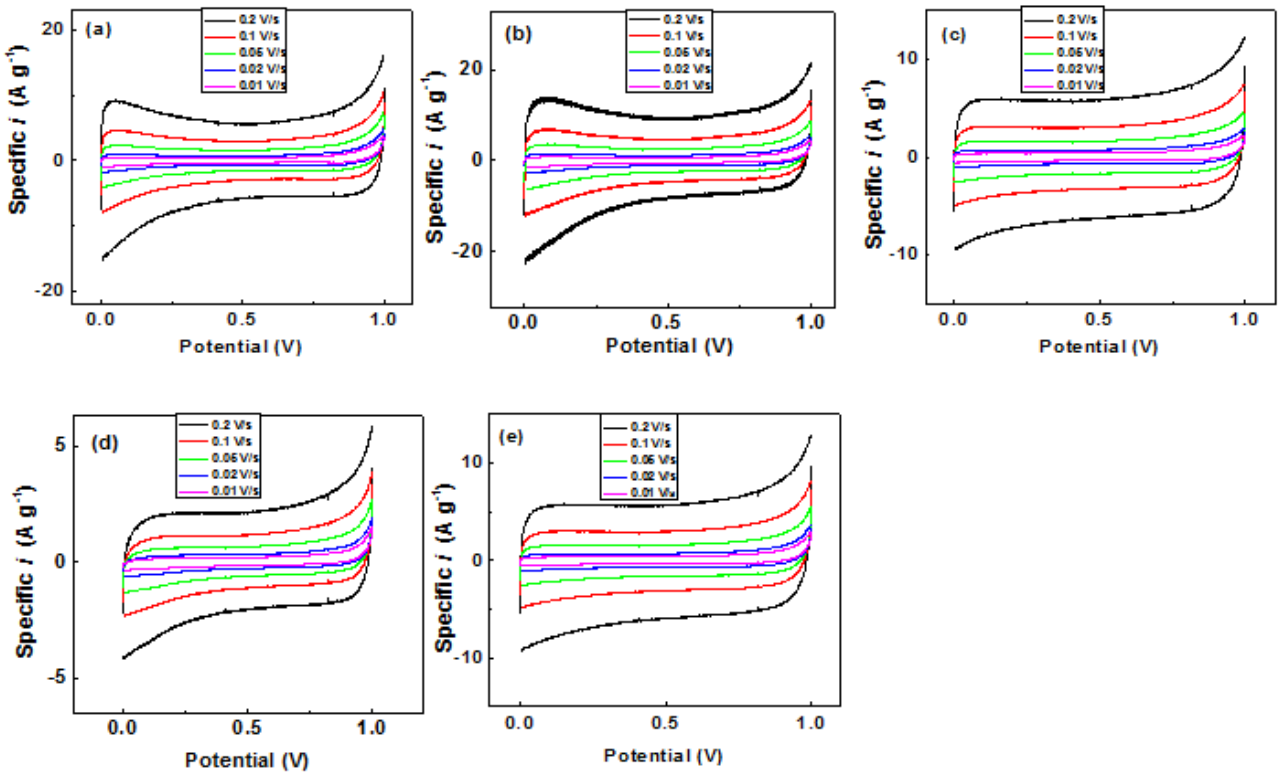

Figure 21: CV curves of (a) SWNTs, (b) G-S, (c) GNPs, (d) MWNTs and (e) G-M in 2 M KCl at scan rates of 10, 20, 50, 100 and 200 mV · s^{-1}.

Charge/discharge behavior of each capacitor at a constant current density was evaluated by chronopotentiometry technique as shown in Figure 22. The linearity of the charge curves of each material emphasize that electric double-layer charging capacitance is developed. At small current densities each material shows an alternative reaction mechanism is competing with the charge current within the range of 0.9 to 1 V consistent with a shift in EDLC charging for CV analysis. This behavior is attributed to a competing faradaic oxygen evolution reaction responsible for dividing the applied current [18]. The slower charge rate appears more significantly in the GNP film and remains present in both GNP/CNT composites where upon reversal a slump corresponding to a faster drop of the initial discharge potential. This indicates a smaller useful discharge current is likely owing to a separate charge transfer mechanism [119] and lower coulombic efficiency. In Figure 22(a) a change in the charge/discharge behavior of

SWNT and G-S near 0 V vs SCE is in accordance to previously noted redox behavior. The specific capacitances of each thin-film were evaluated using the discharge slope of the CD curve according to the Eq. 9. Inflection points present within the linear discharge curves are a result of charging inefficiency or pseudocapacitive behavior, therefore linear segments of the slope for all capacitance measurements were taken within the potential range of 0.6 – 0.3 V. The specific capacitances of MWNTs, G-M and GNPs are 28.6, 50.37 and 70 $F \cdot g^{-1}$, respectively at a current density 0.5 $A \cdot g^{-1}$ yielding a slight decrease in the specific capacitance relative to MWNT mass as observed from CV analysis. The G-S composite retains a high capacitance value from discharge evaluation of 79.6 $F \cdot g^{-1}$ yielding a composite material with higher capacitance than either SWNTs (48.5 $F \cdot g^{-1}$) or GNPs (70 $F \cdot g^{-1}$) individually, which may be contributed from the additional new pore structure formed inside the hybrid materials.

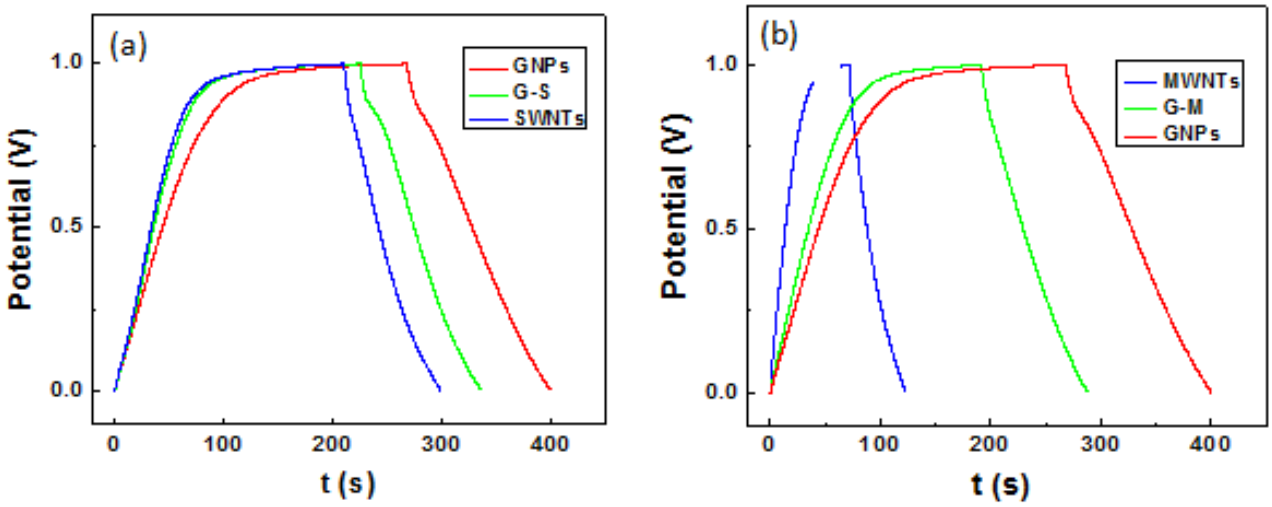

Figure 22: CD curves of (a) SWNT, GNP and composite G-S, and (b) MWNT, GNP and composite G-M at a current density of 0.5 $A \cdot g^{-1}$ in 2 M KCl.

Nyquist plots in Figure 23 (inserts at high frequencies) developed from EIS were used to evaluate the equivalent series resistance (ESR) (includes bulk electrolyte, working electrode and current collector resistances), and the ion transport resistance attributed to the materials porous structure. In the low frequency region porous materials become saturated and can achieve a capacitance that approaches ideal behavior. Resistance within an ideal capacitor for low frequency ac is strictly owing to its capacitive

reactance or imaginary impedance, therefore leading to the overall impedance being perpendicular to the real impedance axis. All materials tested are thus shown to exhibit an approach to ideal capacitive behavior at low frequencies by their respective phase angles that near 90°. Deviations from a purely vertical impedance plot at low frequencies can been observed, and are often owing to the constant phase element (CPE) to describe surface roughness and irregularities in pore distribution/active surface charging [92]. The G-M and G-S composites yield a greater phase angle relative to MWNT and SWNT, respectively within the low frequency domain indicating the addition of GNP provides the electrolyte better access to surfaces of the composite for EDL charging, with a minimal difference in slope at low frequencies between the composite and GNP. Inserts within Figure 23 highlight the intercept of each curve at the axis of real impedance (Z'), representing the ESR parameter of the configured cell. The benefits of reducing the ESR relate to an improvement in power density and energy efficiency of the respective material [48]. An evaluation of ESR values pertaining to MWNT, SWNT and their respective GNP composites can be found in Table 3. A decrease in ESR relative to the pure GNPs is obtained in both G-M and G-S composites, and likely owing to the structure of the composite material. From SEM imaging (Figure 20), in-situ production of the hybrid electrode yields an increasing number of interconnected, electrically conducting pathways between each nanoparticle through the abundant CNTs and high surface area of graphene plates throughout the integrated network, likely improving the overall electrical conductivity.

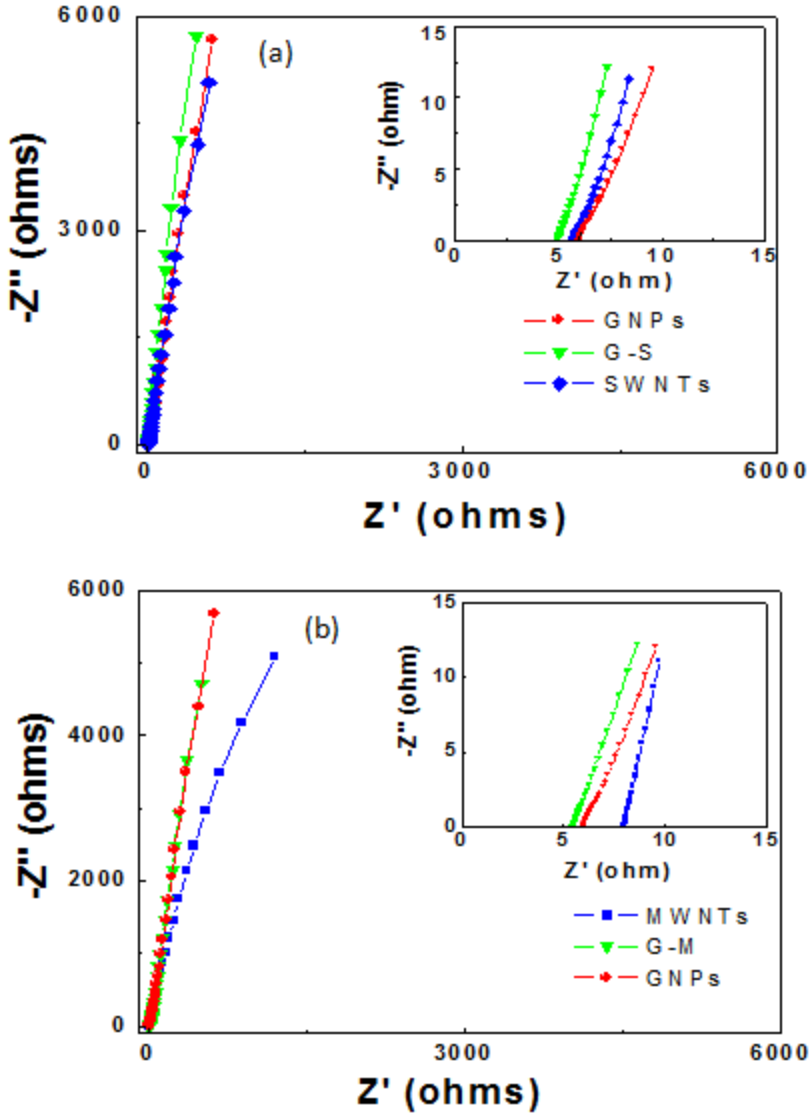

Figure 23 Nyquist plots of (a) MWNT, (b) MWG, (c) GNP, (d) SWNT and (e) SWG at 0.1 V. Top right inset shows high frequency region of ESR.

Table 3: The absorbance at 550 nm from UV-spectroscopy for SWNTs, G-S hybrid, GNPs, G-M hybrid and MWNTs.

Capacitor Material	ESR (ohm)
SWNTs	4.95
G-S	5.5
GNPs	5.6
G-M	5.2
MWNTs	5.8

Thin-film capacitors which maintain a high energy density when operating at a high power density are highly desirable, thus the energy density of each material was evaluated using Eq. 11. A Ragone plot (Figure 24) illustrates consistent trends in the power density achieved relative to the materials energy density. Maximum energy densities obtained for CNT/GNP composites were 12.85 and 5.10 Wh · kg^{-1} for G-M and G-S, respectively. The power densities were evaluated using the Eq. 12, where maximum power densities were obtained to be 2774 and 6447 W · kg^{-1} for G-M and G-S, respectively, showing a competitive performance relative to other thin-film capacitors. This value can likely be increased upon further investigation to reduce the ESR through an optimal combination of the electrode, electrolyte and assembly.

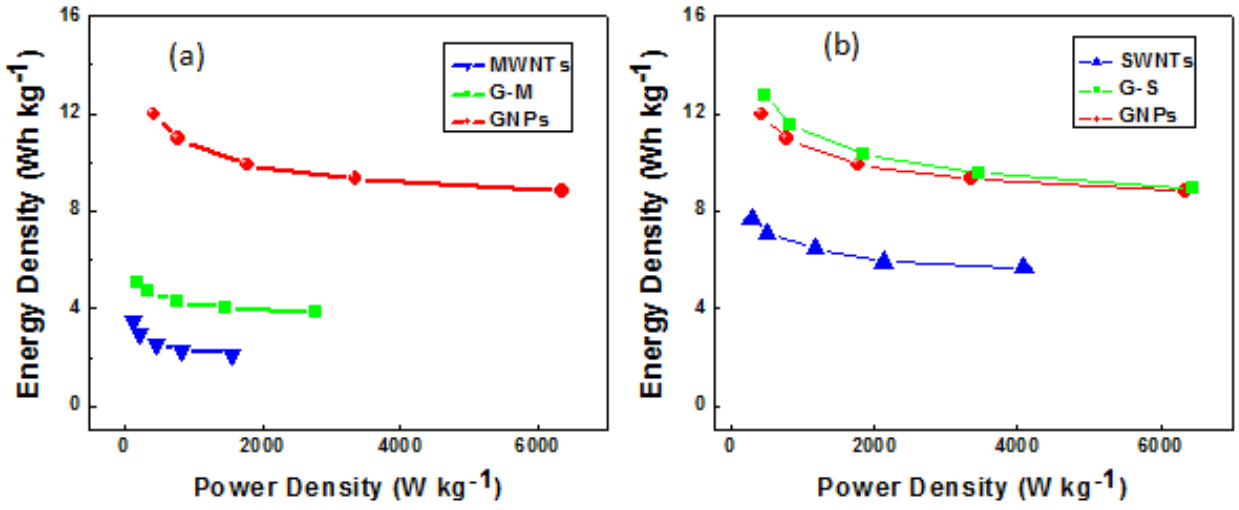

65

Figure 24: Ragone plot of GNP and a) MWNT and b) SWNT composite film performance.

The overall results of relative capacitance and energy/power density were summarized in Table 4. Adding GNP material to CNTs has significantly improved the performance of CNTs. For SWNT/GNP composite G-S sample, the results are even better than GNPs considering transmittance, electrical series resistance, capacitance based on CD analysis and energy/power densities. This is in agreement with the SEM observation of the fine pore structures formed inside the hybrid materials. Adding MWNTs to GNPs does not show pronounced enhancement to the performance to GNPs, probably due to the large tube diameter which prevent the formation of the optimized pore structure accessible the ions.

Table 4 The capacitance calculated from cyclic coltammetry (CV), chronopotentiometry (CD), and the electrical series resistance (ESR) from EIS, maximum energy density and maximum power density for SWNTs, G-S hybrid, GNPs, G-M hybrid and MWNTs.

Capacitor Material	CV Capacitance ($F \cdot g^{-1}$)	CD Capacitance ($F \cdot g^{-1}$)	ESR (ohm)	E_{max} $Wh \cdot kg^{-1}$	P_{max} $W \cdot kg^{-1}$
SWNTs	43.95	48.50	4.95	7.80	4096
G-S	83.28	79.60	5.3	12.85	6445
GNPs	86.14	70.00	5.7	11.97	6341
G-M	44.11	50.34	5.2	5.10	2774
MWNTs	24.95	28.60	5.8	3.50	1562

Stability testing was performed at a higher current density of 2 $A \cdot g^{-1}$ for 800 cycles to evaluate capacitance performance after extended use. In Figure 25 the CNTs, GNPs and composite films all measure to have good stability, retaining a specific capacitance ≥ 89%. The GNPs and SWNTs films in Figure 25b appear to have slightly better stability in comparison to MWNTs performance (Figure 25a),

while the stability of G-M composite improves with the addition of GNP. No discernable difference is noted in the G-S film when compared to both SWNTs and GNPs over the 800 cycles evaluated. Further cycles of SNWTs may lead to some extent loss in stability as a result oxygen functionalities present on the SWNT surface undergoing partially irreversible redox reactions.

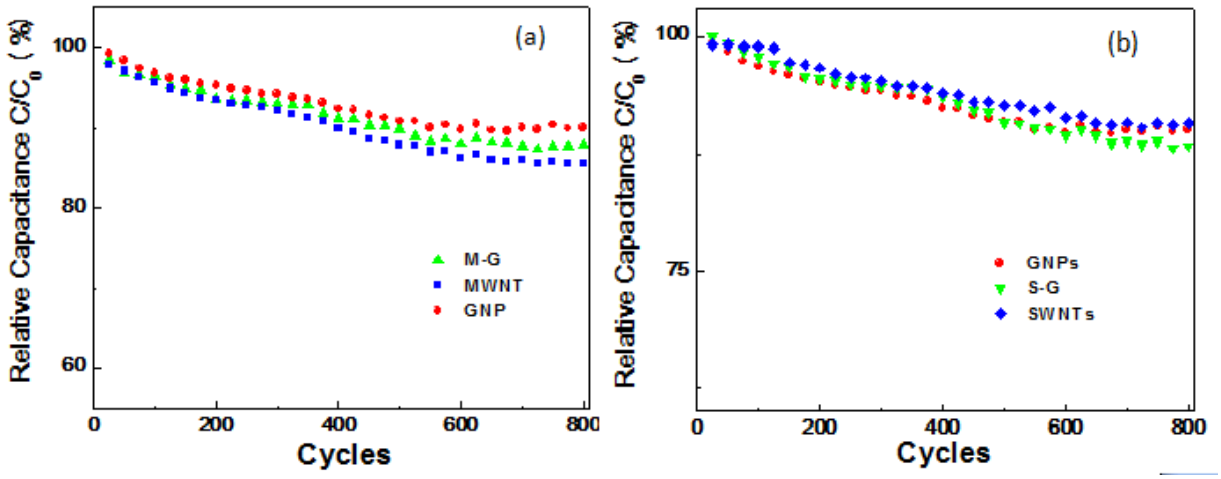

Figure 25: Capacitance retention for 800 cycles at 2 · A g^{-1} current density for GNP with respect to a) MWNT and G-M, and b) SWNT and G-S.

5.4 Conclusion

In conclusion, a systematic study on both MWNTs and SWNTs with GNPs was performed with the fabrication of transparent thin films for supercapacitor application. The hybrid G-S and G-M materials were synthesized via an in-situ reduction process, yielding homogenously distributed composite with a few layer graphene structure preserved. Transmittance of 100 nm thick materials at 550 nm evidently revealed the GNPs film to have an optical transmittance directly between SWNTs and MWNTs films, with equivalent weight CNT/GNP composites possessing an average transmittance of their respective materials. Thus, SWNTs assisted in decreasing the transmittance of GNPs, which is significant for this type of application. Further improving the transmittance can be achieved by decreasing the film thickness, which can be as thin as 25 nm based on previous findings. Evaluation of the charge dynamics and specific capacitance was performed through CV and CD to yield a mean performance from MWNT/GNP

composites relative to MWNT and GNP, while substantiating an improvement of overall performance made by the integration of SWNT and GNP to form a G-S composite. This improvement was thought to be the match of the diameter of SWNT bundles (4-5 nm) and GNP thickness (2-4 nm), which leads to an improved uniform pore structures among the transparent films.

6.0 Graphene-based supercapacitors electrodes with Pulse-Electropolymerization of Polypyrrole

6.1 Introduction

A variety of electrode synthesis methods have been employed to create conductive polymer-carbon nanostructure heterostructures, including one-pot copolymerization, and electrodeposition on pre-fabricated CNT membranes. It is anticipated that these new heterostructures can bring the EDLC and pseudocapacitive behaviour together, leading to a significantly enhanced performance and stability [36][120][121]. However, co-polymerization with GNP or CNT suspensions suffers from polymeric aggregation and high electrode resistances due to poor interconnection between conducting structures, while post-fabrication electrodeposition often blocks electrolyte channels at the outer surface and does not form a conformal coating of polymer [122][123]. Much attention has been given to the pulse electrodeposition techniques owing to their promising results shown recently by several groups [124][123]. In a recent study, pulsed electrodeposition has been employed using well-separated short potential pulses which allows pyrrole (Py) monomers to diffuse into the carbon EDLC material pore space between polymerization pulses, and demonstrated a significant improvement in the uniformity of polypyrrole (PPy) coatings on CNTS [123]. A schematic illustration showing how rest periods may allow for Py molecules to diffuse into the pore space of the G between deposition pulses is shown in Figure 26. This leads to a more uniform coating and less blocked pores than obtained with a continuous deposition method. Some groups have also proposed that during rest periods polypyrrole chains stabilize, making nucleation of new chains more favorable during subsequent polymerization pulses rather than enlarging previous chains [124][80]. Short deposition pulses have also been shown to produce fewer defects in the structure of the resulting polypyrrole chains. In Figure 26 a schematic shows the pulsed electrodeposition process.

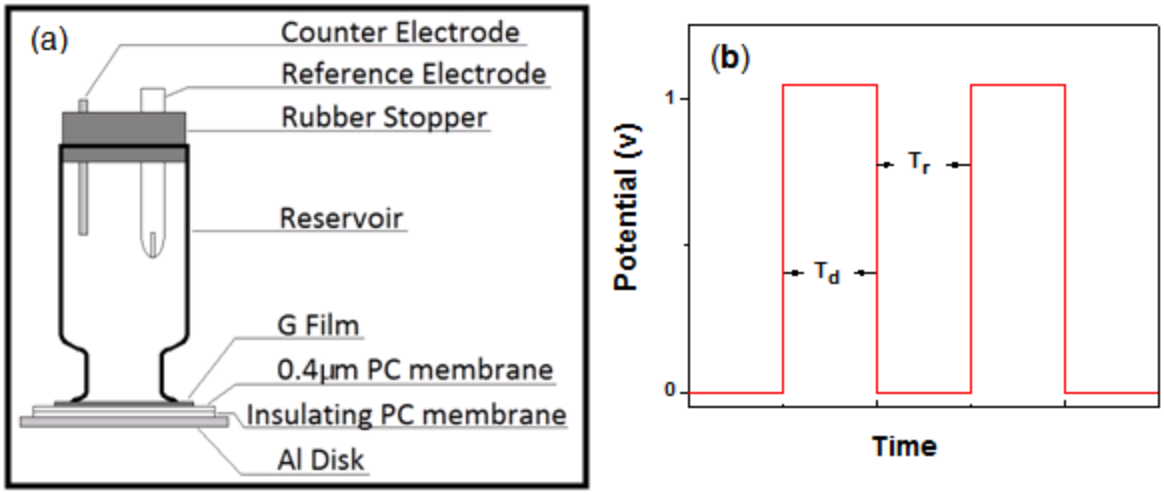

Figure 26: (a) Diagram of the apparatus used to deposit PPY on GNPs and electrochemical testing, where the clamp and rubber O-ring are not shown; (b) Electrodeposition potential waveform used in deposition experiments, with deposition pulse length T_d and rest pulse length T_r. Reprinted in adapted form with permission from [9], Copyright 2010 Journal of Physical Chemistry C

In this study, GNP/polypyrrole composites were created using a modified pulsed electrodeposition technique with differing total deposition times, in an effort to optimize the electrodeposition time of Py for synergistic capacitive ability. The primary objective of this study is to prepare optimized homogeneous GNP/polypyrrole composite films that give reasonably high performance for flexible supercapacitors application.

6.2 Experimental

GNP films were prepared on an insulating polycarbonate membrane support. To prepare these samples, as-prepared GNP was sonicated with a concentration of 0.05 mg · ml^{-1} for one hour. The dispersion was then vacuum filtered through a polycarbonate (PC) membrane (25 mm diameter, 0.4 μm pores) to create a uniform GNP film.

The resulting GNP film on PC support membrane remained flexible and robust to washings. Without removal from the PC membrane, the film was placed on a supporting aluminum disk of the apparatus shown in Figure 26(a). A rubber gasket and glass electrolyte reservoir were clamped to the film

over a representative and uniform region. Following, a 1 M KCl containing 50 mM pyrrole monomer solution was used to fill the reservoir and a rubber stopper was affixed to its top. A three-electrode setup consisting of a Pt counter and SCE reference electrode was placed in solution through the rubber stopper, where the graphene film was then wired as a working electrode.

A CHI 760D Electrochemical Workstation was used to pulse the potential from 0 V to 1.05 V for 0.1 s each until a total deposition time at 1.05 V was obtained in order to deposit PPy onto the GNP film. In order to determine the optimal PPy electrodeposition time, electrodes and films were prepared with several total electrodeposition times ranging from 60 to 360 s using 60 s intervals, and are denoted G/PPy 60, G/PPy 120, G/PPy 180, G/PPy 240, G/PPy 300 and G/PPy 360 respectively, with the pure G electrode being denoted simply G. The results are focused on the G/PPy 60, G/PPy 120, G/PPy 360 samples to demonstrate the concept and performances.

Electrochemical characterization was carried out using the same parameters as above and followed by draining of deposition solution from the reservoir and rinsing of the resulting composite film with deionized water. After drying at 50◦C under vacuum the G/PPy membrane with a diameter of 25 mm is ready for use as an electrode without any further treatment. Techniques including CV, CD and EIS were all carried out following a 25-cycle CV activation between -0.4 and 0.6 V vs. SCE at a scan rate of 100 $mV \cdot s^{-1}$. Subsequent CV and CD technique was also carried out between -0.4 and 0.6 V vs. SCE, at scan rates ranging between 10 and 200 $mV \cdot s^{-1}$; and at current densities between 1 and 4 $A \cdot g^{-1}$, respectively. The EIS was carried out between a frequency range of 1 MHz and 10 mHz under an open circuit potential with ac signal amplitudes between 10 and 100 mV.

TGA was performed on a Q500 Thermogravimetric Analyzer (TA Instruments, USA) in a nitrogen atmosphere between 50 and 800°C at a heating rate of 10°C/min. TGA analysis of samples involved drying the sample at 60°C for 72h prior to testing. SEM images were obtained using a LEO 1550 FESEM (LEO Electron Microscopy Inc., USA)

6.3 Results and Discussion

The waveform of the shape shown in Figure 26(b) was applied to the GNP film in an electropolymerization solution containing 1M KCl electrolyte and 50mM pyrrole. The "on" potential was held at 1.05 V vs. SCE for electropolymerization of pyrrole monomer, and lowered to open circuit potential during the "off" resting cycles. These waveforms are repeated until a total deposition time T_d has been reached. Figure 27(a) and (b) show a graphene film supported on a PC membrane with a diameter of 25 mm before and after 120s electrodeposition of PPy. Both films are homogeneous and show good flexibility, which indicates that deposition pulses do not inhibit the flexibility of pure GNP. This also suggests that the feasible construction of flexible supercapacitors was able to take advantage of both EDLC and pseudocapacitance, which providing an excellent method to meet the increasing demands for high energy density supercapacitors [125][126].

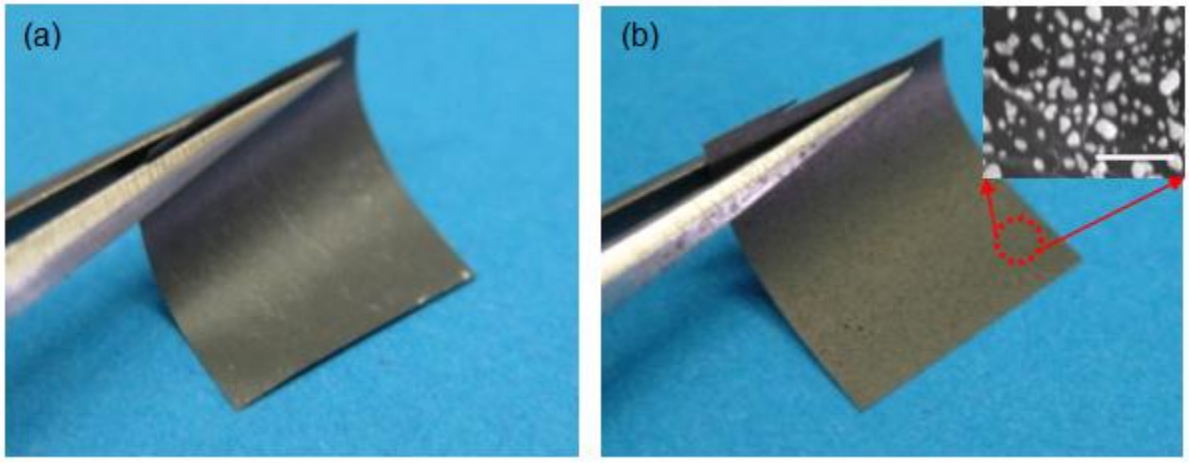

Figure 27: Photographs showing the flexibility of the (a) pure GNPs and (b) G/PPy 120s films, the in-set is the SEM image at the observation area with the white bar is 100 nm. Reprinted in adapted form with permission from [9], Copyright 2010 Journal of Physical Chemistry C

Figure 28 illustrate the whole pulse electropolymerization process compared with the continuous electropolymerization under the waveform shown in Figure 26(b). During the deposition pulse, the

pyrrole monomers in the immediate vicinity of the graphene films are electropolymerized and precipitated as polypyrrole nanoparticles on the graphene surface. During continuous deposition, all pyrrole monomers suspended in the porous structure of the graphene film are consumed, leading to significantly reduced electropolymerization of monomer within the graphene. All remaining deposition current instead is consumed by electropolymerization at the film surface, where pyrrole monomer concentration is continually restored by diffusion from the bulk solution. This appearance of larger sized polymer nanoparticles is further enhanced by the likelihood for electropolymerization to continue on any given polymer chain rather than nucleate the growth of a new chain. This results in very rare nucleation of new chains on the graphene surface, which tends to enlarge present polymer particles rather than increase particle density and surface coverage. The combined effect results large and continuous polypyrrole particles on the graphene surface (shown in continuous electropolymerization), but with very little penetration into the porous network of graphene sheets. This also reduces the surface area of the composite electrode capable of performing the fast faradaic redox reactions which provide the additional contribution of pseudocapacitance to the device. As reported elsewhere [126], increasing the resting time T_r between short deposition pulses allows pyrrole monomers to diffuse from the bulk solution into the intercalating spaces between graphene sheets and to be electropolymerized during the following deposition pulse. The addition of these resting periods results in uniform deposition of small polypyrrole nanoparticles throughout the porous graphene film as shown in Figure 3 and maximizes the exposed polypyrrole surface area on the graphene sheets. The resting time further serves to allow relaxation of polymer chains grown during a previous deposition pulse. This relaxation allows polymer nanoparticles to be grown entirely in one pulse, and then to relax to a lower energy state during the resting time and not to grow during subsequent pulses[42,45]. This result is likely to further improve the PPy coverage on the graphene electrode and increase the pseudocapacitive contribution to the specific capacitance of the composite films.

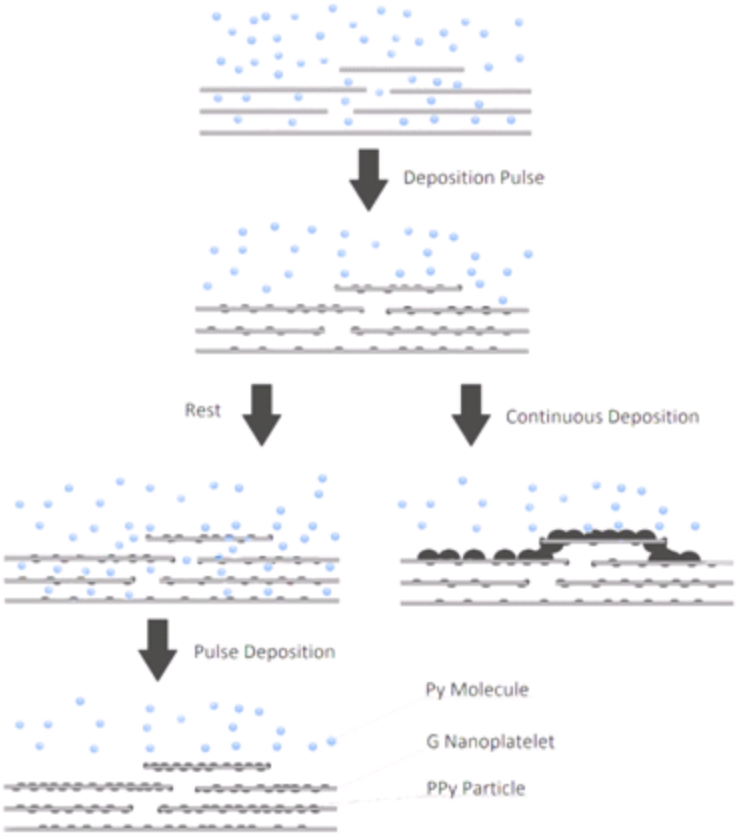

Figure 28: Schematic diagram illustrating how rest periods allow for Py molecules to diffuse into the pore space of the G between deposition pulses. This leads to a more uniform coating and less blocked pores than obtained with a continuous deposition method. Reprinted in adapted form with permission from [9], Copyright 2010 Journal of Physical Chemistry C

In order to quantify the effect of differing electrodeposition parameters on the PPy nanoparticle density and size, SEM, shown in Figure 29, was used to characterize the G/PPy composite film surfaces under various electrodeposition times. It can be seen that the films are uniform with a PPy particle number density increasing with electrodeposition time. SEM was also used for an empirically comparison of the PPy average particle size and particle area density on a nanoparticle/μm^2 basis where images with varying total deposition time were analysed.

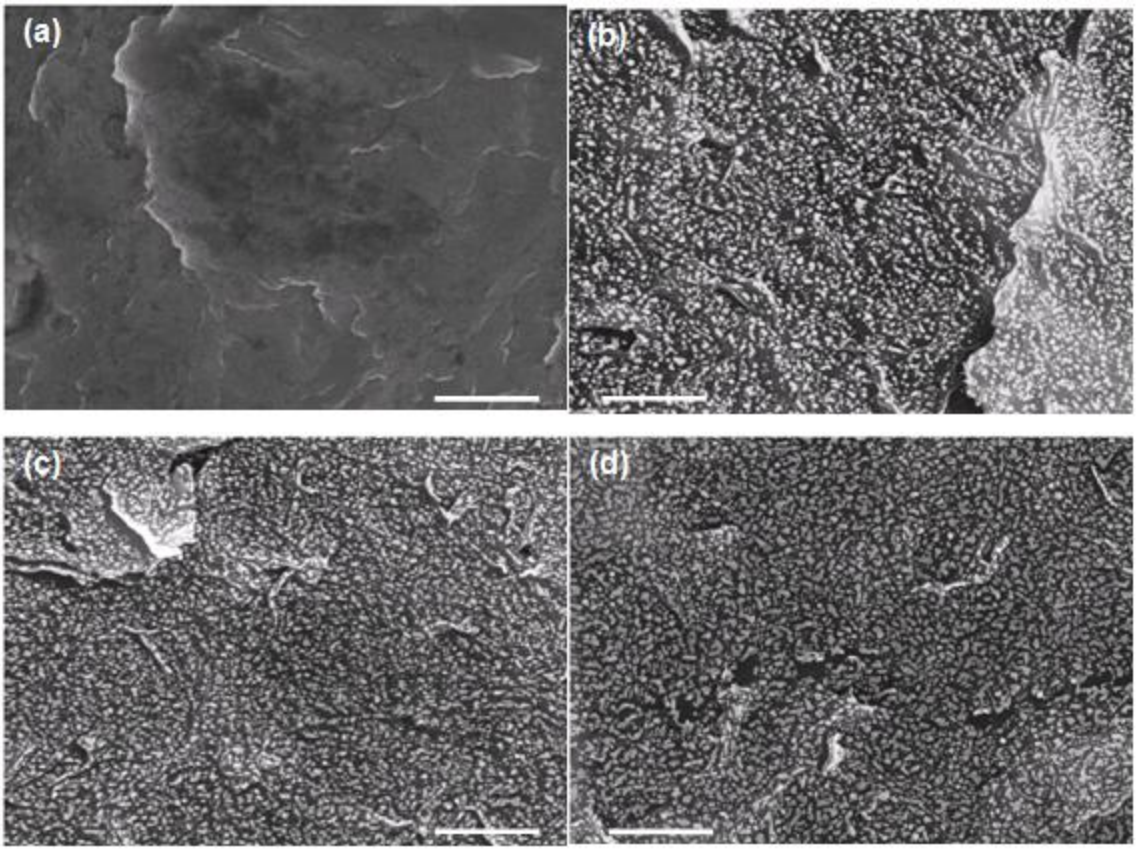

Figure 29: SEM images of (a) pure G and G/PPy after a (b) 60 s, (c) 120 s, (d) 360 s electrodeposition. The white particles are the PPy and the white bar is 1 µm. Reprinted in adapted form with permission from [9], Copyright 2010 Journal of Physical Chemistry C

The results presented in Figure 30(a) show a linear increase in average particle size with electrodeposition time. Previous claims suggest pulsed depositions lead to small, stable nanoparticles *all* of which are nucleated in an initial pulse [124][80]. These particle densities shown in Figure 30(b) appear to substantiate this growth mechanism. As shown, the particle density is increasing with longer electrodeposition times (and therefore greater number of pulses), which suggests that new particles tend to form during each deposition pulse. Combined with average particle size in Figure 30(a), this suggests that many particles are able to relax during a rest pulse, allowing the preferred nucleation of new particles, however some particles do not relax and continue growing during subsequent electrodeposition pulses. It should be noted, however, that given random self-nucleation during a new electrodeposition

pulse and continually increasing particle density, it becomes increasingly likely that a new polymer strand will nucleate on a preexisting particle, thereby resulting in the observed particle size increase. Continuous electrodeposition of polymer would likely produce a relatively constant density independent of deposition time along with an increasing particle size with increasing deposition time, as added monomers tend to polymerize on preexisting polymer chains rather than self nucleate [127].

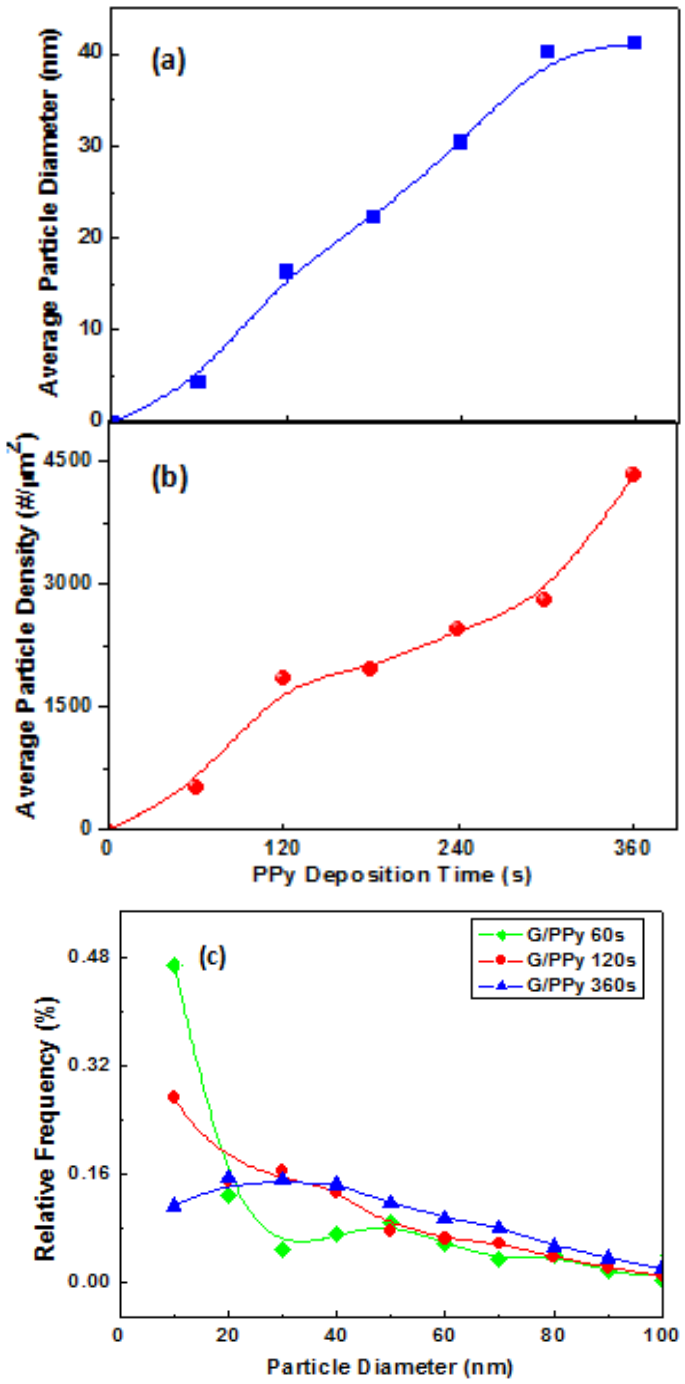

Figure 30: (a) Average PPy particle diameter and (b) average PPy particle density by electrodeposition time as determined by SEM; (c) Particle size distribution of G/PPy 60, 120 and 360. Particles were grouped into intervals with widths of 10nm. Reprinted in adapted form with permission from [9], Copyright 2010 Journal of Physical Chemistry C

It is notable that the PPy particle density does not increase linearly with deposition time. The density increases rapidly up to a total electrodeposition time of 120s is reached, followed by a leveling off as the nucleation rate of new particles decreases. This represents the point at which the tendency for a new polymer chain to nucleate during a deposition pulse becomes less favourable than enlarging an existing PPy particle. The mechanism behind this change in nucleation tendency is likely due to the presence of oxidized defects in the graphene surface, which have been shown to be preferred nucleation sites for crystallite and polymer nucleation [127][128]. Once nucleation has occurred on a majority of the oxidative defects accessible, the energy expenditure for self-nucleation of a new polymer strand increases, making enlargement of an existing strand more energetically favorable.

To gain a more complete analysis of the growth trends at different total deposition times, the particle size distributions at total deposition times of 60, 120 and 360 seconds were calculated and is shown in Figure 30(c). At low deposition times, the vast majority of PPy nanoparticles are under 10 nm in diameter, suggesting most nanoparticles have not grown for more than a single deposition cycle, and nucleation of new nanoparticles is more favourable than enlargement of existing nanoparticles. This peak is notably diminished after 120 seconds of deposition, with a new broad secondary peak appearing for particles with diameters between 20 and 40 nm appearing in addition to the small newly nucleated nanoparticles. The remaining peak at small particle diameters illustrates the continued formation of new nanoparticles, as well as the existence of PPy particles which have stabilized between deposition pulses and do not continue growing with subsequent pulses. After 360 seconds deposition, a very broad peak forms for particles with a diameter between 10 and 60 nm, further showing that particles are both being enlarged and forming with longer depositions contributing to the prevalence of relatively small particles. This extended deposition time has the largest frequency of particles with a greater than 40nm diameter, indicating that particles continue to grow over many deposition pulses. Most notably, very few nanoparticles after this time have diameters under 20 nm, suggesting nucleation of new nanoparticles is

not a majority pathway at this point. The high average particle diameter after this deposition time suggests lower redox-active surface area which will be shown later.

TGA was conducted on the samples to verify an increase in the mass of PPy with longer electrodeposition times. The results of TGA in Figure 31(a) are obtained for a bare PC membrane as a background while Figure 31**(**b) yields the results from G and G/PPy 60, 120 and 360 all of which remain adhered to a PC membrane following preparation. Although the weight percentage drops of PC and PPy slightly overlap each other it remains discernible that the mass of PPy increases in the samples. Indication that the G content makes up a lower percentage of the total mass results from the rate of decreasing mass percent remaining at longer deposition times. As the dimensions of the samples and ratio of G to PC are held constant, the reducing mass that remains after 800°C is attributed to the increasing deposition mass of PPy in the samples. The presence of PPy may also be seen by the mass loss between 200 and 400°C and a more notable loss between 550 to 725°C which is not present in either the PC or G thermograms [129]. The shift in the mass loss seen in the G thermogram indicates that G has a stabilizing effect on the PC. Within the second weight loss region a larger slope of the thermograms for longer deposition times is also indicative of an increasing amount of PPy in the sample. The very sharp loss of mass between 450 and 550°C is attributed to the PC backing membrane with no degradation prior to or following this temperature range [130].

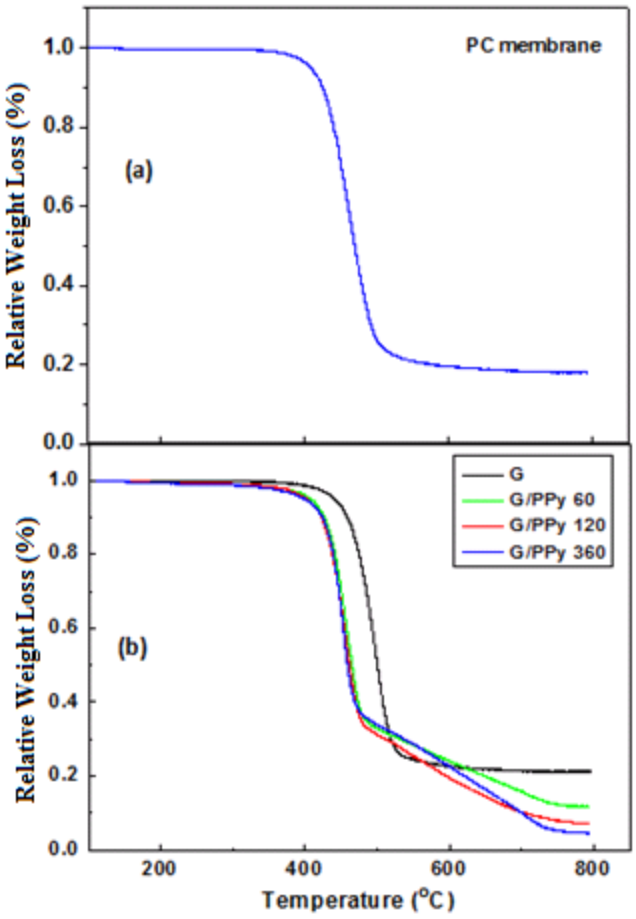

Figure 31: TGA thermograms of (a) PC membrane and (b) G and G/PPy 60, 120 and 360. Reprinted in adapted form with permission from [9], Copyright 2010 Journal of Physical Chemistry C

Figure 32(a-d) shows CV curves for pure G and G/PPy 60, 120 and 360 at varied scan rates between -0.4 and 0.6 V vs. SCE in 1 M KCl. The CV curve for G is virtually rectangular to show an approach to ideal and reversible capacitive behaviour was achieved. With pulse deposited PPy, the shapes of CV show double layer behavior and feature of pseudocapacitive activity from PPy between -0.25 to 0.25 [131]. With extended electrodepostion time, the curve demonstrates a more significant contribution from pseudocapacitive activity of PPy, which is consistent with the particle density results shown in Figure 30(b). The specific capacitances of the electrodes were determined by CV using Eq. 7.

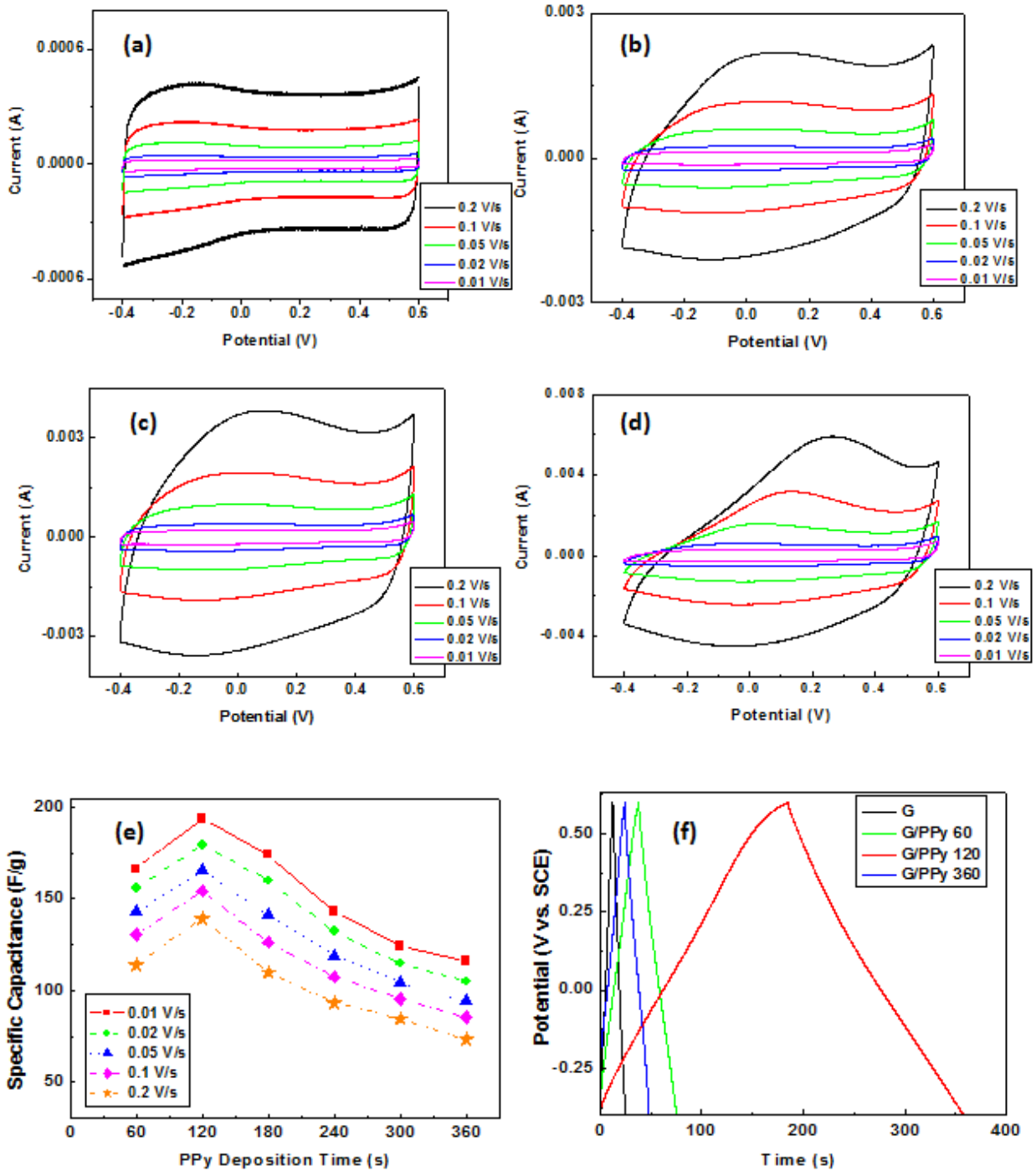

Figure 32: Cyclic Voltammograms curves for the (a) G, (b) G-PPy60, (c) G-PPy120 and (d) G-PPy360 electrodes in a KCl solution between -0.4 and 0.6 V vs. SCE at scan rates of 0.01, 0.02, 0.05, 0.1 and 0.2 V · s-1. (e) Specific Capacitance of all the G/PPy electrodes by electrodeposition time as determined by CV with different scan rates. (f) Galvanostatic Charge-Discharge curves for the G, G-PPy60, G-PPy120 and G-PPy360 electrodes for comparison at a current density of 1 A · g-1 between -0.4 and 0.6 V vs. SCE in 1 M KCl. Reprinted in adapted form with permission from [9], Copyright 2010 Journal of Physical Chemistry C

Through CV analysis of the voltammograms, the electrodes yield specific capacitances ranging from ~194 $F \cdot g^{-1}$ for the G/PPy 120s electrode at a scan rate of 10 $mV \cdot s^{-1}$ and ~47 $F \cdot g^{-1}$ for the graphene electrode at 200$mV \cdot s^{-1}$. Figure 32(e) shows the specific capacitance values of all of the electrodes at the various scan rates. G/PPy 120 shows the best performance at all scan rates due to the PPy morphology obtained after 120 sec of pulsed electrodeposition. As shown by SEM and elaborated on above, G/PPy 120 has a high particle density while still maintaining a relatively low average particle size, leading to a large redox-active surface area able to contribute to the material's pseudocapacitance. The large and densely packed PPy particle growth of G/PPy 360 (Figure 29d) is undesirable for fast ion kinetics and is attributed to the decrease performance.

The CD curves in Figure 32(f) were obtained at a current density of 1 $A \cdot g^{-1}$ between -0.4 and 0.6 V vs. SCE in 1 M KCl for pure G and G/PPy 60, 120 and 360. Near ideal EDLC behavior of the CD curves is seen by the highly linear charge and discharge slopes. Approach to ideality is also noted by the symmetry of the charge and discharge slopes[1]. The slight curvature of the slopes of the G/PPy electrodes are indicative of the pseudocapacitive effects of the PPy and as expected the curvature becomes more pronounced with longer electrodeposition times indicating increased contribution of pseudocapacitance to the systems. The G/PPy 120 shows a minimal internal resistance (IR) drop upon initiated charge and discharge illustrating the low contact resistance of the G/PPy composites and efficient use of a capacitance current [132]. This quality reduces the amount of energy lost to contact resistance with each charge/discharge cycle in the form of heat.

Specific capacitance values of the electrodes from CD were derived from Eq. 9. Nyquist plots are shown in Figure 33 resulting from EIS data obtained for pure G and composites G/PPy 60, 120 and 360 at open circuit potential (OCP). At low frequencies the real portion of the impedance approaches a finite value, while the imaginary portion of the capacitive reactance impedance nears infinity. All EIS plots in Figure 33 are shown to exhibit this behavior at low frequencies, denoting their approach to ideal capacitance. A change of the mid-range frequency impedances in both G/PPy 60 and G/PPy 120 gives

rise to a visible knee frequency, characteristic of the transition from frequency dependent diffusion resistance to pure capacitive charging behavior. A Warburg element is often used to describe ion-diffusion resistances and is made apparent by a 45° phase angle. The frequency dependent diffusion resistance increases with an increase in deposition time as both the number of particles and particle size of PPy continue to increase. The absence of ion diffusion and charge transfer resistances of the untreated graphene sheets contrasts. With a deposition time t > 300s the electrodeposition of Py is shown to favour increasing the size of existing particles, and the EIS of Figure 33d (G/PPy 360) observes a corresponding increase in the parallel resistances present within the composite. Contributing factors to this resistance include charge transfer resistances and parallel faradaic resistances owing to pseudocapacitive materials. Increasing the size and amount of PPy particles can be expected to increase the diffusion resistance of Cl^- doping ion as well as the related charge-transfer resistance of the redox reaction. It is interesting to note the EIS of shorter deposition times lack the latter resistance, and primarily contribute towards increasing the diffusion resistances which are attributed to a change in the pore size and structure of individual graphene sheets.

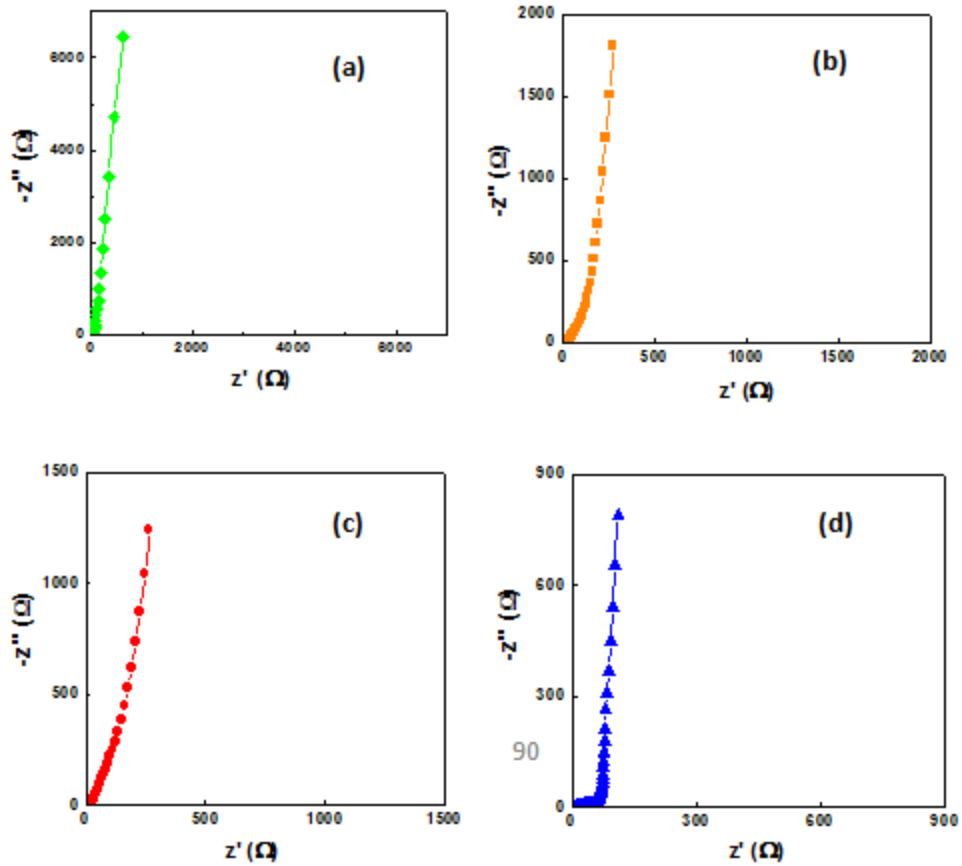

Figure 33: Nyquist plots of the G/PPy electrodes for (a) G, (b) G-PPy60, (c) G-PPy120 and (d) G-PPy360 at frequencies between 1 MHz and 10 mHz with a sinusoidal signal amplitude of 0.01 V vs. SCE in 1 M KCl. Reprinted in adapted form with permission from [9], Copyright 2010 Journal of Physical Chemistry C

The energy densities of the electrodes were calculated using Eq. 11. A high energy density of 26.9 Wh · kg^{-1} was derived from CV data for G/PPy 120 at a scan rate of 10 mV · s^{-1} and 6.5Wh · kg^{-1} for G at 200mV · s^{-1}.

The power densities of the electrodes were calculated from the corresponding energy densities using Eq. 13. Following this analysis, a Ragone plot in Figure 34 shows the power and energy densities for pure G and composites G/PPy 60, 120 and 360. The addition of PPy to pure G leads to a significant improvement in both the energy and power density of the composite material to suggest a synergistic effect. The trend of power and energy density with electrodeposition time denotes an optimal 120 s electrodeposition. Increasing the deposition time beyond 120 s results in undesirable power loss from

resistances, and a greater impedance in developing a higher energy density as a result of the loss of current responsible for capacitive charging.

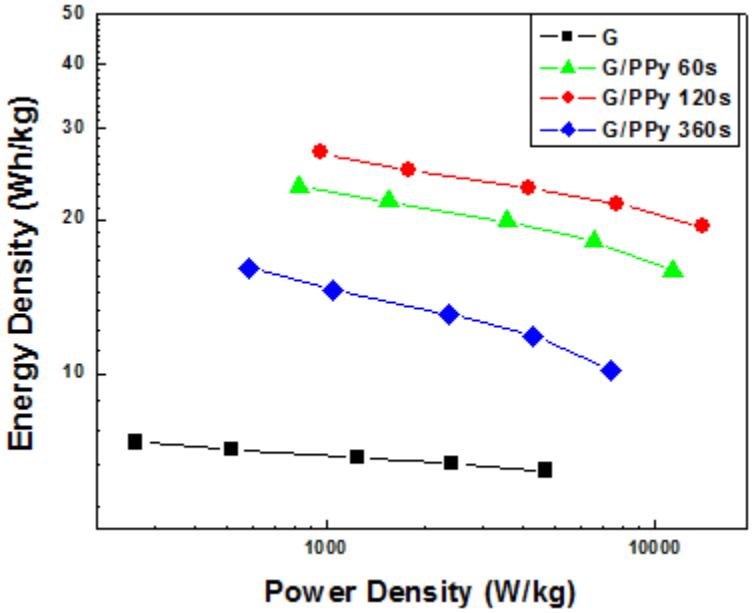

Figure 34: Ragone plot of the energy density vs. power density of the pure G and G/PPy 60, 120 and 360 electrodes, where capacitance data from CV analysis was applied.

6.4 Conclusions

In conclusion, a simple method to create flexible, uniform G/PPy composite films using a pulsed electrodeposition technique was presented. Specific capacitances as high as 203F · g^{-1} were obtained for a moderate deposition time of 120s. This result compares favourably to studies with much longer and complex processes for deposition of PPy to different carbon scaffolds. G/PPy 120 also exhibited the highest energy and power densities with maximum values of ~27 Wh · kg^{-1} and ~14kW · kg^{-1} respectively which were notably higher than the values obtained for all other electrodes and compare very favourably to literature values [48][80]. It has been clearly shown by SEM that increased electrodeposition time results in increased particle density up to 120 seconds total deposition time. This increase was attributed to the favourable nucleation of new polymer chains at defects in the graphene surface, which becomes less favourable as defect sites are covered by existing polymer nanoparticles.

With the addition of a pseudocapacitive contribution to graphene supercapacitor electrodes due to a conformal nanoparticle coating of redox-active PPy, it is possible to obtain high power and energy densities while still maintaining the inherent flexibility of graphene films. It is expected that the increases in energy and power densities in a flexible material can lead to numerous applications, particularly in the field of personal electronics and renewable energy storage. Future work with the optimal G/PPy 120 material is to fabricate two electrode supercapacitor devices, as shown by a schematic in Figure 35 that retain the flexibility and high capacitance observed in this project.

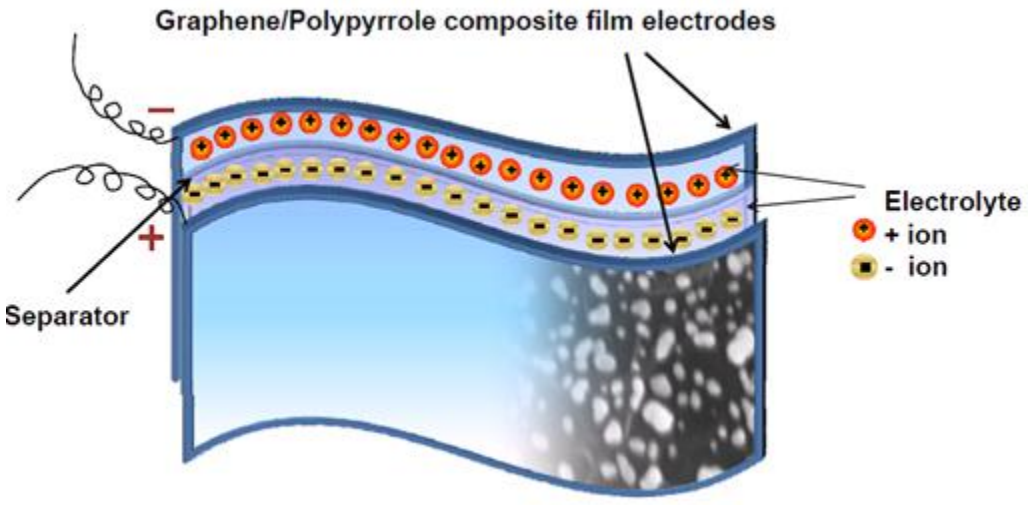

Figure 35: A schematic of a hypothetical two electrode device fabricated with G/PPy 120 composite material for future work.

7.0 Summary and perspective towards future research

In conclusion, the successful development of GNP materials for application as supercapacitor electrodes was demonstrated through the investigations detailed in three distinct studies. The principal goal to fabricate electro-active materials from GNP was intended to exploit the unique physical and electrochemical properties of this two dimensional carbon nanostructure in enhancing the electrochemical double-layer capacitance. Efforts to improve the measurable capacitance of carbon supercapacitor materials, as well as synergistically integrate it with additional EDLC and pseudocapacitive species were the primary motivations behind this work, as the energy storage capabilities of present supercapacitors are a magnitude less their battery counterparts.

The first study was focused entirely on fabrication thin and transparent, flexible electrodes of GNP to evaluate its energy and power densities capabilities. The theoretical high surface area attainable by GNP in addition to its robust and highly electron conducting structure supported the rationale for its application as a EDLC supercapacitor electrode material, where the resulting investigation and obtained supported it valid usage. A high energy and power density could be obtained from the ultra-thin electrode films demonstrating its potential application in optical, and portable electronics as an energy storage device. In addition, its favorable electrical conductance demonstrated its high potential for high-power fast charging applications.

The second study investigated the integration of additional nanostructured carbons, specifically SWNT and MWNT to increase the electro-active surface area accessible to electrolyte ions and reduce inter-particle sheet resistances. While increasing the specific surface area of an EDLC electrode theoretically correlates to an increase in capacitance, several efforts have demonstrated that pore size and distribution a more influential factor through experimental analysis. Hybridization of a MWNT and GNP resulted in a lower capacitance pertaining to a performance that directly correlates to the mass fraction present from each, thus yielding a mean capacitance equated to be a rough average of each pure specimen. The SWNT

and GNP composite; however, was shown to be successful in yielding a slight increase in specific capacitance indicative that the initial objective was achievable. Justification of this performance was largely attributed to the relative aspect ratios of each CNT type and the corresponding pore sizes they are likely to generate through integration with GNP.

The final study sought to integrate a pseudocapacitive ECP material in order to improve upon the energy density through redox reaction mechanisms. Generally found to be unstable when used independently, ECPs have been demonstrated to show improved reliability when supported by highly robust carbon materials. Thus PPy was electro-deposited through a pulse deposition to make effective use of GNP surface area and structure. An optimal high specific capacitance with respect to total deposition was successful attained; with a predominant pseudocapacitive reduction/oxidation capacitance achievable through this effort.

The studies summarily presented herein emphasize graphene nanoplatelets as a EDLC carbon electrode for use in supercapacitor devices. Evaluation of the physical structure, including surface morphology and transparency in conjunction with electrochemical measurements of its specific gravimetric capacitance, energy and power densities support further research into this field of application. Future endeavors can further investigate:

- Procedures that increase and correspondingly preserve a highly accessible surface area for EDLC
- Investigation towards the development of composite GNP electrodes using either aEDLC or pseudocapacitive materials where the corresponding pore size and distribution can be manipulated
- Development of two-electrode full cell supercapacitor devices to further evaluate GNP and GNP composite suitability as a commercially viable electrode material

References

[1] H.E. Becker, “Low Voltage Electrolytic Capacitor,” , 1957.

[2] B.E. Conway, V. Birss, and J. Wojtowicz, “The role and utilization of pseudocapacitance for energy storage by supercapacitors,” *J. Power Sources*, vol. 66, 1997, pp. 1-14.

[3] B.E. Conway, “Transition from "Supercapacitor" to "Battery" Behavior in Electrochemical Energy Storage,” *J. Electrochem. Soc.*, vol. 138, 1991, pp. 1539-1548.

[4] P. Simon and Y. Gogotsi, “Materials for electrochemical capacitors,” *Nat. Mater.*, vol. 7, 2008, pp. 845-854.

[5] M. Armand and J.M. Tarascon, “Building better batteries,” *Nature*, vol. 451, 2008, pp. 652-657.

[6] K. Rand, “DOE Panel on Advanced Energy Storage Systems Calls for Materials Research,” *MRS Bulletin - MRS*, vol. 32, 2007, p. 464.

[7] J.R. Miller and A.F. Burke, “Electrochemical Capacitors: Challenges and Opportunities for Real-World Applications,” *Electrochemical Society Interface*, vol. 17, 2008, pp. 53-57.

[8] A. Yu, I. Roes, A. Davies, and Z. Chen, “Ultrathin, transparent, and flexible graphene films for supercapacitor application,” *Appl. Phys. Lett.*, vol. 96, 2010, p. 253105 253108.

[9] A. Davies, P. Audette, B. Farrow, F. Hassan, Z. Chen, J.-yeon Choi, and A. Yu, “Graphene-Based Flexible Supercapacitors : Pulse-Electropolymerization of Polypyrrole on Free-Standing Graphene Films,” *Journal of Physical Chemistry C*, 2011, pp. 17612-17620.

[10] A.G. Pandolfo and A.F. Hollenkamp, “Carbon properties and their role in supercapacitors,” *J. Power Sources*, vol. 157, 2006, pp. 11-27.

[11] L.L. Zhang and X.S. Zhao, “Carbon-based materials as supercapacitor electrodes.,” *Chemical Society reviews*, vol. 38, Sep. 2009, pp. 2520-31.

[12] D.W. Wang, F. Li, M. Liu, G.Q. Lu, and H.M. Cheng, “3D Aperiodic Hierarchical Porous Graphitic Carbon Material for High-Rate Electrochemical Capacitive Energy Storage,” *Angew. Chem. Int. Ed.*, vol. 47, 2008, pp. 373-376.

[13] Y. Han and Y. Lu, “Characterization and electrical properties of conductive polymer/colloidal graphite oxide nanocomposites,” *Compos. Sci. Technol.*, vol. 69, 2009, pp. 1231-1237.

[14] H. Pan, J.Y. Li, and Y.P. Feng, "Carbon Nanotubes for Supercapacitor," *Nanoscale Research Letters*, vol. 5, 2010, pp. 654-668.

[15] C.N.R. Rao, A.K. Sood, K.S. Subrahmanyam, and A. Govindaraj, "Graphene: The New Two-Dimensional Nanomaterial ," *Angew. Chem. Int. Ed.*, vol. 48, 2009, pp. 7752-7777.

[16] P. Jampani, A. Manivannan, and N.K. Prashant, "Advancing the Supercapacitor Materials and Technology Frontier for Improving Power Quality," *The Electrochemical Society Interface*, vol. 19, 2010, pp. 57-62.

[17] A.K. Shukla, S. Sampath, and K. Vijayamohanan, "Electrochemical supercapacitors: Energy storage beyond batteries," *Current Science*, vol. 79, 2000, pp. 1656-1661.

[18] B.E. Conway, *Electrochemical Supercapacitors*, New York: Plenum Publishing, 1999.

[19] A. Malak, K. Fic, G. Lota, C. Vix-Guterl, and E. Frackowiak, "Hybrid materials for supercapacitor application," *J. Solid State Electrochem.*, vol. 14, 2010, pp. 811-816.

[20] G.G. Amatucci, F. Badway, A. Du Pasquier, and T. Zheng, "An asymmetric hybrid nonaqueous energy storage cell," *J. Electrochem. Soc.*, vol. 148, 2001, pp. 930-939.

[21] K. Naoi, S. Ishimoto, Y. Isobe, and S. Aoyagi, "High-rate nano-crystalline Li4Ti5O12 attached on carbon nano-fibers for hybrid supercapacitors," *Journal of Power Sources*, vol. 195, 2010, pp. 6250-6254.

[22] D.W. Wang, H.T. Fang, L. Feng, Z.G. Chen, G.Q. Zhong, and H.M. Cheng, "Aligned Titania Nanotubes as an Intercalation Anode Material for Hybrid Electrochemical Energy Storage," *Adv. Funct. Mater.*, vol. 18, 2008, pp. 3787-3793.

[23] H. von Helmholtz, "On the laws of the distribution of electrical currents in material conductors with application to experiments in animal electricity," *Ann. Phys. - Paris*, vol. 243, 1879, pp. 337-382.

[24] J.O. Brockis, A.K.N. Reddy, and M.E. Gamboa-Aldeco, *Fundamentals of Electrodics 2A*, New York: Kluwer Academic/Plenum Publishers, 2000.

[25] D.L. Chapman, "A contribution to the theory of electrocapillariy," *Philos. Mag. Ser.*, vol. 6, 1913, pp. 475-481.

[26] G. Gouy, "Interferences with large path differences," *Ann. Phys. - Paris*, vol. 7, 1917.

[27] O. Stern, "The theory of the electrolytic double shift," *Zeitschrift Fur Elektrochemie Und Angewandte Physikalische Chemie*, vol. 30, 1924, pp. 508-516.

[28] R. Parsons, *Modern Aspects of Electrochemistry*, London: Buttersworth, 1954.

[29] D.C. Grahame, “The Electrical Double Layer and the Theory of Electrocapillarity,” *Chem. Rev.*, vol. 41, 1947, pp. 441-501.

[30] B.E. Conway, “Transition from Supercapacitor to Battery Behavior in Electrochemical Energy-Storage,” *J. Electrochem. Soc.*, vol. 138, 1991, pp. 1539-1548.

[31] B.E. Conway and E. Gileadi, “Kinetic theory of pseudo-capacitance and electrode reactions at appreciable surface coverage,” *Trans. Faraday Soc.*, vol. 58, 1962, pp. 2493-2509.

[32] Y.S. Lin, K.Y. Lee, K.Y. Chen, and Y.S. Huang, “Superior capacitive characteristics of RuO2 nanorods grown on carbon nanotubes,” *Applied Surface Science*, vol. 256, 2009, pp. 1042-1045.

[33] C. Peng, J. Jin, and G.Z. Chen, “A comparative study on electrochemical co-deposition and capacitance of composite films of conducting polymers and carbon nanotubes,” *Electrochim. Acta*, vol. 53, 2007, pp. 525-537.

[34] A.S. Aricò, P. Bruce, B. Scrosati, J.-M. Tarascon, and W. van Schalkwijk, “Nanostructured materials for advanced energy conversion and storage devices.,” *Nature materials*, vol. 4, May. 2005, pp. 366-77.

[35] J. Chmiola, G. Yushin, R. Dash, and Y. Gogotsi, “Effect of pore size and surface area of carbide derived carbons on specific capacitance,” *J. Power Sources*, vol. 158, 2006, pp. 765-772.

[36] E. Frackowiak, “Carbon materials for supercapacitor application.,” *Physical chemistry chemical physics : PCCP*, vol. 9, Apr. 2007, pp. 1774-85.

[37] J. Chmiola, G. Yushin, Y. Gogotsi, C. Portet, P. Simon, and P.L. Taberna, “Anomalous increase in carbon capacitance at pore sizes less than 1 nanometer,” *Science*, vol. 313, 2006, pp. 1760-1763.

[38] B. McEnaney, *Introduction to Carbon Science*, London: Butterworths, 1989.

[39] M. Pumera, B. Smid, and K. Veltruska, “Influence of nitric acid treatment of carbon nanotubes on their physico-chemical properties,” *Journal of Nanoscience and Nanotechnology*, vol. 9, 2009, pp. 2671-2676.

[40] E. Frackowiak, K. Metenier, R. Pellenq, S. Bonnamy, and F. Beguin, “Capacitance properties of carbon nanotubes,” *Electronic Properties of Novel Materials - Science and Technology of Molecular Nanostructures*, vol. 486, 1999, pp. 429-432.

[41] K. Jurewicz, S. Delpeux, V. Bertagna, F. Beguin, and E. Frackowiak, “Supercapacitors from nanotubes/polypyrrole composites,” *Chem. Phys. Lett.*, vol. 347, 2001, pp. 36-40.

[42] C. Liu, F. Li, L.P. Ma, and H.M. Cheng, “Advanced Materials for Energy Storage,” *Adv. Mater.*, vol. 22, 2010, pp. 28-62.

[43] L.L. Zhang and X.S. Zhao, “Carbon-based materials as supercapacitor electrodes,” *Chemical Society reviews*, vol. 38, 2009, pp. 2520-2531.

[44] D.N. Futaba, K. Hata, T. Yamada, T. Hiraoka, Y. Hayamizu, Y. Kakudate, O. Tanaike, H. Hatori, M. Yumura, and S. Iijima, “Shape-engineerable and highly densely packed single-walled carbon nanotubes and their application as super-capacitor electrodes,” *Nature Materials*, vol. 5, 2006, pp. 987-994.

[45] T. Bordjiba, M. Mohamedi, and L.H. Dao, “New class of carbon-nanotube aerogel electrodes for electrochemical power sources,” *Adv. Mater.*, vol. 20, 2008, pp. 815-819.

[46] a K. Geim and K.S. Novoselov, “The rise of graphene.,” *Nature materials*, vol. 6, Mar. 2007, pp. 183-91.

[47] C. Liu, Z. Yu, D. Neff, A. Zhamu, and B.Z. Jang, “Graphene-Based Supercapacitor with an Ultrahigh Energy Density.,” *Nano letters*, vol. 10, Nov. 2010, pp. 4863-4868.

[48] Y. Wang, Z. Shi, Y. Huang, Y. Ma, C. Wang, M. Chen, and Y. Chen, “Supercapacitor Devices Based on Graphene Materials,” *J. Phys. Chem. C*, vol. 113, 2009, pp. 13103-13107.

[49] M.D. Stoller, S.J. Park, Y.W. Zhu, J.H. An, and R.S. Ruoff, “Graphene-Based Ultracapacitors,” *Nano Lett.*, vol. 8, 2008, pp. 3498-3502.

[50] A. Lewandowski and M. Galinski, “Practical and theoretical limits for electrochemical double-layer capacitors,” *J. Power Sources*, vol. 173, 2007, pp. 822-828.

[51] J.-H. Chen, C. Jang, S. Adam, M.S. Fuhrer, E.D. Williams, and M. Ishigami, “Charged-impurity scattering in graphene,” *Nature Physics*, vol. 4, 2008, pp. 377-381.

[52] A.B. Kuzmenko, E.V. Heumen, F. Carbone, and D.V.D. Marel, “Universal Optical Conductance of Graphite,” *Physical Review Letters*, vol. 100, 2008, pp. 117401-117404.

[53] C. Lee, X. Wei, J.W. Kysar, and J. Hone, “Measurement of the elastic properties and intrinsic strength of monolayer graphene,” *Science*, vol. 321, 2008, pp. 385-388.

[54] R. Ruoff, “Calling all chemists,” *Nature Nanotechnology*, vol. 3, 2008, pp. 10-11.

[55] X. Wang, X. Li, L. Zhang, Y. Yoon, P.K. Weber, H. Wang, J. Guo, and H. Dai, “N-doping of graphene through electrothermal reactions with ammonia,” *Science*, vol. 324, 2009, pp. 768-771.

[56] M.D. Stoller, S.J. Park, Y.W. Zhu, J.H. An, and R.S. Ruoff, "Graphene-Based Ultracapacitors," *Nano Lett.*, vol. 8, 2008, pp. 3498-3502.

[57] Y. Wang, Z. Shi, Y. Huang, Y. Ma, C. Wang, M. Chen, and Y. Chen, "Supercapacitor Devices Based on Graphene Materials," *J. Phys. Chem. C*, vol. 113, 2009, pp. 13103-13107.

[58] D.-W. Wang, F. Li, J. Zhao, W. Ren, Z.-G. Chen, J. Tan, Z.-S. Wu, I. Gentle, G.Q. Lu, and H.-M. Cheng, "Fabrication of Graphene/Polyaniline Composite Paper via In Situ Anodic Electropolymerization for High-Performance Flexible Electrode.," *ACS nano*, vol. 3, Jun. 2009, pp. 1745-1752.

[59] M.H. Liang, B. Luo, and L.J. Zhi, "Application of graphene and graphene-based materials in clean energy-related devices," *Int. J. Energ. Res.*, vol. 33, 2009, pp. 1161-1170.

[60] T.-K. Hong, D.W. Lee, H.J. Choi, H.S. Shin, and B.-S. Kim, "Transparent, flexible conducting hybrid multilayer thin films of multiwalled carbon nanotubes with graphene nanosheets.," *ACS nano*, vol. 4, Jul. 2010, pp. 3861-8.

[61] X. Li, G. Zhang, X. Bai, X. Sun, X. Wang, E. Wang, and H. Dai, "Highly conducting graphene sheets and Langmuir-Blodgett films.," *Nature nanotechnology*, vol. 3, Sep. 2008, pp. 538-42.

[62] S. Biswas and L.T. Drzal, "Multilayered Nanoarchitecture of Graphene Nanosheets and Polypyrrole Nanowires for High Performance Supercapacitor Electrodes," *ACS applied materials & interfaces*, 2010, pp. 5667-5671.

[63] K.S. Kim, Y. Zhao, H. Jang, S.Y. Lee, J.H. Kim, J.-H. Ahn, P. Kim, J.-Y. Choi, and B.H. Hong, "Large-scale pattern growth of graphene films for stretchable transparent electrodes," *Nature*, vol. 457, 2009, pp. 706-710.

[64] Y. Xu, H. Bai, G. Lu, C. Li, and G. Shi, "Flexible graphene films via the filtration of water-soluble noncovalent functionalized graphene sheets.," *Journal of the American Chemical Society*, vol. 130, May. 2008, pp. 5856-7.

[65] J.P. Zheng, P.J. Cygan, and T.R. Jow, "Hydrous Ruthenium Oxide as an Electrode Material for Electrochemical Capacitors," *Journal of The Electrochemical Society*, vol. 142, 1995, pp. 2699-2703.

[66] T. Cottineau, M. Toupin, T. Delahaye, T. Brousse, and D. Bélanger, "Nanostructured transition metal oxides for aqueous hybrid electrochemical supercapacitors," *Applied Physics A*, vol. 82, Nov. 2005, pp. 599-606.

[67] X.P. Zhou, H.Y. Chen, D. Shu, C. He, and J.M. Nan, "Study on the electrochemical behavior of vanadium nitride as a promising supercapacitor material," *Journal of Physics and Chemistry of Solids*, vol. 70, 2009, pp. 495-500.

[68] N.L. Wu, “Nanocrystalline oxide supercapacitors,” *Materials Chemistry and Physics*, vol. 75, 2002, pp. 6-11.

[69] L.L. Zhang, T. Wei, W. Wang, and X.S. Zhao, “Manganese oxide-carbon composite as supercapacitor electrode materials,” *Microporous Mesoporous Mater.*, vol. 123, 2009, pp. 260-267.

[70] T. Brousse, M. Toupin, R. Dugas, L. Athouel, O. Crosnier, and D. Belanger, “Crystalline MnO2 as possible alternatives to amorphous compounds in electrochemical supercapacitors,” *J. Electrochem. Soc.*, vol. 153, 2006, pp. 2171-2180.

[71] J.P. Zheng, “A New Charge Storage Mechanism for Electrochemical Capacitors,” *Journal of The Electrochemical Society*, vol. 142, 1995, p. L6.

[72] S.W. Zhang and G.Z. Chen, “Manganese oxide based materials for supercapacitors,” *Energy Materials*, vol. 3, 2008, pp. 186-200.

[73] S.C. Pang and M.A. Anderson, “Novel electrode materials for ultracapacitors: Structural and electrochemical properties of sol-gel-derived manganese dioxide thin films,” *New Materials for Batteries and Fuel Cells*, vol. 575, 2000, pp. 415-421.

[74] E. Frackowiak, V. Khomenko, K. Jurewicz, K. Lota, and F. Beguin, “Supercapacitors based on conducting polymers/nanotubes composites,” *J. Power Sources*, vol. 153, 2006, pp. 413-418.

[75] H. Wang, Q. Hao, X. Yang, L. Lu, and X. Wang, “Graphene oxide doped polyaniline for supercapacitors,” *Electrochemistry Communications*, vol. 11, Jun. 2009, pp. 1158-1161.

[76] B. Schulz, B. Dietzel, I. Orgzall, I. Diez, and C. Xu, “Aspects of Morphology Control during the Oxidative Synthesis of Electrically Conducting Polymers,” *High Performance Polymers*, vol. 21, Sep. 2009, pp. 633-652.

[77] K. Zhang, L.L. Zhang, X.S. Zhao, and J. Wu, “Graphene/Polyaniline Nanofiber Composites as Supercapacitor Electrodes,” *Chemistry of Materials*, vol. 22, Feb. 2010, pp. 1392-1401.

[78] A. Rudge, J. Davey, I. Raistrick, S. Gottesfeld, and J.P. Ferraris, “Conducting Polymers as Active Materials in Electrochemical Capacitors,” *Journal of Power Sources*, vol. 47, 1994, pp. 89-107.

[79] Y. Zhang, H. Feng, X. Wu, L. Wang, A. Zhang, T. Xia, H. Dong, X. Li, and L. Zhang, “Progress of electrochemical capacitor electrode materials: A review,” *International Journal of Hydrogen Energy*, vol. 34, Jun. 2009, pp. 4889-4899.

[80] J. Yan, T. Wei, Z. Fan, W. Qian, M. Zhang, X. Shen, and F. Wei, "Preparation of graphene nanosheet/carbon nanotube/polyaniline composite as electrode material for supercapacitors," *J. Power Sources*, vol. 195, 2010, pp. 3041-3045.

[81] V. Khomenko, E. Raymundo-Pinero, E. Frackowiak, and F. Beguin, "High-voltage asymmetric supercapacitors operating in aqueous electrolyte," *Applied Physics A*, vol. 82, 2006, pp. 567-573.

[82] A. Burke, "R&D considerations for the performance and application of electrochemical capacitors," *Electrochim. Acta*, vol. 53, 2007, pp. 1083-1091.

[83] A.F. Burke, "Batteries and ultracapacitors for electric, hybrid, and fuel cell vehicles," *Proceedings of the Ieee*, vol. 95, 2007, pp. 806-820.

[84] A. Lewandowski, A. Olejniczak, M. Galinski, and I. Stepniak, "Performance of carbon–carbon supercapacitors based on organic, aqueous and ionic liquid electrolytes," *Journal of Power Sources*, vol. 195, Sep. 2010, pp. 5814-5819.

[85] G.I. Goldstein, D.E. Newbury, P. Echlin, D.C. Joy, C. Fiori, and E. Lifshin, *Scanning electron microscopy and x-ray microanalysis*, New York: Springer, 2003.

[86] D.A. Skoog, F.J. Holler, and S.R. Crouch, *Principles of Instrumental Analysis*, Brooks Cole, 2006.

[87] X. Zhao, H. Tian, M. Zhu, K. Tian, J.J. Wang, F. Kang, and R. a Outlaw, "Carbon nanosheets as the electrode material in supercapacitors," *Journal of Power Sources*, vol. 194, Dec. 2009, pp. 1208-1212.

[88] H. Wang, Q. Hao, X. Yang, L. Lu, and X. Wang, "Graphene oxide doped polyaniline for supercapacitors," *Electrochemistry Communications*, vol. 11, 2009, pp. 1158-1161.

[89] J. Chmiola, G. Yushin, R. Dash, and Y. Gogotsi, "Effect of pore size and surface area of carbide derived carbons on specific capacitance," *Journal of Power Sources*, vol. 158, Jul. 2006, pp. 765-772.

[90] R.A. Huggins, "Supercapacitors and electrochemical pulse sources," *Solid State Ionics*, vol. 134, 2000, pp. 179-195.

[91] R. de Levie, "On porous electrodes in electrolyte solutions I. Capacitance effects," *Electrochimica Acta*, vol. 8, Oct. 1963, pp. 751-780.

[92] R. Kotz and M. Carlen, "Principles and applications of electrochemical capacitors," *Electrochim. Acta*, vol. 45, 2000, pp. 2483-2498.

[93] J. Wang, Y. Xu, X. Chen, and X. Sun, "Capacitance properties of single wall carbon nanotube/polypyrrole composite films," *Composites Science and Technology*, vol. 67, Nov. 2007, pp. 2981-2985.

[94] D.A. Evans and J.R. Miller, "Hybrid electrolytic/electrochemical capacitor for electric vehicles," *Proceedings of the Symposium on Electrochemical Capacitors Ii*, vol. 96, 1997, pp. 253-257 337.

[95] B. Dunn, J.W. Long, and D.R. Rolison, "Rethinking Multifunction in Three Dimensions for Miniaturizing Electrical Energy Storage," *Electrochemical Society Interface*, 2008, pp. 49-53.

[96] G. Eda, G. Fanchini, and M. Chhowalla, "Large-area ultrathin films of reduced graphene oxide as a transparent and flexible electronic material.," *Nature nanotechnology*, vol. 3, May. 2008, pp. 270-4.

[97] S. Ju, J.F. Li, J. Liu, P.C. Chen, Y.G. Ha, F. Ishikawa, H. Chang, C.W. Zhou, A. Facchetti, D.B. Janes, and T.J. Marks, "Transparent active matrix organic light-emitting diode displays driven by nanowire transistor circuitry," *Nano Lett.*, vol. 8, 2008, pp. 997-1004.

[98] P.C. Chen, G. Shen, S. Sukcharoenchoke, and C. Zhou, "Flexible and transparent supercapacitor based on In2O3 nanowire/carbon nanotube heterogeneous films," *Appl. Phys. Lett.*, vol. 94, 2009, p. -.

[99] J. Yan, T. Wei, B. Shao, F. Ma, and Z. Fan, "Electrochemical properties of graphene nanosheet / carbon black composites as electrodes for supercapacitors," *Carbon*, vol. 48, 2010, pp. 1731-1737.

[100] N.J. Dudney, "Thin Film Micro-Batteries," *Electrochemical Society Interface*, 2008.

[101] L.L. Zhang, R. Zhou, and X.S. Zhao, "Graphene-based materials as supercapacitor electrodes," *Journal of Materials Chemistry*, vol. 20, 2010, pp. 5983-5992.

[102] S.R.C. Vivekchand, C.S. Rout, K.S. Subrahmanyam, A. Govindaraj, and C.N.R. Rao, "Graphene-based electrochemical supercapacitors," *Journal of Chemical Sciences*, vol. 120, 2008, pp. 9-13.

[103] S.R.C. Vivekchand, C.S. Rout, K.S. Subrahmanyam, a Govindaraj, and C.N.R. Rao, "Graphene-based electrochemical supercapacitors," *Journal of Chemical Sciences*, vol. 120, Mar. 2008, pp. 9-13.

[104] W.S. Hummers and R.E. Offeman, "Preparation of Graphitic Oxide," *J. Am. Chem. Soc.*, vol. 80, 1957, p. 1339.

[105] B.C. Brodie, "On the Atomic Weight of Graphite," *Philosophical Transactions of the Royal Society of London*, vol. 149, Jan. 1859, pp. 249-259.

[106] H.C. Schniepp, J.-L. Li, M.J. McAllister, H. Sai, M. Herrera-Alonso, D.H. Adamson, R.K. Prud'homme, R. Car, D. a Saville, and I. a Aksay, "Functionalized single graphene sheets derived from splitting graphite oxide.," *The journal of physical chemistry. B*, vol. 110, May. 2006, pp. 8535-9.

[107] A. Davies and A. Yu, "Material advancements in supercapacitors: From activated carbon to carbon nanotube and graphene," *The Canadian Journal of Chemical Engineering*, vol. 89, Jun. 2011, p. n/a-n/a.

[108] C.M. Aguirre, S. Auvray, S. Pigeon, R. Izquierdo, P. Desjardins, and R. Martel, "Carbon nanotube sheets as electrodes in organic light-emitting diodes," *Appl. Phys. Lett.*, vol. 88, 2006, p. -.

[109] M.E. Itkis, F. Borondics, A. Yu, and R.C. Haddon, "Bolometric infrared photoresponse of suspended single-walled carbon nanotube films.," *Science (New York, N.Y.)*, vol. 312, Apr. 2006, pp. 413-6.

[110] E. Bekyarova, M.E. Itkis, N. Cabrera, B. Zhao, A. Yu, J. Gao, and R.C. Haddon, "Electronic properties of single-walled carbon nanotube networks.," *Journal of the American Chemical Society*, vol. 127, Apr. 2005, pp. 5990-5.

[111] Z. Gu, L. Zhang, and C. Li, "Preparation of highly conductive polypyrrole/graphite oxide composites via in situ polymerization," *J. Macromol. Sci., Part B: Phys.*, vol. 48, 2009, pp. 1093-1102.

[112] H. Hu, A. Yu, E. Kim, B. Zhao, M.E. Itkis, E. Bekyarova, and R.C. Haddon, "Influence of the zeta potential on the dispersability and purification of single-walled carbon nanotubes.," *The journal of physical chemistry. B*, vol. 109, Jun. 2005, pp. 11520-4.

[113] A. Yu, E. Bekyarova, M.E. Itkis, D. Fakhrutdinov, R. Webster, and R.C. Haddon, "Application of centrifugation to the large-scale purification of electric arc-produced single-walled carbon nanotubes.," *Journal of the American Chemical Society*, vol. 128, Aug. 2006, pp. 9902-8.

[114] Y.T. Park, A.Y. Ham, and J.C. Grunlan, "High Electrical Conductivity and Transparency in Deoxycholate-Stabilized Carbon Nanotube Thin Films," *Journal of Physical Chemistry C*, vol. 114, 2010, pp. 6325-6333.

[115] M.E. Itkis, D.E. Perea, R. Jung, S. Niyogi, and R.C. Haddon, "Comparison of Analytical Techniques for Purity Evaluation of Single-Walled Carbon Nanotubes," *J. Am. Chem. Soc.*, vol. 127, 2005, pp. 3439-3448.

[116] E. Raymundo-Pinero, K. Kierzek, J. Machnikowski, and F. Beguin, "Relationship between the nanoporous texture of activated carbons and their capacitance properties in different electrolytes," *Carbon*, vol. 44, 2006, pp. 2498-2507.

[117] J.N. Barisci, G.G. Wallace, and R.H. Baughman, "Electrochemical Characterization of Single-Walled Carbon Nanotube Electrodes," *Journal of The Electrochemical Society*, vol. 147, 2000, p. 4580.

[118] E. Frackowiak and F. Beguin, "Carbon materials for the electrochemical storage of energy in capacitors," *Carbon*, vol. 39, 2001, pp. 937-950.

[119] T. Wang, A. Kiebele, J. Ma, S. Mhaisalkar, and G. Gruner, "Charge Transfer Between Polyaniline and Carbon Nanotubes Supercapacitors: Improving Both Energy and Power Densities," *Journal of The Electrochemical Society*, vol. 158, 2011, p. A1.

[120] H. Konno, T. Ito, M. Ushiro, K. Fushimi, and K. Azumi, "High capacitance B/C/N composites for capacitor electrodes synthesized by a simple method," *Journal of Power Sources*, vol. 195, Mar. 2010, pp. 1739-1746.

[121] K.-W. Nam, C.-W. Lee, X.-Q. Yang, B.W. Cho, W.-S. Yoon, and K.-B. Kim, "Electrodeposited manganese oxides on three-dimensional carbon nanotube substrate: Supercapacitive behaviour in aqueous and organic electrolytes," *Journal of Power Sources*, vol. 188, Mar. 2009, pp. 323-331.

[122] Y.Q. Han, X.T. Qing, S.J. Ye, and Y. Lu, "Conducting polypyrrole with nanoscale hierarchical structure," *Synth. Met.*, vol. 160, 2010, pp. 1159-1166.

[123] Y. Fang, J. Liu, D.J. Yu, J.P. Wicksted, K. Kalkan, C.O. Topal, B.N. Flanders, J. Wu, and J. Li, "Self-supported supercapacitor membranes: Polypyrrole-coated carbon nanotube networks enabled by pulsed electrodeposition," *J. Power Sources*, vol. 195, 2010, pp. 674-679.

[124] R.K. Sharma, a C. Rastogi, and S.B. Desu, "Pulse polymerized polypyrrole electrodes for high energy density electrochemical supercapacitor," *Electrochemistry Communications*, vol. 10, Feb. 2008, pp. 268-272.

[125] M. Kaempgen, C.K. Chan, J. Ma, Y. Cui, and G. Gruner, "Printable Thin Film Supercapacitors Using Single-Walled Carbon Nanotubes," *Nano Lett.*, vol. 9, 2009, pp. 1872-1876.

[126] D. Wang, F. Li, M. Liu, and H. Cheng, "Improved capacitance of SBA-15 templated mesoporous carbons after modification with nitric acid oxidation," *New Carbon Materials*, vol. 22, Dec. 2007, pp. 307-314.

[127] M. Massa, J. Carvalho, and K. Dalnoki-Veress, "Confinement Effects in Polymer Crystal Nucleation from the Bulk to Few-Chain Systems," *Physical Review Letters*, vol. 97, Dec. 2006, pp. 1-4.

[128] A. Gouldstone, K.J.V. Vliet, and S. Suresh, "Simulation of defect nucleation in a crystal," *Nature*, vol. 411, 2001, pp. 44106-44106.

[129] P. Mavinakuli, S. Wei, Q. Wang, A.B. Karki, S. Dhage, Z. Wang, D.P. Young, and Z. Guo, "Polypyrrole / Silicon Carbide Nanocomposites with Tunable Electrical Conductivity," *J. Phys. Chem. C*, 2010, pp. 3874-3882.

[130] B.N. Jang and C. a Wilkie, "A TGA/FTIR and mass spectral study on the thermal degradation of bisphenol A polycarbonate," *Polymer Degradation and Stability*, vol. 86, Dec. 2004, pp. 419-430.

[131] J. Kim, K. Nam, S. Ma, and K. Kim, "Fabrication and electrochemical properties of carbon nanotube film electrodes," *Carbon*, vol. 44, Aug. 2006, pp. 1963-1968.

[132] Q. Wu, Y. Xu, Z. Yao, A. Liu, and G. Shi, "Supercapacitors based on flexible graphene/polyaniline nanofiber composite films.," *ACS nano*, vol. 4, Apr. 2010, pp. 1963-70.